

Analysis of high-pressure safety valves

Citation for published version (APA):

Beune, A. (2009). *Analysis of high-pressure safety valves*. [Phd Thesis 1 (Research TU/e / Graduation TU/e), Mechanical Engineering]. Technische Universiteit Eindhoven. <https://doi.org/10.6100/IR652510>

DOI:

[10.6100/IR652510](https://doi.org/10.6100/IR652510)

Document status and date:

Published: 01/01/2009

Document Version:

Publisher's PDF, also known as Version of Record (includes final page, issue and volume numbers)

Please check the document version of this publication:

- A submitted manuscript is the version of the article upon submission and before peer-review. There can be important differences between the submitted version and the official published version of record. People interested in the research are advised to contact the author for the final version of the publication, or visit the DOI to the publisher's website.
- The final author version and the galley proof are versions of the publication after peer review.
- The final published version features the final layout of the paper including the volume, issue and page numbers.

[Link to publication](#)

General rights

Copyright and moral rights for the publications made accessible in the public portal are retained by the authors and/or other copyright owners and it is a condition of accessing publications that users recognise and abide by the legal requirements associated with these rights.

- Users may download and print one copy of any publication from the public portal for the purpose of private study or research.
- You may not further distribute the material or use it for any profit-making activity or commercial gain
- You may freely distribute the URL identifying the publication in the public portal.

If the publication is distributed under the terms of Article 25fa of the Dutch Copyright Act, indicated by the "Taverne" license above, please follow below link for the End User Agreement:

www.tue.nl/taverne

Take down policy

If you believe that this document breaches copyright please contact us at:

openaccess@tue.nl

providing details and we will investigate your claim.

Analysis of high-pressure safety valves

PROEFSCHRIFT

ter verkrijging van de graad van doctor aan de
Technische Universiteit Eindhoven, op gezag van de
rector magnificus, prof.dr.ir. C.J. van Duijn, voor een
commissie aangewezen door het College voor
Promoties in het openbaar te verdedigen
op donderdag 22 oktober 2009 om 16.00 uur

door

Arend Beune

geboren te Helmond

Dit proefschrift is goedgekeurd door de promotoren:

prof.dr.ir. J.J.H. Brouwers
en
Prof.Dipl.-Ing. J. Schmidt

Copromotor:
dr. J.G.M. Kuerten

Copyright © 2009 by A. Beune

All rights reserved. No part of this publication may be reproduced, stored in a retrieval system, or transmitted, in any form, or by any means, electronic, mechanical, photocopying, recording, or otherwise, without the prior permission of the author.

Cover design: Oranje Vormgevers Eindhoven (www.oranjevormgevers.nl).

Printed by the Eindhoven University Press.

A catalogue record is available from the Eindhoven University of Technology Library

ISBN: 978-90-386-2006-0

ACKNOWLEDGEMENTS

The following organizations are acknowledged for their contribution:

BASF SE Ludwigshafen am Rhein in Germany for funding this research.

The department Safety Engineering & Fluid Dynamics for providing know-how and the department High-pressure Technology for providing the test facility at the high-pressure laboratory in Ludwigshafen.

Contents

Summary	7
1 Introduction	9
1.1 Background	9
1.2 Literature overview	13
1.3 Research objectives and outline	18
2 Valve sizing methods	21
2.1 Standardized valve sizing method	22
2.2 Real-gas material definition	24
2.3 Real-gas property table generation	26
2.4 Applicability to other gases	31
2.5 Literature review of valve sizing at high pressures	31
2.6 Alternative valve sizing methods	34
2.7 Comparison of valve sizing methods	37
3 Development of numerical tool	39
3.1 Numerical valve model parameters	39
3.1.1 Mathematical models	40
3.1.2 Discretization and solution method	43
3.2 Validation test cases at low pressure	45
3.2.1 1D shock tube	46
3.2.2 Axisymmetric nozzle	49
3.2.3 2D supersonic ramp	51
3.2.4 2D simplified valve model	55
3.2.5 3D pneumatic valve model	57
3.2.6 3D safety valve	59
3.3 Validation test case of a high-pressure nozzle	62
4 Facility for safety valve tests	65
4.1 Design considerations and construction	65
4.2 Measurement variables	67
4.2.1 Valve disk lift	68
4.2.2 Valve disk force	70

4.2.3	Temperature	73
4.2.4	Pressure	74
4.2.5	Liquid mass flow rate	75
4.2.6	Gas mass flow rate	78
4.2.7	Discharge coefficient	80
4.2.8	Data acquisition	80
4.3	Examples of valve tests	81
4.3.1	Valve test with water	81
4.3.2	Valve test with nitrogen	82
5	Comparison of numerical and experimental results	85
5.1	Liquid valve flow	85
5.1.1	Experimental results	85
5.1.2	Numerical simulations	87
5.1.3	Comparison and analysis	89
5.2	Gas valve flow	93
5.2.1	Re-evaluation of low-pressure safety valve measurement data	93
5.2.2	Numerical simulation of high-pressure valve tests	95
5.2.3	Comparison and analysis of high-pressure valve tests	98
5.3	Safety valve flow with real-gas effects	108
6	Dynamic flow simulations	111
6.1	Numerical approach	113
6.2	Results	116
7	Discussion	121
	Bibliography	127
	Dankwoord	133
	Curriculum vitae	135

Summary

Analysis of high-pressure safety valves

In presently used safety valve sizing standards the gas discharge capacity is based on a nozzle flow derived from ideal gas theory. At high pressures or low temperatures real-gas effects can no longer be neglected, so the discharge coefficient corrected for flow losses cannot be assumed constant anymore. Also the force balance and as a consequence the opening characteristics will be affected.

In former Computational Fluid Dynamics (CFD) studies valve capacities have been validated at pressures up to 35 bar without focusing on the opening characteristic. In this thesis alternative valve sizing models and a numerical CFD tool are developed to predict the opening characteristics of a safety valve at higher pressures.

To describe gas flows at pressures up to 3600 bar and for practical applicability to other gases the Soave Redlich-Kwong real-gas equation of state is used. For nitrogen consistent tables of the thermodynamic quantities are generated. Comparison with experiment yielded inaccuracies below 5% for reduced temperatures larger than 1.5.

The first alternative valve sizing method is the *real-average* method that averages between the valve inlet and the nozzle throat at the critical pressure ratio. The second *real-integral* method calculates small isentropic state changes from the inlet to the final critical state. In a comparison the most simple *ideal* method performs slightly better than the *real-average* method and the dimensionless flow coefficient differs less than 3% from the most accurate *real-integral* valve sizing method.

Benchmark validation test cases from which field data is available are used to investigate the relevance of the physical effects present in a safety valve and to determine the optimal settings of the CFD code ANSYS CFX. First, 1D Shock tube calculations show that strong shocks cannot be captured without oscillations, but the shock strength in a safety valve flow is small enough to be accurately computed. Second, an axisymmetric nozzle (ISO 9300) model is simulated at inlet pressures up to 200 bar with computed mass flow rate deviations less than 0.46%. Third, a supersonic ramp flow shows a dependency of the location of the separation and reattachment points on the turbulence model, where the first-order accurate SST model gives the best agreement with experiment. Fourth, computations of a simplified 2D valve model by Föllmer show that reflecting shocks can be accurately resolved. Fifth, a comparison of mass flow rates of a pneumatic valve model results in deviations up to 5% which seems due to a 5% too high stagnation pressure at the disk front. Sixth, the computed safety valve capacities of TÜV Rheinland Aachen overpredict the measured discharge coefficient by 18%. However, a replication of this experiment at the test facility re-

duces the error to 3%. A clear reason for the large deviation with the reference data cannot be given. Lastly, the computed mass flow rates of a nozzle flow with nitrogen at pressures up to 3500 bar agrees within 5% with experiment.

A high-pressure test facility has been constructed to perform tests of safety valves with water and nitrogen at operating pressures up to 600 bar at ambient temperature. The valve disk lift and flow force measurement systems are integrated in a modified pressurized protection cap so that the opening characteristics are minimally affected. The mass flow rates of both fluids are measured at ambient conditions by means of a collecting tank with a mass balance for fluids and through subcritical orifices for gases with inaccuracies of the discharge coefficient of 3 and 2.5%.

Reproducible valve tests with water have been carried out at operating pressures from 64 to 450 bar. The discharge coefficient does not depend on the set pressure of the safety valve. The dimensionless flow force slightly increases with disk lift. CFD computations of selected averaged measurement points with constant disk lift show that for smaller disk lifts the mass flow rate is overpredicted up to 41%. Extending the numerical model with the Rayleigh-Plesset cavitation model reduces the errors of the mass flow rates by a factor of two. The reductions in the flow forces range from 35 to 7% at lower disk lifts.

Also reproducible valve tests with nitrogen gas at operating pressures from 73 to 453 bar have been conducted. The discharge coefficient is also independent of set pressure. In contrast to the water tests, the dimensionless flow force continually decreases with disk lift. All computed mass flow rates agree within 3.6%. The computed flow forces deviate between 7.8 and 14.7%.

An analysis shows that the effects of condensation, transient effects, variation of the computational domain or mechanical wear cannot explain the flow force deviation. The reason partially lies in a larger difference between the set pressure and the opening pressure of the test valve. The flow distribution around the valve spindle is sensitive to the inlet pressure and rounding of sharp edges due to mechanical wear. The cavity of the valve spindle probably causes valve chatter partially observed in the experiments and simulations.

In safety valve computations with nitrogen at higher pressures up to 2000 bar and temperatures down to 175 K outside the experimentally validated region the discharge coefficient of all three valve sizing methods varies less than 6% compared to the 7 bar reference value at ambient temperature. So the standardized *ideal* valve sizing method is sufficient for safety valve sizing. The dimensionless force, however, increases with pressure up to 34% so that the valve characteristic is affected.

The influence of valve dynamics on steady-state performance of a safety valve is studied by extending the CFD tool with deformable numerical grids and the inclusion of Newton's law applied to the valve disk. The mass flow rate and disk lift are less affected, but a fast rise and collapse of the flow force due to redirection of the bulk flow has been observed during opening. Only dynamic simulations can realistically model the opening characteristic, because these force peaks have not been observed in the static approach. Furthermore, the valve geometry can be optimized without sharp edges or cavities so that redirection of the flow will result in gradual flow force changes. Then, traveling pressure waves will lead to less unstable valve operation.

Chapter 1

Introduction

1.1 Background

In process industry, a process is continuously further optimized to operate more efficiently closer to its mechanical limits such as its maximum allowable operating pressure. To ensure safe plant operation, the performance of all levels of safety systems needs to be reconsidered. Besides the organizational and process control measures to maintain safe plant operation, the last stage of protection of a process apparatus against excess pressure is often through the use of a mechanical self-actuated device. These devices, a safety relief valve or bursting disc, are mostly installed on top of the pressurized system, like a vessel, to be protected and directly connected to the system through a short pipe (figure 1.1 left).

Excess pressures can result from a failure in the heating system supplying extrinsic heat to the contents of a vessel. Further possible causes are a breakdown of the cooling system or the presence of a catalyst overdosing in a reactor vessel, which may initiate an exothermic chemical reaction. Furthermore, leakages or overpressures in an apparatus connected to the pressurized system considered can result in excess pressure of the system. If in case of an emergency relief the temperature rise and so the pressure rise of the system is estimated, the most suitable safety relief device can be chosen.

When the pressure in the apparatus reaches the set pressure of the safety device, the pressure forces the disk to open and the fluid is discharged into a disposal system, a containment vessel or directly into the atmosphere. In the case of a spring-loaded safety relief valve a spring forces the disk to close when the pressure decreases below the closing pressure of the valve. Then, the plant can be shut down in a controlled way with a minimum loss of product to the environment.

A spring-loaded safety relief valve consists of a compression spring, which presses the valve spindle with disk on the valve seat in order to seal the pressurized system in case of operating conditions below the valve set pressure (figure 1.1 right). Prior to the valve installation the spring is pre-stressed so that the spring force equals the desired pressure multiplied with the sealing area of the valve seat. At this pressure the safety

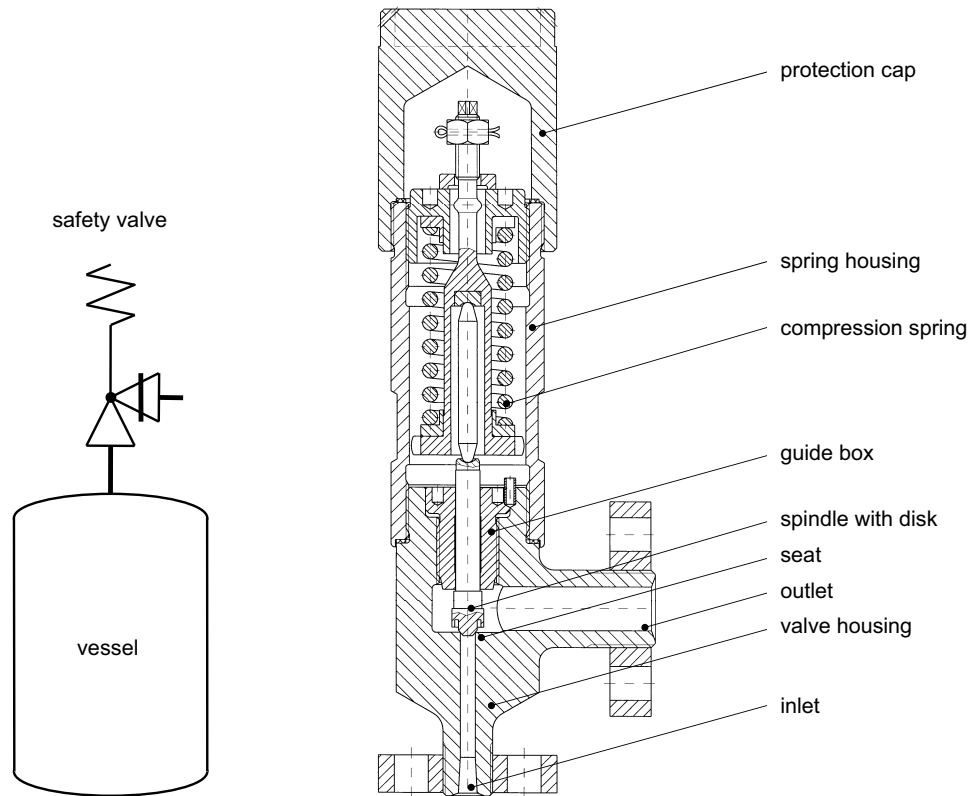


Figure 1.1. Schematic setup and construction drawing of a safety valve.

valve should open, which is defined as the set pressure. Depending on the geometry of the valve seat and spindle with disk as well as spring stiffness, *proportional safety valves* open proportionally when the momentum transfer of the stagnating flow to the spindle, and thus the force on the spindle, gradually increases with valve opening and stagnation pressure at the valve inlet. These valves are used in relative slow pressure exceeding processes such as a thermal expansion.

For *pop-up safety valves* the outer part of the disk at the top of the spindle has a larger lifting-aid resulting in a larger area with enhanced pressures and deflects flow at a larger angle. Then, the momentum transfer and flow area at higher pressures is already large at small opening resulting in a larger force increase than the linear force increase of the compression spring. At a certain valve disk lift the flow force equalizes the remaining forces acting on the valve disk. Pop-up valves open with a pop-action and are used when the response should be accurate on the occurrence of high pressure increase rates.

Besides the flow and spring force, three remaining forces interact with the valve disk as well (figure 1.2 left). First, the acceleration force is present when the valve

starts to open, with the mass of the moving components of the valve slowing down rapid opening of the valve. Second, due to pressure losses in the housing and outlet of the valve a back flow force reduces the net flow force when the valve is open. Then the pressure rises in the valve housing as well as in the spring housing. Third, the gravity force constantly pulls the vertically oriented valve disk down as well depending on its orientation. Fourth, the gap between the spindle and guide box is sufficiently large so that mechanical friction forces are minimal and can be neglected especially for high-pressure valves.

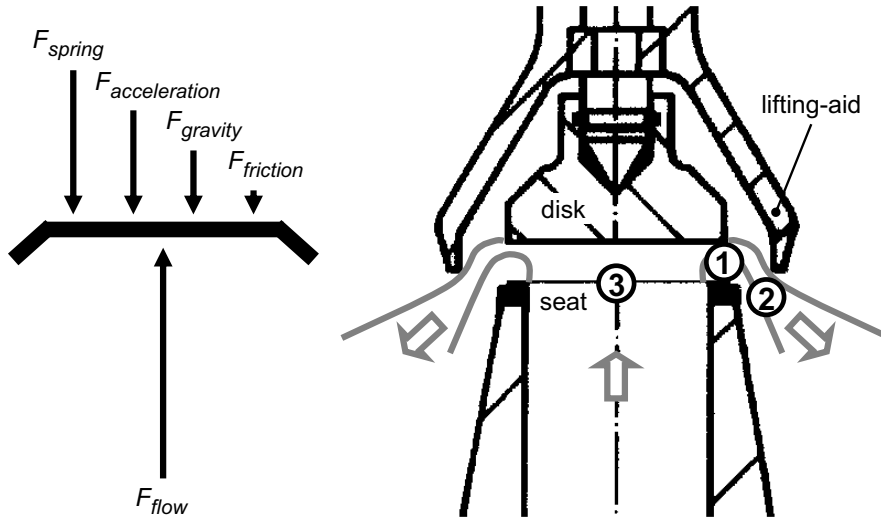


Figure 1.2. Force balance of and possible choking areas in a safety valve indicated by the numbers.

During valve opening a complex flow pattern is formed between the valve seat and spindle or disk (figure 1.2 right). In this region with the smallest flow cross-sectional area the geometry forces the flow to be accelerated up to the smallest cross-sectional area and to be deflected. Depending on the thermodynamic state of the fluid the contour of the flow varies. In case of compressible flow, when the pressure ratio between the inlet and outlet exceeds the critical pressure ratio the flow chokes. Then, at small valve disk lifts a contour surface with Mach number unity is reached between the valve seat and the disk (point 1 of figure 1.2 right) that limits the total mass flow rate through the valve. At larger openings of the valve, the narrowest through-flow cross-sectional area moves to the lifting-aid at the outer side of the valve disk i.e. to point 2. For still larger opening the smallest cross-sectional area is at the valve seat itself, so that the sonic flow plane is located at 3. For further valve opening the mass flow rate does not increase anymore for the same thermodynamic state at the inlet.

After passing the Mach number unity plane the flow expands and accelerates further to supersonic with low pressures and temperatures, conditions for which con-

densation could occur. Also the local pressure at the disk wall is reduced, thus the flow force acting on the disk varies with the position of the effective throat as well. Further downstream a compression shock wave brings the flow to the thermodynamic state at the valve outlet. The strength of the compression wave depends on the pressure ratio. Because of the strong deflection of the internal forced flow underneath the valve disk, at the edges of the disk and seat, large adverse pressure gradients result in flow separation areas and areas with recirculating flow. In addition, due to high operating pressures of safety valves the fluid has to be considered as a real gas.

If the flow Mach number remains much smaller than unity throughout the valve, the flow can be considered incompressible. Then, compressibility effects such as shocks and sonic flow do not occur, but in the same area after the smallest cross-sectional area with the largest velocities (equal to the supersonic area for compressible flow) the flow still strongly accelerates with low local pressures as well so that for liquid flows phase transition by means of cavitation can occur. The mass flow rate is limited by pressure losses occurring in the whole valve housing.

The European standard EN ISO 4126-1 [30] and the derived German regulation AD 2000 [1] describe the sizing procedure of safety devices for protection against excess pressure. These standards are valid for safety valve sizing with operating pressures up to 200 bar. However, many plants throughout the world are operated at pressures up to 3000 bar for the production of synthesis gas or low-density polyethylene. In this pressure range the discharge capacity is not prescribed and currently the valve sizing procedures have to be extrapolated.

The flow capacity calculation of a safety valve is based on isentropic flow through a nozzle with a correction factor for flow losses and redirection of the flow, the so-called discharge coefficient K_d . For incompressible nozzle flow the mass flow rate calculation is based on the Bernoulli equation with a correction for viscous flow effects and for compressible flow the equation of state (EoS) for a perfect gas is used. The discharge coefficient is experimentally determined in valve tests mostly at low pressures with removed compression spring so that the valve spindle can be fixed at a specified position. There are test rigs available with operating pressures up to 250 bar to test the function and release capacity of spring-loaded safety relief valves. The test fluids are sub-cooled water and gaseous air or nitrogen. Discharge coefficients derived from these tests are directly used for other liquids and gases as well. As a consequence, in the standard it is assumed that the experimentally obtained discharge coefficient is constant for a certain valve type, independent of the set pressure and compressibility of the fluid. From a physical point of view, at higher pressures the intermolecular interaction of a gas denoted as real-gas effects cannot be neglected. Therefore, it is expected that the discharge coefficient will vary with pressure while it will also depend on the gas considered.

Alternative analytical calculation tools are available to calculate the flow conditions around the safety valve as part of the piping system (Cremers, 2000 [15]). Especially for piping systems with long entrance and relief lines enhanced pressure losses occur that affect the proper functioning of the safety valve. In the worst case the valve starts to vibrate due to oscillating flow so that the maximum disk lift is not

reached at all and the effective discharge capacity is reduced substantially. On the whole, these methods do not consider the complex flow dynamics in a safety valve and assume that the safety valve will open and relieve as expected with a constant assumed discharge coefficient at 10% above the maximum allowable operating pressure of the pressurized system as defined in the valve sizing standards.

1.2 Literature overview

In order to identify safety valve functioning the literature overview starts with safety valve flow considerations and the dynamics of safety valves. Then, studies of safety valve flows carried out employing Computational Fluid Dynamics (CFD) are given. Next, the focus is on CFD studies of flow phenomena that are related to safety valve flows. Finally, recent references are discussed that consider flow dynamics of valves using with CFD.

Dynamics in safety valves

In many literature sources the dynamic response of safety valves is discussed. To start with the experimental work of Sallet (1981) [57], the flow inside a typical safety valve was studied by visualization of the flow in a 2D valve model. Pressure distributions and discharge capacities were investigated in tests with choked air flow, water and choked two-phase flow. It can be recognized that the physical effects of flow separation, cavitation, choking and valve disk vibrations are significant flow phenomena that complicate the prediction of the characteristic valve coefficients. Sallet also observed that vortical flows near the valve disk (periodic flow oscillations due to flow past a cavity) cause valve disk vibrations. This effect is larger for incompressible flows. Also in a safety valve the interaction between shock waves and flow separation can cause self-sustaining oscillating flow fields.

Föllmer (1981) [22] performed experimental research on air flow through a flat valve choked in the annular gap. By means of a Mach-Zender-Interferometer isodensity fringes of the flow were accurately determined. Assuming isenthalpic flow, the density distribution was converted into a Mach number distribution to obtain insight into the gas dynamics of choked gas flow. The pressure ratio and the geometry of the valve inlet were varied to study the effects of flow separation and shocks resulting in additional pressure losses and periodic oscillations of the supersonic part of the flow. This research forms the basis for a quantitative comparison with resulting computational methods.

Singh (1982) [62] studied the dynamics and stability of spring-loaded safety relief valves. He developed an analytical coupled thermal-hydraulic and spring-mass systems model. He concluded that the operating stability of a safety valve can be increased by either lowering an adjustment ring mounted at the valve seat so that the discharge angle becomes smaller, or by a softer spring, smaller backpressures, or adding a damping device as well. Also MacLeod (1985) [40] used analytical models to analyze the dynamic stability of safety valves. The addition of a dampening system balances between fast valve opening and the avoidance of rapid and extreme alternating opening and closing of the safety valve, the so-called valve chatter or flutter.

Baldwin (1986) [8] introduced design guidelines to avoid flow-induced vibration in safety valves, which is the main cause of relief failure in power plant industry. This vibration comprises unstable coupling of vortex shedding at the valve inlet with the side branch acoustic resonance. The design procedure uses a relationship involving Strouhal number, Mach number and pipe stub dimensions based on dynamic response data from safety valves in power plant steam service. It was observed, that the shape of the trailing edge of a cavity can stabilize the flow in such a way that alternating flow impingement is avoided. Moisidis (1995) [44] reduced the risk of relief valve failure by improving the design of a Crosby safety valve. By reducing the misalignment between moving parts and eccentric loading, the risk of valve operating failures, such as popping pressure drift, spurious valve actuations, or leakage is minimized.

In choking flow experiments by Betts (1997) [10] 3D effects on the local pressure ratio upstream of the safety valve disk were studied. These effects were more apparent at the outer part of the disk due to circulating flow patterns. This asymmetry of the flow field around the disk is confirmed by the experiments of pilot-operated relief valves of Botros (1998) [12]. He found that the safety valve is subjected to lateral forces, which can lead to rubbing, sticking or in extreme cases adhesive wear, i.e. galling.

Safety valve tests with enhanced backpressures of Francis (1998) [24] showed that the movement of the shock wave due to changes in reservoir pressure and backpressure clearly affects the lifting force on the disk and hence its position, especially at low lifts for which the shock wave can be expected to be relatively close to the seal. This indicates again that backpressure effects are important for the 3D flow field in the narrowest flow cross-section of the safety valve. In addition to the operating stability mechanisms of a safety valve configuration, Frommann (2000) [25] investigated the effect of bends in the inlet line on the reflection of the pressure wave in experiments with straight vertical inlet lines. There were no significant differences observed and the mechanism remains the same.

Cremers (2003) [16] experimentally investigated the effect of the inlet and discharge pipe dimensions on the dynamical performance of a safety relief valve. For a certain configuration the valve can chatter. Practical technical guidelines and design rules have been created to permit a certain maximum length of the inlet and discharge pipes. Also a maximum allowable pressure loss in the pipes during discharge due to friction in the inlet pipe has been defined. Muschelknautz (2003) [47] evaluated the effect of flow reaction forces during discharge of a safety relief valve on a larger scale, which is the foundation of a plant. From numerical calculations and blowdown tests he concluded that a T-piece at the outlet compensates stationary flow reaction forces and the instationary flow forces occur at a too high frequency to affect the plant.

Safety valve studies with CFD

In the above described literature sources the effects of valve flow on the dynamical performance of safety valves are generally discussed. The present project, however, does not focus on the chatter phenomenon itself, but on the design of a numerical tool to describe the complex 3D flow in safety valves necessary for proper valve sizing and design. It has been chosen to use advanced numerical methods to model these 3D flow

fields. Computational fluid dynamics (CFD) is a numerical approach that provides a qualitative and with extra effort sometimes even a quantitative prediction of 3D fluid flows by means of solving partial differential equations with the help of numerical methods. It gives also insight into flow patterns that are difficult, expensive or impossible to study with traditional experimental techniques. As in experiments only a few local or integrated quantities can be measured for a limited range of problems and operating conditions, CFD predicts all modeled quantities with high resolution in space and time in the whole actual flow domain for any operating condition whether safe or unsafe. It is noted that CFD results can never be 100% reliable, because the input data may involve inaccuracy, the mathematical model of e.g. turbulence may be inadequate and the computational recourses may limit the computational grid resolution and therewith the accuracy of the flow problem too much.

In the following academic studies the 3D flow physics in a safety valve is calculated with the help of CFD software. In the thesis of Zahariev (2001) [71] the flow behavior in safety valves was studied with the commercial CFD software package CFX TASCflow. The study mainly focused on optimization of the valve disk. The validation of the numerical model was limited to force experiments of a single valve experiment series of air with fixed disk lifts at an inlet pressure of 20 bar blowing off at atmospheric conditions. Although the differences between the predicted and measured quantities is within 5%, from a single validation it is not possible to evaluate the performance of the numerical tool. As a result, more validation needs to be done with the focus on the physical phenomena occurring in high-pressure safety valve flows.

In the work of Bredau (2000) [13] air flows in simplified pneumatic valve models up to 7 bar have been visualized in experiments and calculated with the CFD program TASCflow. The calculated flow field showed good agreement with the experimental data. The flow could be considered in the smallest flow cross-section as quasi-steady, but at the outlet the fluctuations were larger, so that a steady approximation was no longer valid. This work shows the ability of CFD modelling to accurately describe safety valve flows, but this applies only to flows at low pressures. Within the same research project in the work of Bürk (2006) [14], numerical calculations with CFX based on additional experimental data of pneumatic valve models showed that for the practical relevant disk lift range with the smallest flow cross-sectional area smaller than the seat area, the calculated mass flow rates and the pressure distribution on the valve disk are in good agreement with experiments. For higher disk lifts the pressure loss in the stagnation area is calculated too small but it still resulted in a smaller difference of the measured and predicted forces.

In industry, the role of CFD for safety valve design gradually becomes more important. Darby and Molavi (1997) [18] calculated viscous correction factors for high-viscous fluids through safety valves with the help of CFD. In the work of Föllmer and Schnettler (2003) [23] it is stated that the flow fields agree with expectations, but quantitative comparisons with experimental data is not given. Furthermore, in recent work of Moncalvo and Höhne (2008) [45] four mass flow rates of fixed lift safety valve experiments up to 35 bar have been calculated with ANSYS Flo with deviations up to 11%.

According to the academic studies modeling safety valve flow should be possible with sufficient accuracy, but validation has been considered for low pressures only. The industry, however, has not published accurate validation data yet. The capability of a numerical tool for the highly complex safety valve flow can be judged only when it is also focused on the individual flow phenomena that occur in safety valve flows.

CFD studies of flow phenomena in high-pressure safety valves

The flow in a safety valve is basically a nozzle flow that impinges on a plate and is deflected to a side outlet. Nozzle flows are extensively studied with analytical models also with the inclusion of real-gas effects, see section 2.5. Besides these models, nozzles are also studied with numerical methods. Kim (2008) [33] investigated flow features of high-pressure hydrogen through a choked nozzle using a fully implicit finite volume method. Several kinds of EoS were used in order to study the influence of real-gas effects, with the real-gas EoS Redlich-Kwong (RK) predicting comparatively well.

Johnson (1998) [32] investigated the effectiveness of using CFD for a critical standard ISO 9300 nozzle assuming a perfect gas, assessing the level of agreement between experiments and numerical solutions for four different gas species (Ar, N₂, CO₂, and H₂). The results matched within 0.5% except for CO₂ that is 2%. The inclusion of real-gas effects would probably improve the results. These previous studies show that modeling nozzle flows is possible with CFD with high accuracy, but validation at high pressures cannot be carried out because of lack of experimental data.

Supersonic impinging jets were experimentally and numerically investigated by Alvi (2002) [2]. A stagnation bubble with low-velocity recirculating flow and high-speed radial wall jet were found to be similar in the computations with the Shear Stress Transport (SST) turbulence model and the experimental data. It was stated that the Boussinesq hypothesis is not valid in the impingement area and Reynolds-stress models should improve the results. According to this work the usage of the SST model is promising, but the influence of the turbulence model used for safety valve flows should be investigated.

The stagnating flow on the disk forms a boundary layer and becomes supersonic again followed by a shock inducing flow separation. This interaction in the form of shock-induced boundary layer separation occurs in supersonic intakes of an aircraft and is extensively experimentally investigated and studied with CFD. In the experimental work of Müller (2001) [43] the position and reattachment of a supersonic flow past a 24° ramp was investigated. Also NASA has experimental data available from a supersonic shock/boundary-layer interaction database from Settles (1991) [60] for the same geometry.

In the studies with CFD, Druguet (2003) [21] investigated the influence of viscous dissipation in shock wave reflections in supersonic steady flows. She found that the choice of the numerical method has a significant impact on the quality of the predicted shock reflections and the height of the so-called Mach stem.

Knight et al. (2003) [34] compared results of numerical simulations with different turbulence models and five different configurations with experiment. For the supersonic flow passing a 3D double fin, two-equation turbulence Reynolds-Averaged

Navier-Stokes (RANS) models sufficiently predict the surface streamline pattern, but accurately predict the surface pressure only in the initial region of the interaction.

Kral (1998) [36] applied different RANS models to the calculation of complex flow fields over aircraft components. The SST turbulence models performed best for the lift and drag of an airfoil with separation and shock. This model is also capable to predict the flow separation in shock/boundary layer interaction calculations. For non-equilibrium external flows the SST turbulence model is recommended. For internal flows the $k - \epsilon$ models may provide better predictions than the SST model.

Rigas (2005) [54] validated the propagation of shock waves produced by a dense explosive detonation in a small-scale complex tunnel configuration. The arrival time and pressure of the explosion front were reasonably predicted and it was concluded that CFD can be effectively used for problems with sudden and complex flow phenomena.

CFD studies of safety valve dynamics

In recent studies the valve opening characteristics are investigated with CFD. A first preliminary study without any verification data is from Domagala (2008) [20], in which the CFD program ANSYS CFX was used to prove the principle of fluid-structure interaction (FSI) for a pilot-operated relief valve. It was experienced problematic to define a single deformable grid that can cover the whole operating range. Srikanth (2009) [66] studied subsonic compressible air flow in an electric circuit breaker with ANSYS CFX with valve element mesh motion. From the axisymmetrical simulations the pressure history was found to be significantly affected by the velocity of the moving contact in the chamber, which can be used for future design studies.

Dynamic simulations with FSI is also applied in practical engineering problems. In coupled FSI simulations of a vacuum relief valve of Reich (2001) [51] a moving body simulation was set up to mimic field conditions during opening of the valve. With this set up the design was improved to avoid the tendency of the valve to flutter under expected subcritical gas flow conditions. The problem was solved with two grids that interact with each other by a overset mesh module. The computed mass flow rate at full opening deviated 3% from that found in experiment.

Li et al. (2005) [38] used non-linear finite element analysis in combination with CFD to dynamically model the closing characteristics of a subsurface safety valve operating in productive gas wells. A combination of valve testing and finding the cause for problematic slam-closure loads with the help of FSI has led to a changed valve design that closes throughout the entire range of flow rates. With this engineering approach the strength of FSI is used to qualitatively analyse the valve function without focussing on local physical effects.

Mahkamov (2006) [41] has developed a CFD model for axisymmetric flow to analyse the working process of a Stirling cycle machine. The gas dynamics and heat transfer of the internal gas circuit are calculated on a structured computational grid, where a virtual piston cyclic moves from the smallest volume of the compression space to the one of a connected expansion space. With this model the performance is more accurately predicted than the traditional approach with analytical models. However, comparison with local measurement data is not pursued.

The only study in which the problem of reduced grid quality is tackled with multiple grids with high-speed flows is the research from Bürk (2006) [14]. He carried out transient CFD simulations with moving grids with a predefined trajectory of a pneumatic valve with critical gas flow with ANSYS CFX. Due to large deformations of the computational domain intermediate meshes are necessary to keep the mesh quality appropriate. With the help of the programming language Perl simulations with multiple meshes are automatically controlled. Validations of the numerical model employing data from experiment with prescribed valve disk velocity showed that a quasi-stationary approach is sufficient for a pressure ratio down to 1/3. For higher pressures and faster disk movements it is expected that the already observed dynamic effects become significant.

1.3 Research objectives and outline

From the literature overview it is clear that the physical effects of choking, shocks and flow separation basically occur in safety valves. Preliminary CFD studies already showed that it is basically possible to predict safety valve capacities. However, the validation only occurred at pressures up to 35 bar only with different levels of agreement. In order to evaluate the performance of the numerical method, it is desired to validate the physical phenomena occurring in safety valves separately, so that the mathematical models of the numerical method can be evaluated. In the present thesis these phenomena are investigated with also the application to high-pressure valve flows. Also the opening characteristics have been explored with CFD, in which most studies lack on sufficient validation.

The objective of this research is to develop a numerical tool of sufficient predictive capability that allows the calculation of mass flow capacities and opening characteristics of spring-loaded safety valves at operating pressures up to 3600 bar. For the mass flow capacity calculation the standardized sizing method based on nozzle flow of a perfect gas needs to be evaluated. Possibly this model has to be extended to account for flows at high pressures with real-gas effects. Besides the mass flow capacity, for predicting the opening characteristics CFD is the only way to obtain the complex flow phenomena. Therefore, a numerical method needs to be developed that covers the physical effects so that the pressure distributions around and flow force on the valve disk can be predicted accurately. This method needs to be extended with moving meshes to study and optimize the valve opening characteristic and operating stability.

As a result, with the use of the numerical tool the number of high-cost valve function tests can be reduced, the reliability of safety valves in existing process systems can be improved and valve design for future applications can be optimized. The research focuses on compressible high-pressure single-phase flow through safety valves discharging into the atmosphere.

In the following chapter descriptions of the approach of this research project is outlined. In chapter 2 the current standardized valve sizing method based on a perfect-gas gas nozzle model will be presented in detail. In order to evaluate this method

for safety valve flows at high pressures a real-gas EoS will be proposed, from which real-gas data will be derived. The same data will also be used for CFD computations later on. Then, two alternative valve sizing methods for real gases will be discussed with different complexity. Lastly, to evaluate the performance of the existing and the two new valve sizing methods with real-gas effects the results of the methods will be compared with each other.

In chapter 3 a numerical method for valve characterization will be developed, that is based on a finite volume method to solve the time dependent Navier Stokes equations. First, the mathematical models, the discretization and the solution method will be given. Then, a suitable CFD software package will be chosen and its model parameters will be determined in a step-by-step development from 1D inviscid to 3D real-gas flows. As part of the development process, validation test cases based on reference data from literature will be defined. The cases are chosen such that these are a combination of the relevant physical phenomena. Finally, the numerical method as well as the valve sizing methods will be validated with experimental data of a high-pressure nozzle with inlet pressures up to 3500 bar.

In order to validate the numerical tool at high-pressures, experimental data of safety valve flows has to be obtained. Chapter 4 will present the high-pressure test facility that will be designed and realized to conduct function tests of high-pressure safety valves with operating pressures up to 600 bar. With this data the valve sizing models and the CFD tool for valve characterization can be validated. First, design considerations for the construction of the test facility will be provided. Then, the apparatus for the quantities to be measured will be given. At the end, two examples of valve tests will be shown for which the valve capacity and opening characteristic of a safety valve operating with sub-cooled water and gaseous nitrogen can be determined.

In chapter 5 the experimental results from the high-pressure valve tests will be compared with both the standardized valve sizing methods and with CFD computations of the developed numerical model. First, steady-flow experimental results of valve tests for sub-cooled water at two different set pressures will be presented. Then, the setup of the numerical simulations will be given and after that both results will be compared with each other. In the analysis deviations between the results will be discussed with the focus on local physical effects. The same comparison and analysis will be presented for gaseous nitrogen valve flows at two different set pressures. This chapter concludes with calculations of valve flows outside the experimental validation region to higher pressures up to 2000 bar to investigate the influence of real-gas effects on the valve characteristic.

In chapter 6 the numerical tool will be extrapolated to transient flow with the inclusion of fluid-structure interaction (FSI). Then the opening characteristics and operating stability of safety valves will be studied for liquid flow.

In chapter 7 the outcome of this research will be discussed and recommendations for application of the valve sizing methods and numerical valve characterization tool will be given.

Chapter 2

Valve sizing methods

This chapter focuses on valve models to determine the discharge capacity of safety valves, which is required for accurate valve sizing. As stated in the introduction the discharge coefficient K_d is the correction factor between the mass flow rate of an isentropic flow in a nozzle \dot{m}_{nozzle} and the actual mass flow rate in a safety valve \dot{m}_{exp}

$$K_d = \dot{m}_{exp} / \dot{m}_{nozzle}. \quad (2.1)$$

Ideally, this discharge coefficient should only account for flow losses and redirection of the flow caused by a non-ideal geometry. In addition, the dimensionless flow coefficient C calculated with the nozzle model should only cover the thermodynamic state changes as much as possible by [59]

$$C = \frac{\dot{m}_{nozzle}}{A_0 \sqrt{2p_0 \rho_0}}, \quad (2.2)$$

with valve seat area A_0 , stagnation pressure p_0 and density ρ_0 or specific volume $v_0 = 1/\rho_0$. Then the nozzle model depends on the thermodynamic fluid properties, such as set pressure and compressibility. It is hypothesized that depending on the extent that the nozzle flow model covers the thermodynamics of the nozzle flow, the discharge coefficient will be less sensitive to set pressure and compressibility. In fact, this chapter will analyse different nozzle flow models that deliver a fluid-dynamic flow coefficient used as a basis for valve sizing methods at high-pressures.

First, in section 2.1, the standardized valve sizing method will be discussed, which does not properly take real-gas effects into account. Then, in sections 2.2 and 2.3 a real-gas EoS will be proposed from which real-gas property data will be derived to accurately compute flows at high pressures with real-gas effects. Also the possibility to use the real-gas definitions for other gases is discussed in section 2.4. Furthermore, in section 2.5, a literature study focuses on existing approaches of nozzle flows with real-gas effects. Hereafter, in section 2.6, two alternative valve sizing methods that account for real-gas effects will be presented. In the last section 2.7, results of the existing and the two new valve sizing methods will be compared with experimental data of a high-pressure nozzle with inlet pressures up to 3500 bar, so that the performance of the models can be assessed.

2.1 Standardized valve sizing method

For sizing of a safety valve, the capacity needs to be known at a certain specified inlet pressure. The prediction of the discharge capacity is based on quasi-one-dimensional reversible and adiabatic, i.e. isentropic, flow through a nozzle with smallest cross-sectional area A_0 and an experimentally determined discharge coefficient K_d . This discharge coefficient corrects for flow losses due to friction, deflection and separation of the flow. For nozzle flows this factor is close to unity but for safety valve flows it mostly varies between 0.5 and 0.9. This dependency stems from the area of the valve seat being taken rather than the actual geometrical smallest cross-sectional flow area. The latter could be smaller at lower disk lifts.

The principle of critical or choked gas flow is explained with a flow in a convergent-divergent duct or stream tube with variable cross-section. First the Mach number Ma is defined, which is the ratio between the flow velocity u and the speed of sound a

$$Ma = u/a. \quad (2.3)$$

The speed of sound is related to the isentropic change of pressure p with respect to density ρ

$$a^2 = \left(\frac{\partial p}{\partial \rho} \right)_s. \quad (2.4)$$

From the conservation equations for quasi-one dimensional isentropic flow and the definition of the speed of sound an area-velocity relation valid for isentropic flow in a variable-area duct is deduced (Anderson, 2003) [3]

$$\frac{1}{A} \frac{dA}{dx} = (Ma^2 - 1) \frac{1}{u} \frac{du}{x}. \quad (2.5)$$

This expression shows that a subsonic flow in a convergent duct will always accelerate, while a supersonic flow in the same duct shows the opposite behavior. The relation also shows that an (isentropic) acceleration from subsonic flow to supersonic flow, passing the sonic condition $Ma = 1$, is only possible at an extremum of the duct cross-sectional area A . Further analysis shows that this always is a minimum, a throat. Apparently, the mass flow density ρu as a function of flow Mach number Ma shows the maximum at $Ma = 1$, corresponding to a minimum A . This phenomenon is called choking. With the calculation of the gaseous mass flow rate \dot{m}_g at the throat of the convergent-divergent duct with density at the throat ρ^* , cross-section area A_0 and sonic velocity $u = a$

$$\dot{m}_g = \rho^* A_0 a, \quad (2.6)$$

equation (2.5) prevents increase of the Mach number beyond unity, so that a further reduction in pressure at the nozzle exit cannot influence the flow properties at the throat so that the mass flow rate only depends on the inlet conditions.

According to the European standard EN ISO 4126 [30], the derived German regulation AD 2000 [1] and the American standard API 520 [5] for non-condensing and non-reacting vapors and gases, the dimensionless flow coefficient $C_{g,id}$ is derived from the

perfect gas EoS at stagnation conditions

$$C_{g,id} = \sqrt{\frac{\kappa_0}{\kappa_0 - 1} \eta^{\frac{2}{\kappa_0}} \left[1 - \eta^{\frac{\kappa_0 - 1}{\kappa_0}} \right]}. \quad (2.7)$$

The variable η is the ratio of the pressure p at the smallest cross-section area and inlet pressure p_0

$$\eta = p/p_0. \quad (2.8)$$

This standardized calorically perfect gas approximation of the flow coefficient will be referred to as *ideal* method in a comparison in section 2.7. For a calorically perfect gas the adiabatic exponent κ_0 is defined as the ratio between the specific heats or given as a function of the specific gas constant $R_s = R/M$ given by the molar gas constant R divided by the molar mass M of the gas

$$\kappa_0 = \frac{c_{p,0}}{c_{p,0} - R_s}. \quad (2.9)$$

When the backpressure at the outlet of the valve p_b is equal or lower than the pressure at the nozzle throat, the flow is choked at the nozzle throat and the critical pressure ratio is fixed. In case of a calorically perfect gas the critical pressure ratio η_{crit} equals

$$\eta_{crit} = \left(\frac{2}{\kappa_0 + 1} \right)^{\frac{\kappa_0}{\kappa_0 - 1}}. \quad (2.10)$$

For even lower backpressures or lower pressure ratios no further increase in discharge capacity can be achieved and shocks occur after the throat until the flow is completely supersonic until the outlet.

At high pressures (or low temperatures) the gas cannot be considered to behave as a perfect gas anymore, so that the stagnation properties deviate from the calorically perfect gas approximation and have to be calculated employing a real-gas EoS. Then, the density is corrected with a compressibility factor Z and the adiabatic exponent κ has to be calculated with a real-gas EoS as well. The derivation of real-gas nozzle flow models will be presented in the next section.

The flow can be considered incompressible when the maximum flow velocity is approximately one order lower than the speed of sound of the fluid. Then the discharge capacity is calculated with the Bernoulli equation for incompressible flow with a correction factor for effects of viscosity (wall friction) K_v . The dimensionless flow coefficient for liquids C_l is

$$C_l = K_v \sqrt{1 - \eta}. \quad (2.11)$$

Since the flow is considered incompressible the backpressure p_b always limits the throughput. The viscosity correction factor K_v for water equals unity. At high pressures the density is no longer constant but significantly varies with pressure according to Roberts (2006) [56]

$$p = p_{amb} + a^2(\rho - \rho_{amb}), \quad (2.12)$$

where the speed of sound a depends on the bulk modulus K and the pressure p_{amb} and density ρ_{amb} at standard temperature and pressure

$$a = \sqrt{K/\rho_{amb}}. \quad (2.13)$$

The resulting density for calculating the mass flow rate in equation (2.2) for liquids yields

$$\rho = \rho_{amb} \left(\frac{p - p_{amb}}{K} + 1 \right). \quad (2.14)$$

2.2 Real-gas material definition

For the standardized valve sizing method the density ρ and the adiabatic exponent κ at the valve inlet need to be accurately known in the region where real-gas effects are significant. Also for the alternative sizing methods (section 2.5) and especially for the numerical tool (chapter 3) more parameters are necessary. This section presents the parameters related to the standardized valve sizing method. The following section focuses on the parameters used in the numerical tool and partially in the alternative sizing methods.

An accurate database for thermodynamic properties of pure gases is tabulated in IUPAC (2008) [31] with pressures up to 10000 bar. In order to calculate real-gas flows at pressures up to 3600 bar with the CFD code the temperature has to range from 100 to 6000 K and the pressure from 0.01 to 10000 bar for numerical stability during the iterative solution process. In addition, it is essential that all data points are all thermodynamically consistent with each other so that a unique solution can exist at each integration point. However, the IUPAC tables only partially cover this region and with less points than necessary for the CFD code. Moreover, linear interpolation close to the critical point and extrapolation to low and high temperatures would lead to inconsistencies and failure of the solver of the numerical method. As a result, it is chosen to use an EoS to generate the points in the extreme large pressure and temperature region with the focus on thermodynamic consistency.

The cubic Redlich-Kwong (RK) EoS relates the pressure to the temperature and specific volume of a supercritical gas. This equation was extended by Soave for improved accuracy for larger and polar molecules. For many gases the coefficients of this EoS are well tabulated and with the help of mixing rules this EoS can also be applied to gas mixtures, which is beneficial for practical applicability of the valve sizing models and the numerical tool.

The Soave Redlich-Kwong (SRK) EoS has not been developed for pressures above 1000 bar, so it is chosen to compare the thermodynamic property compressibility factor Z and the specific heat capacity c_p with accurate data tables from IUPAC (2008) [31] to ensure accuracy in the wide range of interest. All other properties depend on these two parameters, which will be explained in the next section. The compressibility factor Z equals

$$Z = \frac{pv}{R_s T} \quad (2.15)$$

with v the specific volume per unit of mass equal to $1/\rho$. The SRK EoS is defined as

$$Z = \frac{v}{v-b} - \frac{a\alpha}{R_s T(v+b)}, \quad (2.16)$$

where the coefficients a , b and acentric factor ω are functions of the specific gas constant R_s , pressure p and temperature T , critical pressure p_c , critical temperature T_c (Soave, 1972) [64].

$$a = 0.42747 \frac{R_s^2 T_c^2}{p_c} \quad (2.17)$$

$$b = 0.08664 \frac{R_s T_c}{p_c} \quad (2.18)$$

$$\alpha = [1 + (0.480 + 1.574\omega - 0.176\omega^2)(1 - T_r^{0.5})]^2 \quad (2.19)$$

$$(2.20)$$

Soave has introduced a generalized correlation for the acentric factor ω

$$\omega = -1 - \log_{10}(p_r)_{T_r=0.7}. \quad (2.21)$$

The thermodynamic properties of different gases can be compared with each other by expressing the properties in terms of reduced pressure p_r and reduced temperature T_r :

$$p_r = \frac{p}{p_c} \quad (2.22)$$

$$T_r = \frac{T}{T_c} \quad (2.23)$$

The adiabatic exponent κ is defined as the ratio of isentropic pressure-density fluctuations

$$\kappa = -\frac{v}{p} \left(\frac{\partial p}{\partial v} \right)_s. \quad (2.24)$$

For real gases according to Rist (1996) [55]

$$\kappa = \frac{c_p}{c_p[1 - K_p] - Z R_s [1 + K_T]^2}, \quad (2.25)$$

where K_p and K_T are derivatives of the compressibility factor Z , which are zero for perfect gases since then $Z = 1$

$$K_p = \left(\frac{p}{Z} \frac{\partial Z}{\partial p} \right)_T \quad (2.26)$$

$$K_T = \left(\frac{T}{Z} \frac{\partial Z}{\partial T} \right)_p. \quad (2.27)$$

2.3 Real-gas property table generation

This section presents the thermodynamic properties necessary for the numerical tool and partially for the alternative valve sizing methods. These properties are derived from the same SRK EoS (2.16) presented in the preceding section. In order to adequately compare the results of the valve sizing methods (section 2.7) and a CFD validation test case of a high-pressure nozzle flow (section 3.3) with each other, exactly the same material properties have to be used. Then, the EoS will not contribute to possible differences between results of the methods.

In the CFD program ANSYS CFX [4] a real-gas can be defined by the specification of nine fluid properties as functions of pressure and temperature given in table 2.1. The variables have to be specified in a number of points (p_i, T_j) with $i = 1 \cdots N_p$ and $j = 1 \cdots N_T$. The actual values will be bilinearly interpolated between the tabulated data points.

To be able to calculate all properties of table 2.1 intermediate partial derivatives

1	c_p	Specific heat at constant pressure
2	v	Specific volume
3	c_v	Specific heat at constant volume
4	$(\frac{\partial p}{\partial v})_T$	Pressure-specific volume derivative at constant temperature
5	a	Speed of sound
6	h	Specific enthalpy
7	s	Specific entropy
8	μ	Dynamic viscosity
9	λ	Thermal conductivity

Table 2.1. Thermodynamic properties for real-gas table generation in ANSYS CFX.

are necessary. From the SRK EoS (2.16) the specific volume v can be expressed as a function of the pressure p , temperature T in combination with the real-gas law (2.15). The derivatives of the compressibility factor with respect to pressure and temperature necessary for K_p and K_T are numerically evaluated with a second-order approximation, e.g.:

$$\frac{\partial Z}{\partial T} \cong \frac{Z(p, T + dT) - Z(p, T - dT)}{2dT} \quad (2.28)$$

$$\frac{\partial^2 Z}{\partial T^2} \cong \frac{Z(p, T + dT) - 2Z(p, T) + Z(p, T - dT)}{dT^2}, \quad (2.29)$$

where the temperature perturbation dT is sufficiently small to obtain a solution independent of dT . Also other thermodynamic properties can be evaluated directly from

the EoS:

$$\frac{\partial \rho}{\partial p} = -\frac{\rho}{Z} \frac{\partial Z}{\partial p} - \frac{Z}{p} \quad (2.30)$$

$$\frac{\partial p}{\partial v} = -\frac{\rho^2}{\frac{\partial \rho}{\partial p}} \quad (2.31)$$

$$\frac{\partial \rho}{\partial T} = -\frac{\rho}{p} \frac{Z + T \frac{\partial Z}{\partial T}}{T \frac{Z}{p}} \quad (2.32)$$

$$\frac{\partial^2 v}{\partial T^2} = 2 \frac{\partial Z}{\partial T} \frac{R_s}{p} + R_s \frac{T}{p} \frac{\partial^2 Z}{\partial T^2} \quad (2.33)$$

In order to calculate the thermodynamic properties as a function of p and T it is chosen to combine the EoS (2.16) with the specific heat capacity at constant pressure c_p as a function of temperature at one value of the pressure p_{ref} . This is the minimal set of information wherefrom all thermodynamic states in the whole pressure and temperature domain can be derived in a thermodynamically consistent way, i.e. by obeying the Maxwell relations. It is convenient to choose p_{ref} as low as possible, so that the fluid is in the gas phase for all values of T at this pressure.

The first law of thermodynamics for the specific enthalpy difference dh (2.41) reads in combination with the general real-gas EoS

$$dh = c_p dT - K_T v dp. \quad (2.34)$$

The specific enthalpy can now be calculated at any combination of p and T from (2.34) with the trapezoidal rule:

$$h(p, T) = h_{ref} + \int_{T_{ref}}^T c_p(p_{ref}, \tilde{T}) d\tilde{T} - \int_{p_{ref}}^p K_T(\tilde{p}, \tilde{T}) v(\tilde{p}, \tilde{T}) d\tilde{p}, \quad (2.35)$$

where $h_{ref} = h(p_{ref}, T_{ref})$ is a reference value. The specific heat c_p can be derived in a similar way by using the Maxwell relation

$$\frac{\partial c_p}{\partial p} = \frac{\partial}{\partial T} \left(v - T \left(\frac{\partial v}{\partial T} \right)_p \right). \quad (2.36)$$

For numerical stability of high-pressure calculations up to 3600 bar with CFD it is necessary that the pressure of the real-gas property table ranges from 0.01 to 10000 bar and the temperature from 100 to 6000 K. However, the IUPAC tables supply data from 10 bar onwards with a limited temperature range, so an alternative reference source has to be used for lower pressures and higher temperatures. For a large number of species thermochemical data is available (NIST, 2009) [49], where for nitrogen the heat capacity at constant pressure per unit quantity of mass is directly tabulated with 0.3 to 0.8% uncertainty at low temperatures up to 2000 K and at a constant reference pressure of 0.01 bar. For higher temperatures from 298 up to 6000 K a polynomial fit from the same database is used

$$c_p = (A + B\hat{T} + C\hat{T}^2 + D\hat{T}^3 + E/\hat{T}^2)/M \quad (2.37)$$

with temperature $\hat{T} = 10^{-3}T$, molar mass $M = 28.014 \times 10^{-3}$ kg/mol, coefficients $A = 26.092$ J/(mol K), $B = 8.218801$ J/(mol K²), $C = -1.976141$ J/(mol K³), $D = 0.159274$ J/(mol K⁴) and $E = 0.044434$ J K/mol valid for a reference pressure of 1 bar. The high-temperature polynomial is slightly shifted to match the tabulated data at the lower reference pressure of 0.01 bar. Hereafter, three fifth-order polynomial fits with ranges 100-400 K, 400-1010 K and 1010-6000 K are defined to achieve the highest accuracy for calculation of the internal real-gas property table points (p_{ref}, T) with the function

$$c_p = \hat{A}T^5 + \hat{B}T^4 + \hat{C}T^3 + \hat{D}T^2 + \hat{E}T + \hat{F}. \quad (2.38)$$

Table 2.2 provides the coefficients for the three fifth-order polynomials in the whole temperature range 100-6000 K at the reference pressure of 0.01 bar.

The accuracy of the calculated compressibility factor Z and specific heat capacity

T [K]	$10^{12}\hat{A}$ [$\frac{J}{kg K^6}$]	$10^9\hat{B}$ [$\frac{J}{kg K^5}$]	$10^6\hat{C}$ [$\frac{J}{kg K^4}$]	$10^3\hat{D}$ [$\frac{J}{kg K^3}$]	$10\hat{E}$ [$\frac{J}{kg K^2}$]	$10^{-3}\hat{F}$ [$\frac{J}{kg K}$]
100-400	-3.516090	5.935904	-3.150280	0.760534	-0.086934	1.042872
400-1010	0.422704	-1.204028	0.866450	0.333386	-0.355100	1.103862
1010-6000	0.000278	-0.005100	0.040772	-0.181417	0.446863	0.866319

Table 2.2. Polynomial coefficients of c_p of nitrogen in three temperature ranges at $p_{ref} = 0.01$ bar.

at constant pressure c_p is compared with IUPAC (2008) [31] reference data in figure 2.1 for nitrogen. It is assumed that the other thermodynamic properties in table 2.1 will have the same order of accuracy. It can be seen that for reduced temperatures $T_r > 1.5$ the accuracy of both variables is within 5% at pressures up to 3600 bar. This is the highest valve inlet pressure to be calculated with the numerical method. Closer to the critical point where the gradients of the variables are large the deviation is up to 10%. Especially at the lowest temperature the parameter Z shows large variations so that deviations of the EoS turn into larger deviations of the c_p . In the comparison of the results of the valve sizing models at high pressures in section 2.7 the temperature at the nozzle inlet is increased to 150 K ($T_r = 1.18$) so that the flow should not condense in the nozzle throat. Also in the extrapolation of the numerical CFD model in section 5.3 the valve inlet temperature has to be further increased to 175 K ($T_r = 1.39$) so that the temperature at the smallest cross-section remains above the critical temperature for which the deviations are smaller.

The heat capacity ratio κ is calculated from equation (2.25). The specific heat

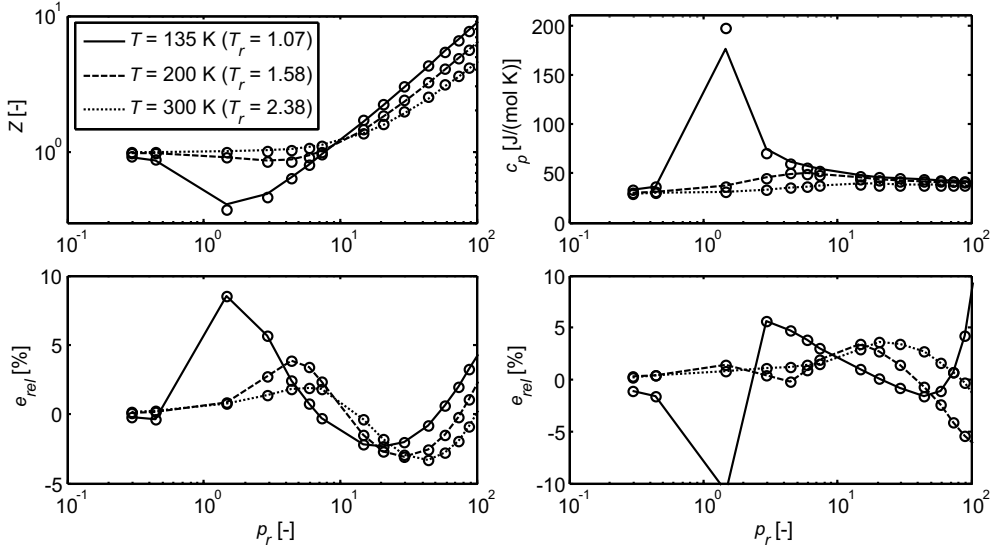


Figure 2.1. Comparison of calculated compressibility factor Z and specific heat capacity at constant pressure c_p with IUPAC data for nitrogen for three values of the reduced temperature. The circles in the two upper figures refer to the IUPAC data and in the two lower figures refer to the points of comparison.

capacity at constant volume c_v and the speed of sound a are derived from

$$c_v = ZR_s \frac{[1 + K_T]^2}{\kappa[1 - K_p]^2 - [1 - K_p]} \quad (2.39)$$

$$a = \sqrt{\left(\frac{\partial p}{\partial \rho}\right)_T + \frac{T}{\rho^2 c_v} \left(\left(\frac{\partial \rho}{\partial T}\right)_p\right)^2}. \quad (2.40)$$

For higher pressures the specific enthalpy h

$$dh = c_p dT + \left[v - T \left(\frac{\partial v}{\partial T}\right)_p \right] dp \quad (2.41)$$

and the specific entropy s

$$ds = c_p \frac{dT}{T} - \left(\frac{\partial v}{\partial T}\right)_p dp. \quad (2.42)$$

are numerically integrated using the trapezoidal rule.

The dynamic viscosity $\mu(p, T)$ in [Pa s] is defined according to the rigid, non-interacting sphere model (Reid, 1966) [52] with the molar mass M in [kg/mol], the

temperature in [K] and the critical volume V_c in [m³/mol].

$$\mu = 10^{-7} 26.69 \frac{\sqrt{1000MT}}{\sigma^2} \quad (2.43)$$

$$\sigma = 0.809 V_c^{1/3} \quad (2.44)$$

The thermal conductivity $\lambda(p, T)$ is defined according to the modified Eucken model (Reid, 1966) [52] as

$$\lambda = \mu c_v \left(1.32 + 1.77 \frac{R_s}{c_v} \right). \quad (2.45)$$

The CFD solver ANSYS CFX does not permit the real-gas property data to come into the subcooled liquid region, so that the EoS can only be used in the vapor and supercritical region. This region is bounded by the saturated vapor pressure curve up to the critical point and needs to be specified. For instance, at pressures lower than the critical pressure, when during iteration of the numerical method the temperature stored at a certain grid node would become beyond the saturation temperature at that pressure, the solution variables of that grid node will be clipped to the values at that saturation pressure. Furthermore, at pressures higher than the critical pressure, when during iteration the temperature falls below the critical temperature, the solution variables stored at the grid nodes of the CFD code will be clipped to values in the real-gas tables at the critical temperature T_c .

The saturated vapor pressure curve according to Gomez-Thodos (Reid, 1966) [52] crosses the critical point and is given by

$$p_{sat} = 10^{-5} p_c \exp\left(\beta \left[\frac{1}{T_r^m} - 1\right] + \gamma [T_r^7 - 1]\right) \quad (2.46)$$

with the parameters β , m and γ depending on the critical pressure p_c , critical temperature T_c and boiling temperature T_b of the gas.

At pressures higher than the critical pressure and close to the critical temperature the calculation of the adiabatic exponent κ becomes undefined, because in equation (2.25) the denominator becomes zero. Therefore, in the real-gas property tables for nitrogen the saturated vapor pressure curve is proportionally shifted to cross an artificial critical temperature with $T_{r,shift} = 1.05 T_r$ from which the solution variables are continuous (figure 2.2 left). That means that for the numerical CFD tool the artificial critical temperature for nitrogen is increased from the physical value of 126.2 K (plus symbol) to the artificial value of 132.5 K. The lower temperature limit of the property tables is set to 100 K.

The right part of figure 2.2 shows the temperature shift of the critical point (bullet) to the continuous solution of the specific heat at constant pressure c_p versus temperature at a constant pressure of 50 bar. The 25 bar point (triangle) lies on the vapor pressure curve. Although the 5 bar point (diamond) is below the vapor pressure curve the temperature is clipped to the minimum table limit. For each property the pressure in the table ranges from 10³ to 10⁹ Pa and is logarithmically divided into 400 points. The temperature ranges from 100 to 6000 K and is linearly divided into 400 points. These wide ranges are necessary to stabilize the solver of ANSYS CFX during iteration.

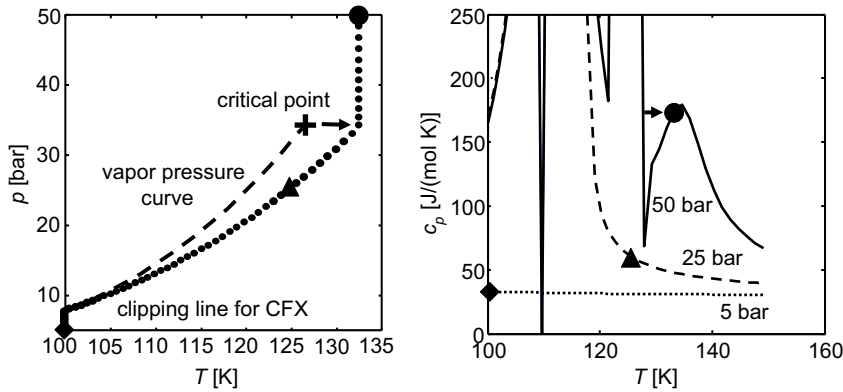


Figure 2.2. Modified vapor pressure curve for clipping solution variables in ANSYS CFX for nitrogen.

2.4 Applicability to other gases

According to the principle of corresponding states [46] the compressibility factor Z of a gas can be expressed as a function of the reduced pressure p_r and reduced temperature T_r defined in equations (2.22) and (2.23). When the compressibility factors of various pure gases are plotted versus reduced pressure for various temperatures, the isotherms for different gases with equal reduced temperature coincide closely [46]. Figures 2.3 and 2.4 show two generalized compressibility charts for the reduced pressure ranges $p_r \leq 10.0$ and $10 \leq p_r \leq 40$ respectively. For 30 non-polar and slightly polar gases used in developing the chart the deviation is 5% at most and for lower pressures it is much less. For hydrogen, helium and neon for $T_r > 5$ an adapted formulation of the reduced properties is used, which reads $p_r = p/(p_c + 8)$ and $T_r = T/(T_c + 8)$ with pressures in atmosphere and temperatures in K. As can be seen the value of Z tends to unity for all temperatures when the pressure tends to zero which is the ideal gas law in equation (2.15).

The generalization of the gas dynamics for real gases indicates that the analysis achieved with nitrogen can be applied to other gases as long as the thermodynamic state is expressed in terms of reduced properties. For gas mixtures, such as natural gas, generalized compressibility charts can also be applied with mixing rules, using a mass fraction weighted average of the reduced pressure and temperature.

2.5 Literature review of valve sizing at high pressures

Before alternative valve sizing methods are proposed this section focuses on previous research carried out in the field of valve sizing at high pressures. Bober et al. (1990) [11] analytically investigated the influence of real-gas effects on the discharge coeffi-

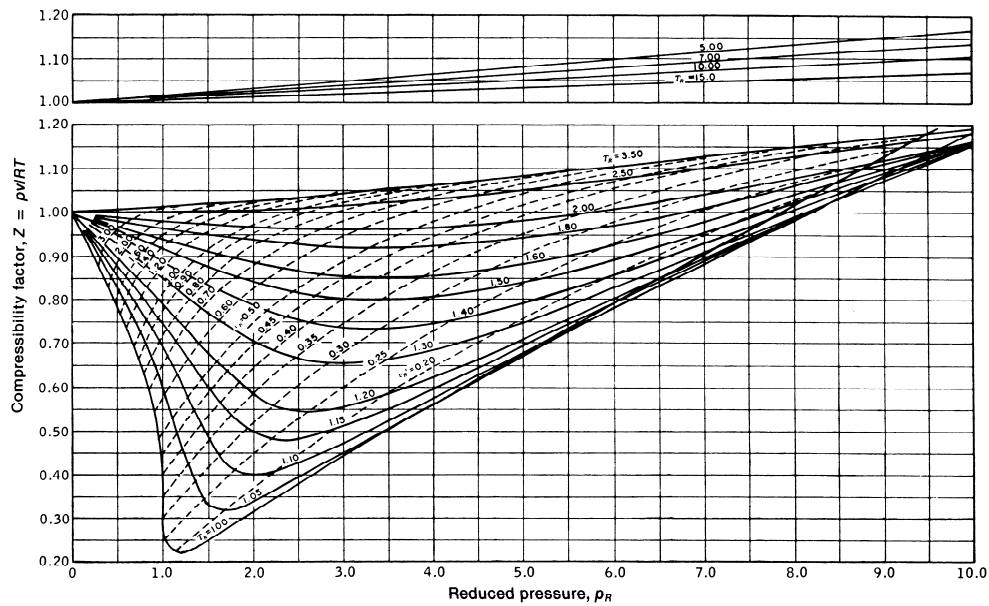


Figure 2.3. Generalized compressibility chart for $p_r \leq 10.0$ (Moran, 2006) [46]. Legend: solid = constant reduced temperature T_r ; dashed = constant pseudo-reduced specific volume $v'_r = v/(R_s T_c/p_c)$.

cient of choked nozzles. In their work an analytical method for non-ideal isentropic gas flow through converging-diverging nozzles based on the Redlich-Kwong EoS with the specific heat as function of temperature and pressure was developed. Choked mass flow rates between ideal gas and real-gas flow differed up to 19% for methane at a reduced pressure $p_{0,r} = 5$ and reduced temperature $T_{0,r} = 1.4$. It was concluded that the iteration scheme would be more efficient when the isentropic change between two thermodynamic states would be solved with temperature T and specific volume v as the independent variables instead of solving it as function of pressure.

Also Bauerfeind et al. (2003) [9] focused on an analytical method to calculate the local course of thermodynamic and fluid dynamic states of a real-gas in an adiabatic nozzle in order to calculate the maximum mass flow rate with variable dissipation effects. The local dissipation rate along the nozzle was estimated with functions for the loss coefficient depending on the shape of the nozzle. It was concluded that the mass flow rate through a critical nozzle can be calculated accurately enough with the simple isentropic state change of an ideal gas as presented in section 2.1, when the compressibility factor Z and the adiabatic exponent κ are arithmetically averaged between the fluid dynamic state at the inlet and the critical state at the nozzle throat. Closer to the critical point of the gas this approach is still accurate because the modeling errors compensate each other. The dissipation coefficients reduced from 0.975 for stagnation pressures below the critical pressure and to 0.95 for pressures above the critical point up to 160 bar. This dissipation effect is a relatively small error source in

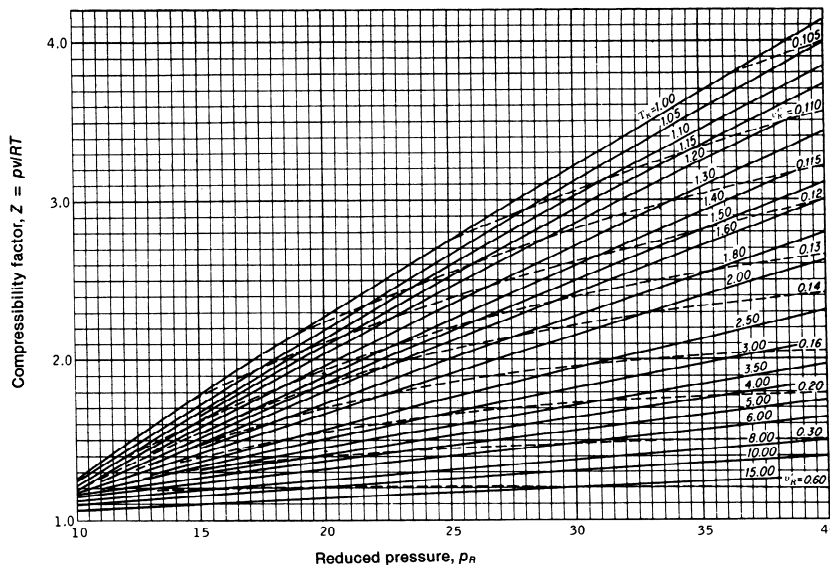


Figure 2.4. Generalized compressibility chart for $10 \leq p_r \leq 40$ (Moran, 2006) [46]. Legend: solid = constant reduced temperature T_r ; dashed = constant pseudo-reduced specific volume $v'_r = v/(R_s T_c / p_c)$.

comparison with the addition of real-gas effects in the nozzle flow model where mass flow rates of methane with the Redlich-Kwong EoS are calculated up to 36% higher at the stagnation state $1.5p_c$ and $1.1T_c$ than with the ideal gas EoS.

In a computational study of critical nozzle flow of high-pressure hydrogen gas of Kim et al. (2008) [33] experimental data was compared with results of a CFD model of a Venturi nozzle with adiabatic frictionless walls. It was reported that the discharge coefficient defined as the ratio between the theoretical mass flow rate according to critical isentropic ideal gas flow and the measured mass flow rate exceeds unity for Reynolds numbers below 6×10^5 . Numerical results showed that the location of the shock wave at $2.6D$ downstream of the nozzle throat moves $0.5D$ downstream due to real-gas effects. As a consequence, the mass flux distribution at the nozzle throat slightly changes as well, leading to an increase of the discharge coefficient up to 1.015. According to a numerical investigation of the discharge coefficient in critical nozzles of Johnson (1998) [32], the effect of a hot wall, where the nozzle wall is isothermal and has a temperature equal to the inlet temperature, is smaller than 0.28% in the case of Argon gas at low Reynolds numbers of 4000.

In the investigation of Luft et al. (2007) [39], the polymerization of ethylene was selected to calculate the effective discharge area of safety valves operating at high temperatures and pressures up to 300 MPa. An isenthalpic pressure relief calculation of an autoclave with ethylene agreed well with experiment so that the rate of pressure decay could be predicted in a real application. To account for real-gas effects, it is recommended that the coefficient of discharge should be evaluated from relief

measurements under the conditions the valves are operated. However, this is only possible for small relief valves at laboratory scale and in particular hardly possible at industrial scale, so that a numerical tool is necessary for accurate valve sizing.

In contrast to the derivation of the real-gas critical nozzle flow model with dissipation of Bauerfeind it is expected that the pressure losses due to shocks should not be taken into account, since these occur after the choking plane and influence the critical pressure at the nozzle throat only at lower Reynolds numbers. Furthermore, in case of small pressure ratios the shock is located far downstream towards the nozzle exit. Then a small variation of the first shock does not influence the mass flux distribution in the nozzle itself. Also, the calculated dissipation coefficients have an averaged value of 0.96, which is small in comparison with the loss factors as given in the standard ISO 9300 [28] at high Reynolds numbers. The dissipation coefficients are up to 0.995 where the boundary layers are thin and are calibrated with experiments to achieve errors below $< 0.5\%$ in practice.

From the brief literature overview concerning recent investigations in the field of high-pressure valve sizing two ways for analytical determination of the mass flow rate of a choked nozzle with real-gas effects can be distinguished. In the first approach, referred to as *real-average* method, only the stagnation properties of the nozzle inlet or an arithmetical average between the inlet and the critical properties at the nozzle throat are used. This method is used by Bauerfeind et al. (2003) [9] based on recommendations of the American standard API RP520 (2000) [5] and extensively described by Rist (1996) [55]. In the second approach, referred to as *real-integral* method, the critical thermodynamic state is calculated iteratively with isentropic thermodynamic state change relations. This method was used by Bober et al. (1990) [11].

From a practical point of view it is desirable to have an accurate nozzle flow model that resolves real-gas effects without using iteration schemes. Then the discharge coefficient accounting for flow losses due to friction, separation and recirculation of the flow should depend only weakly on thermodynamic effects, such as real-gas effects, when the nozzle model already accurately captures this. In addition, the discharge coefficient K_d becomes essentially a geometry factor that is insensitive to the inlet temperature and pressure. The real-gas nozzle flow model delivers the flow coefficient C_g to calculate the mass flow rate in the general equation (2.2).

2.6 Alternative valve sizing methods

This section presents two alternative valve sizing methods based on both approaches. In section 2.7 the results of these methods are compared with the standardized valve sizing method. In section 3.3 the performance of the three valve sizing methods and also CFD results will be compared with experimental data from a high-pressure nozzle flow. It is emphasized that for each valve sizing method the same real-gas definition described in sections 2.2 and 2.3 are used to minimize influences from inaccuracies of the EoS used.

The derivation of both analytical nozzle methods starts with the first law of ther-

thermodynamics for the specific enthalpy difference dh (2.41) which results in combination with the general real-gas EoS in equation (2.34). With the help of the second law of thermodynamics the specific entropy ds equals (2.42). For an isentropic flow, $ds = 0$, the enthalpy difference becomes [59]

$$dh_{is} = ZR_s \frac{c_p}{1 + K_T} dT = ZR_s \frac{\kappa[1 + K_T]}{\kappa[1 - K_p] - 1} dT = \frac{ZR_s}{\Pi} dT, \quad (2.47)$$

where

$$\Pi = \frac{\kappa[1 - K_p] - 1}{\kappa[1 + K_T]}. \quad (2.48)$$

In an adiabatic isentropic nozzle the specific total enthalpy remains constant, so that the enthalpy difference can be integrated from the nozzle inlet with velocity zero to the nozzle throat

$$\int_0^{throat} dh = -u^2/2, \quad (2.49)$$

where u is the velocity in the throat. The locations of both thermodynamic states in a truncated nozzle are shown in figure 2.5. In reality, viscous effects and heat

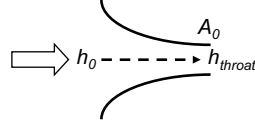


Figure 2.5. Enthalpy change of a flow in a truncated nozzle.

conduction always result in entropy production. As a consequence, for a convergent adiabatic nozzle flow the enthalpy change with enthalpy production Δh yields [55]

$$\int_0^{throat} dh = -u^2/2 + \Delta h. \quad (2.50)$$

For a frictionless nozzle flow the mass flow rate $\dot{m}_{g,nozzle}$ equals

$$\dot{m}_{g,nozzle} = \frac{A_0}{v} \sqrt{-2 \int_0^{throat} dh} \equiv C_g A_0 \sqrt{2 \frac{p_0}{v_0}} \quad (2.51)$$

with throat area A_0 , specific volume v , dimensionless flow coefficient C_g and total pressure p_0 that equals the definition of equation (2.2). An isentropic change of state of a real-gas without friction reads

$$C_g = \frac{v_0}{v} \sqrt{\frac{-\int_0^{throat} dh_{is}}{v_0 p_0}}. \quad (2.52)$$

First alternative valve sizing method: *real-average*

In the first approach, referred to as *real-average* method, the enthalpy integral is solved by arithmetically averaging all variables between the total state at the inlet and the static state at the nozzle throat, where the enthalpy is maximum. This approach has been published in Schmidt et al. (2009) [59].

$$C_g = \frac{v_0}{v} \sqrt{\frac{1}{\Pi_m} \frac{Z_m}{Z_0} \left(1 - \frac{T}{T_0}\right)} \quad (2.53)$$

with the mean values according to Rist (1996) [55]

$$\kappa_m = (\kappa + \kappa_0)/2 \quad (2.54)$$

$$Z_m = (Z + Z_0)/2 \quad (2.55)$$

$$K_{p,m} = (K_p + K_{p,0})/2 \quad (2.56)$$

$$K_{T,m} = (K_T + K_{T,0})/2 \quad (2.57)$$

$$\Pi_m = \frac{\kappa_m[1 - K_{p,m}] - 1}{\kappa_m[1 + K_{T,m}]} \quad (2.58)$$

The isentropic relations for real gases are

$$\frac{T}{T_0} = \left(\frac{p}{p_0}\right)^{\Pi_m} \quad (2.59)$$

$$\frac{v_0}{v} = \left(\frac{p}{p_0}\right)^{\frac{1}{\kappa_m}} \quad (2.60)$$

With the coefficient φ accounting for viscous effects and heat conduction, the dimensionless flow coefficient for real gases as function of the pressure ratio $\eta = p/p_0$ with pressure p at the nozzle throat becomes

$$C_g = \varphi \sqrt{\frac{1}{\Pi_m} \frac{Z_m}{Z_0} \eta^{\frac{2}{\kappa_m}} (1 - \eta^{\Pi_m})}. \quad (2.61)$$

By differentiating this equation with respect to the pressure ratio the maximum value of C_g is formed for the pressure ratio

$$\eta_{crit} = \left[\frac{2}{2 + \Pi_m \kappa_m} \right]^{\frac{1}{\Pi_m}} \quad (2.62)$$

When this critical pressure ratio is smaller than the backpressure ratio $\eta_b = p_b/p_0$ the flow is choked. The critical pressure ratio has to be determined iteratively because it depends on the thermodynamic properties of the critical state as well. As initial guess the ideal gas critical ratio can be used, which is equation (2.62) with $K_{p,m} = K_{T,m} = 0$ so that $\Pi_{m,ideal} = (\kappa_0 - 1)/\kappa_0$. When the critical pressure ratio is larger than the backpressure ratio the flow remains subsonic and the dimensionless flow coefficient can be directly calculated with the actual backpressure ratio.

Second alternative valve sizing method: *real-integral*

In the second approach, referred as *real-integral* method, the enthalpy integral (2.52) is evaluated by subsequently calculating the isentropic state change from the total state condition at the inlet to the final critical state. In each sequence the temperature is decreased with a sufficiently small amount until the derivative of the flow coefficient C_g at state i approaches zero.

$$C_{g,crit,i} = \varphi \left(\frac{v_0}{v_i} \right) \sqrt{\frac{h_0 - h_i}{v_0 p_0}} \quad (2.63)$$

The corresponding pressure at state i is based on equation (2.42) with $ds = 0$ with

$$p_i = p_{i-1} + \frac{c_{p,i-1}}{T_{i-1} \left(\frac{\delta v}{\delta T} \right)_{i-1}} dT, \quad (2.64)$$

where the thermodynamic properties are based on the state of the previously calculated state $i - 1$. The temperature difference dT is given by

$$dT = T_i - T_{i-1}. \quad (2.65)$$

The same accounts for the enthalpy at state i based on equation (2.47)

$$h_i = h_{i-1} + \frac{Z_{i-1} R_s}{\Pi_{i-1}} dT. \quad (2.66)$$

This temperature controlled analytical model is sensitive to non-linearities of the thermodynamic properties close to the critical point. Alternatively, the enthalpy change at the locations where the flow coefficient is maximum can also be calculated with constant small decreasing pressure. This algorithm allows flow coefficient determination when the thermodynamic variables are partially discontinuous. When in a sequence of the calculation the pressure reaches the backpressure before the dimensionless flow coefficient has reached its maximum, the flow remains subsonic and the actual dimensionless flow coefficient corresponding to the applied backpressure ratio has to be used.

2.7 Comparison of valve sizing methods

The standardized ideal gas valve sizing method (*ideal* method) is compared with the two alternative real-gas sizing methods at choked flow conditions, where the thermodynamic variables are arithmetically averaged between the stagnation state at the inlet and the critical state at the nozzle throat in the *real-average* method and integrated between both states in the *real-integral* method. For pressures ranging from 0.1 to 2500 bar flow coefficient curves of the maximum value of the dimensionless flow coefficient at inlet temperatures of 150 and 300 K for each sizing method for nitrogen are given in figure 2.6.

At low reduced pressures all three analytical methods yield a similar flow coefficients $C_g = 0.48$, because no real-gas effects occur and the flow behaves as an

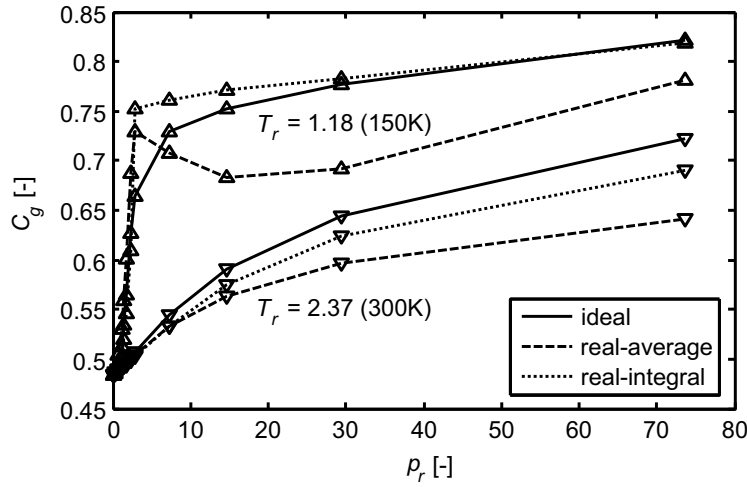


Figure 2.6. Dimensionless flow coefficient of three different analytical methods, for two values of reduced temperatures T_r , versus reduced pressure p_r for nitrogen at choked flow conditions. The lines are only connected to guide the eye.

ideal gas and the temperature influence is small. At the low reduced temperature $T_r = 1.18$ all three methods show a sharp increase in the flow coefficient, where the *real-average* method decreases sharply around the critical pressure in contrast to the two other methods. At 2500 bar and the lowest reduced temperature the flow coefficient increases from 0.48 to 0.82 which is an increase of 71%. The two highest values of the lowest reduced temperature curve are 5 and 10 K below the saturation temperature curve. This indicates that the flow could partially condense close to the nozzle throat.

Since the *real-integral* sizing method actually solves the enthalpy integral, it is closest to reality. However, the method still neglects friction, flow separation, heat transfer, 2D effects of the choking plane in the nozzle throat and assumes a homogeneous developed velocity profile. In a regularly shaped converging nozzle, it is expected that the flow is essentially fully developed, does not separate and therefore shows a flat choking plane. The effect of heat transfer is expected to be small since the flow is essentially adiabatic. The effects of friction, separation effects and 2D effects will be discussed in the comparison with computations of the numerical tool in section 3.3. Although the *ideal* method is the simplest model since no iterative calculations have to be made within the whole pressure and temperature range, it deviates only 3% from the most complex *real-integral* valve sizing method.

Chapter 3

Development of numerical tool

In this chapter the numerical method for valve characterizing is developed with CFD. In section 3.1, the mathematical models, the discretization and the solution method of the numerical method will be given. Then in section 3.2, a suitable CFD software package will be chosen and its model parameters will be determined with the help of validation test cases based on low-pressure reference data from literature. In section 3.3, the performance of the CFD method as well as the valve sizing methods from the preceding chapter will be validated with measurement data from a high-pressure nozzle flow.

3.1 Numerical valve model parameters

Computational fluid dynamics is applied as a numerical tool to describe the flow through safety valves. The numerical tool comprises partial differential equations (PDE) representing the physics of the flow, which are solved for small control volumes defined by a computational mesh. In the case of fluid flow the PDE system consists of the conservation equations for the mass, momentum and energy. Before CFD can be applied it is important to know which physical phenomena dominate the flow within a safety valve and with which physical models the Navier-Stokes equations have to be completed. Then, the computational domain has to be specified so that at the boundaries the flow variables are prescribed or follow from boundary conditions. The considered valve geometry will be decomposed into small volumes, where the elements should be small in flow regions with large gradients of the flow variables. The coupled non-linear algebraic equations resulting from discretization of the governing PDE's must be solved iteratively until a certain convergence criterion is met. Then a solution of the flow problem is achieved that can be analyzed in a post-processor. From the computed flow field the desired information can be extracted, such as integral computed variables that can be compared with experimental data.

3.1.1 Mathematical models

To describe the 3D flow phenomena in a safety valve, the conservation laws of mass, momentum and energy are used in a set of equations known as the unsteady Navier-Stokes equations which are solved by a commercial software package ANSYS CFX in their conservation form [4]. The continuity equation with density ρ and velocity vector \mathbf{u} is

$$\frac{\partial \rho}{\partial t} + \nabla \cdot (\rho \mathbf{u}) = 0. \quad (3.1)$$

The momentum equations with pressure p , in absence of volumetric forces yields

$$\frac{\partial(\rho \mathbf{u})}{\partial t} + \nabla \cdot (\rho \mathbf{u} \mathbf{u}) = -\nabla p + \nabla \cdot \tau \quad (3.2)$$

with assuming a Newtonian fluid the stress tensor τ related to the strain rate by

$$\tau = \mu \left(\nabla \mathbf{u} + (\nabla \mathbf{u})^T - \frac{2}{3} \delta \nabla \cdot \mathbf{u} \right). \quad (3.3)$$

Here Stokes' hypothesis that τ has a zero trace is used to relate the second viscosity to the dynamic viscosity. The total energy equation with Fourier's law of heat conduction is

$$\frac{\partial \rho h_0}{\partial t} - \frac{\partial p}{\partial t} + \nabla \cdot (\rho \mathbf{u} h_0) = \nabla \cdot (\lambda \nabla T) + \nabla \cdot (\mathbf{u} \cdot \tau), \quad (3.4)$$

where total enthalpy $h_0 = h + \frac{1}{2} \mathbf{u}^2$ and the term $\nabla \cdot (\mathbf{u} \cdot \tau)$ represents the work due to viscous stresses. The volumetric heat sources are neglected. For low velocities or incompressible flows the density is approximately constant and the continuity equation reduces to

$$\nabla \cdot \mathbf{u} = 0. \quad (3.5)$$

The conservation equations have to be completed with definitions of the fluid properties in the form of a thermal EoS, which describes the relation between the thermodynamic parameters pressure, density and temperature of the fluid. Also a caloric EoS expressing the internal energy as a function of two independent thermodynamic parameters and the transport properties dynamic viscosity μ and thermal conductivity λ of the fluid are necessary. Section 2.5 focuses on material properties for high pressures.

The Navier-Stokes equations can be solved directly numerically (DNS) when the numerical grid is sufficiently fine. Then, all spatial and time scales must be resolved in the computational mesh from the smallest dissipative scales up to the integral scale associated with the motions containing most of the kinetic energy. However, turbulence occurs at much smaller scales than can actually be resolved in practical applications. Also for engineering purposes only the time-averaged flow quantities and not the fluctuations are of interest. To obtain an approximate solution, the Reynolds-Averaged Navier-Stokes (RANS) equations are used. In this approach, the flow quantities are decomposed in a mean (ensemble-average) and a fluctuating part. For example, at each location \mathbf{x} at time t the velocity $\mathbf{u}(\mathbf{x}, t)$ is decomposed into the time-averaged

$\bar{\mathbf{u}}$ value denoted by an overbar and the random fluctuating component of motion \mathbf{u}' denoted by a prime

$$\mathbf{u}(\mathbf{x}, t) = \bar{\mathbf{u}}(\mathbf{x}) + \mathbf{u}'(\mathbf{x}, t). \quad (3.6)$$

Substituting this decomposition in the Navier-Stokes equation and time-averaging, results for the averaged equation of momentum

$$\frac{\partial \bar{\rho \mathbf{u}}}{\partial t} + \nabla \cdot (\bar{\rho \mathbf{u} \mathbf{u}}) = \nabla \cdot (\bar{\tau} - \bar{\rho \mathbf{u}' \mathbf{u}'}). \quad (3.7)$$

In the averaged partial differential equations cross-correlations of the turbulent fluctuations appear as new terms. These terms are called the Reynolds stresses $-\bar{\rho \mathbf{u}' \mathbf{u}'}$ and the Reynolds heat flux $-\bar{\rho \mathbf{u}' h'}$ for the averaged energy equation and constitute nine new unknowns, which means that the system is not closed anymore.

A solution is to approximate the Reynolds stress tensor and the turbulent heat flux term with a turbulence model depending on the type of flow. There is a large variety of models, but all these models have in common that they introduce uncertainties. The main difference between these turbulence models is their complexity. In engineering flows, eddy viscosity based models are the simplest level of closure that does not require geometry or flow regime as input with a reasonable compromise between computational effort and physical accuracy. Herein, the Boussinesq approximation assumes that the Reynolds stresses are proportional to the eddy or turbulent viscosity μ_t and the mean velocity gradients

$$-\bar{\rho \mathbf{u}' \mathbf{u}'} = \mu_t (\nabla \bar{\mathbf{u}} + (\nabla \bar{\mathbf{u}})^T) - \frac{2}{3} \delta (\rho k + \mu_t \nabla \cdot \bar{\mathbf{u}}), \quad (3.8)$$

with turbulent kinetic energy k defined as

$$k = \frac{1}{2} \overline{u'^2}. \quad (3.9)$$

The gradient-diffusion hypothesis relates the Reynolds fluxes of a scalar linearly to the mean scalar gradient

$$-\bar{u' h'_0} = -\Gamma_T \nabla \bar{h}_0, \quad (3.10)$$

where Γ_T is the eddy diffusivity as a function of the turbulent Prandtl number Pr_T

$$\Gamma_T = \frac{\mu_t}{Pr_T}. \quad (3.11)$$

The turbulent Prandtl number is defined as a function of the mean velocity and temperature gradients, the turbulent shear stress $\bar{u'v'}$ and the turbulent heat flux $\bar{v'T'}$

$$Pr_T = \frac{\bar{u'v'}}{\bar{v'T'}} \frac{\partial \bar{T}}{\partial y} \bigg/ \frac{\partial \bar{u}}{\partial y}, \quad (3.12)$$

which is a prescribed dimensionless quantity. Two-equation models provide the turbulent viscosity μ_t so that the turbulence is expressed in terms of mean variables. The most popular version of the two-equation model is the $k - \epsilon$ model, where ϵ is the

rate at which turbulent energy is dissipated into smaller eddies (Jones and Launder, 1972) [32]

$$\mu_t = C_\mu \rho \frac{k^2}{\epsilon}, \quad (3.13)$$

where C_μ is a dimensionless quantity. The values of k and ϵ are computed from two partial differential transport equations for the turbulence kinetic energy and turbulence dissipation rate. The $k - \epsilon$ model is less sensitive to the free stream values of ϵ , but is often inadequate in flows with adverse pressure gradients such as in safety valves.

The second most widely used type of turbulence model is the $k - \omega$ model of Wilcox (1993) [69], where ω is the frequency of the largest eddies. The $k - \omega$ model assumes that the turbulent viscosity μ_t is related to the turbulence kinetic energy and turbulent frequency via

$$\mu_t = \rho \frac{k}{\omega}. \quad (3.14)$$

The $k - \omega$ model performs well close to walls in boundary layers in strong adverse pressure gradients. However, it is sensitive to the free stream value of ω and unless great care is taken to set this value, inaccurate results can be found in both the boundary layer and shear flows.

An interesting option is a combination of the two models, which is called the Baseline (BSL) model (Menter, 1994) [42]. In this model the properties of the $k - \omega$ model close to the wall and the performance of the $k - \epsilon$ model in the free shear flow are retained by a gradual blending of the two models from the wall to the free stream. The BSL model combines the advantages of the $k - \omega$ and $k - \epsilon$ model, but still fails to properly predict the onset and extent of flow separation from smooth surfaces. The main reason is that both models do not account for the transport of turbulent shear stress. This results in an overprediction of the eddy viscosity. A limiter in the formulation of the eddy viscosity can obtain the proper transport behavior. This approach is known as the shear stress transport (SST) model, proposed by Menter (1994) [42]. This SST model is considered as the best two-equation turbulence model to predict the turbulent flow effects under the influence of adverse pressure gradients, non-equilibrium boundary layer regions as those found behind shocks, or close to regions with flow separation.

Two-equation RANS turbulence models are only valid in developed turbulent bulk flows at high Reynolds numbers. Adjacent to the wall in the boundary layer turbulent fluctuations are suppressed and viscous flow effects become important. Also high flow gradients would require a high grid density to accurately resolve the boundary layer. Commonly used empirical wall functions model the viscous sub-layer and the log-law zone of the boundary layer so that they overcome the inaccuracy of the turbulence model and the necessity of a fine grid at the wall. For smooth walls the laminar viscous sub-layer has the velocity profile

$$u(y) = y \frac{\tau_w}{\mu} \quad (3.15)$$

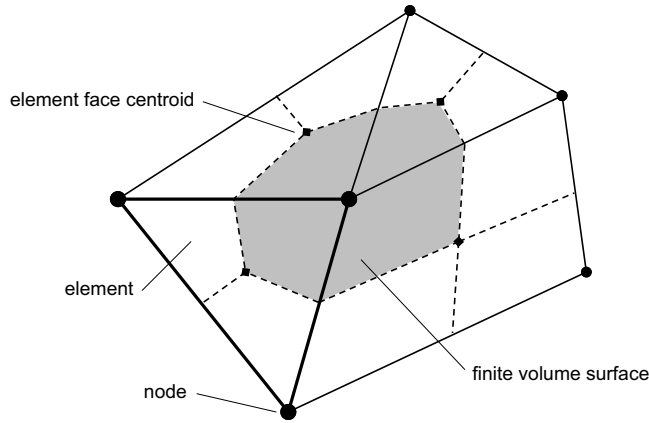


Figure 3.1. 2D representation of polyhedral mesh.

where y is the distance to the wall and u the velocity component parallel to the wall, τ_w the wall shear stress and μ the dynamic viscosity. The logarithmic law-of-the-wall functions model the log-law zone of the boundary layer

$$u(y) = \sqrt{\frac{\tau_w}{\rho}} \left(\frac{1}{\kappa} \ln y^+ + C \right), \quad (3.16)$$

where κ is the von Karman constant and C is a log-layer constant depending on wall roughness. The dimensionless wall-normal coordinate y^+ equals

$$y^+ = \frac{y\rho}{\mu} \sqrt{\frac{\tau_w}{\rho}}. \quad (3.17)$$

At the first grid point from the wall, this quantity should have a value between 30 and 300 to calculate the mesh spacing within the logarithmic layer of the boundary layer.

3.1.2 Discretization and solution method

In most commercial CFD software packages, the control volumes are defined around the generated grid nodes of the mesh. This means that when a mesh is generated with prism, tetrahedral and/or hexahedral shaped cells connected to the nodal points at their edges, the polyhedral volume is generated by surfaces constructed from element face centroids and middle of the element line points (figure 3.1 [4]). The discretization accuracy is highest when the surfaces of the polyhedral volume cells are almost perpendicular and parallel to the flow. Structured grids with hexahedral elements adjacent to the wall meet this condition, because these have node positions along the streamlines of the flow resulting in a minimum discretization error. Structured grids are therefore used in boundary layers, where it is important that the distance to the

walls, the dimensionless wall-normal coordinate y^+ is kept at a constant value to meet the requirements for near-wall turbulence modeling. For high-pressure compressible flows the boundary layers are thin so that the height of the first cell at the boundary wall has to be up to 1000 times smaller in comparison with transonic flow at atmospheric conditions or incompressible flows.

For complex valve geometries a structured mesh is not possible without dividing the volume into blocks to generate a block-structured mesh. The cells at the corners of the block are optimal, but the drawback is that at the edges between two blocks in the bulk flow the cells become too stretched which can cause numerical instabilities. Unstructured hexahedral grids are the compromise between geometrical flexibility and the possibility to refine the mesh locally without deteriorating the mesh quality. A further advantage of using hexahedral mesh elements is that the memory usage is up to four times smaller and the computational time up to 1.6 times shorter than for a tetrahedral mesh with equivalent accuracy according to FEM calculations of Tsuboi (2001) [67].

At the surfaces of a meshed computational domain boundary conditions have to be imposed. Since a safety valve flow involves high velocities the heat exchange with the walls is negligible so that the wall can be considered as adiabatic. At the enlarged inlet and outlet of a safety valve flow the velocities are low so that the stagnation pressure and temperature are well-defined which can directly be specified at these boundaries. In case of compressible flows with unknown inlet velocity profile or mass flow rate, specified values of the total pressure and total temperature at the subsonic inlet and the static pressure and temperature at the subsonic outlet give the most stable results. It is noted that both boundaries are defined as an opening allowing the fluid to cross the boundary surface in either direction. Then these boundaries do not block traveling pressure waves in reverse flow direction possibly causing numerical instabilities. At the inlet also a low turbulence intensity is set and it is recommended to set it at the outlet to zero gradient.

In the CFD software package ANSYS CFX the numerical discretization is node based and it uses shape functions to evaluate the derivatives for the pressure gradient term and the diffusion terms in the momentum, continuity and turbulence quantities equations. The Navier-Stokes equations are discretized in an unstaggered, collocated way and solved by an algebraic multigrid solver. To avoid pressure-velocity decoupling, a robust interpolation scheme similar to Rhie-Chow interpolation (1983) [53] is used. CFX solves the conservation equations of mass and momentum in one-system of linear equations, with all equations being fully coupled (ANSYS, 2006) [4]. The turbulence equations are pairwise solved as well.

CFX uses advection schemes such as first-order upwind difference and numerical advection with specified blend factor. This blend factor can be varied between 0 and 1 to vary between a first- and second-order differencing scheme to control numerical diffusion. The high resolution scheme option will be chosen which maintains the blend factor as close as possible to 1 without violating the boundedness principle that could result in non-physical overshoots or undershoots in the solution. Only for the turbulence equations the first-order accurate scheme is sufficient. For CFD simulations for

Test case	Choking	Shocks	Real gas	Separation	Condensation
1D shock tube		X	X		
Axisymmetric nozzle	X	X	X		
2D supersonic ramp		X		X	
2D simplified valve model	X	X		X	
3D pneumatic valve model	X	X		X	
3D safety valve	X	X	X	X	X

Table 3.1. Stepwise validation test cases with focus on combination of physical effects.

unsteady flow a second-order accurate linear multistep method is applied for the time integration of the mass, momentum and energy equation, while a first-order backward Euler scheme is applied for the turbulence equations. As check on the convergence the maximum residual values for mass, momentum and energy and the global balances for momentum and energy equations will be monitored.

3.2 Validation test cases at low pressure

The main performance properties of a safety valve are the mass flow rate and normal flow force exerted on the valve disk. Therefore, it is important to accurately resolve the velocity and pressure fields of the flow especially in the region close to the disk. Since these properties are integrated quantities of the basic flow quantities velocity and pressure, errors in the flow field might cancel, resulting in a good prediction of the mass flow rate and force for already not extremely fine meshes. Hence, the best way to validate a CFD method is with these basic flow fields. When only integral quantities are available, which will be the case in measurements of high-pressure safety valves, the risk of modeling errors can only be minimized by validation with measurement data within the largest operating range as possible.

In the development of the numerical method, benchmark configurations from which field data is available will be used to investigate the relevance of the physical effects and to check whether the real flow is represented adequately. Furthermore, sensitivity and parametric studies of different turbulence models, geometry, initial and boundary conditions will result in a definition of the parameter settings, performance and limitations for a certain range of valve flows. Table 3.1 shows a number of defined test cases and the physical effects to be validated. In the following sections the physical effects will be studied.

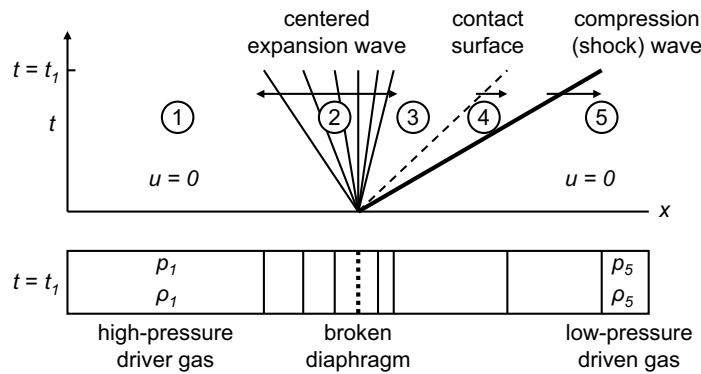


Figure 3.2. Propagation of different waves in an idealized shock tube after diaphragm rupture.

3.2.1 1D shock tube

Sod's well-documented shock tube problem (Sod, 1978) [65] is commonly used to test the accuracy of CFD codes, because it is possible to compare transient gas dynamics, such as expansion waves, contact discontinuities and shocks of an inviscid flow with an analytical solution. A shock tube consists of a pipe in which a diaphragm separates a driver gas at high pressure from a low pressure test gas, which are both at rest. When the diaphragm suddenly bursts, the high-pressure gas expands, i.e. dynamically interacts with the low-pressure side (figure 3.2). Practically, when an object would be placed in the test gas section it can be exposed to a supersonic and high-temperature flow with constant conditions between the shock wave and the contact discontinuity for a few milliseconds so that its aerodynamic behavior typical for aerospace conditions can be tested.

In a duct with small differences in pressure, density and velocity between two locations, compression and expansion waves isentropically balance between the two thermodynamic states. When the differences become larger, the compression wave can topple over, resulting in a discontinuous thermodynamic state change somewhere in the duct. This is the so-called shock wave, where the fluid properties jump through a very sharp gradient. For inviscid flow, the shock is idealized to be infinitely thin. Practically, the shock-front has a typical thickness of the molecular mean free path with strong viscous forces acting on the fluid passing through it, so the process is irreversible. The flow passing a shock is adiabatic, since there is no heat being supplied or work transferred.

For a shock wave Rankine-Hugoniot relations can be derived from inviscid Navier-Stokes equations in combination with a perfect gas between the thermodynamic states before and after the shock as function of the shock strength p_5/p_4 (Hoeijmakers, 2005) [27]. With these jump relations for the velocity u , speed of sound a , pressure p and density ρ five different regions can be distinguished (figure 3.2):

1. undisturbed high-pressure driver gas at rest and constant speed of sound $a_1 =$

- $\sqrt{\frac{\kappa p_1}{\rho_1}}$ with the ratio of the specific heats κ defined in (2.9),
2. simple-wave expansion starting with characteristic $x = -a_1 t$,
 3. uniform flow of the driver gas moving with the contact surface with $x = u_p t$,
 4. uniform flow of the test gas moving with the contact surface until the shock with $x = u_s t$,
 5. undisturbed low-pressure test gas at rest and constant speed of sound $a_5 = \sqrt{\frac{\kappa p_5}{\rho_5}}$.

The contact discontinuity moves with velocity u_p and has to be solved iteratively from

$$\frac{p_1}{p_5} = \frac{1 + \left(\kappa_5 \frac{u_p}{a_5}\right) [X + \sqrt{1 + X^2}]}{\left(1 + \frac{\kappa_1 - 1}{2} \frac{u_p}{a_1}\right)^{\frac{2\kappa_1}{\kappa_1 - 1}}}, \quad (3.18)$$

where

$$X = \frac{\kappa_5 + 1}{4\kappa_5} \left(\kappa_5 \frac{u_p}{a_5}\right). \quad (3.19)$$

The shock speed u_s is given by

$$u_s = a_5 [X + \sqrt{1 + X^2}]. \quad (3.20)$$

It is chosen to evaluate the performance of the CFD software packages ANSYS CFX, ANSYS FLUENT and FEMLAB. The one-dimensional problem is modeled as a square cross-section pipe of length $L = 1$ m that is sliced into a coarse and fine grid with 512 and 10000 respectively equally spaced cells in the x -direction. At the lateral boundaries of the pipe symmetry conditions are applied. A transient simulation is initialized with a sudden pressure drop at $x = 0.5$ m with variable high driver gas pressure p_1 up to 512 bar and constant low driven gas pressure p_5 occurring in safety valve applications, uniform temperature and zero velocity. This sudden pressure drop is expressed as

$$p(x, t_0) = -\frac{p_5 - p_1}{2} \tanh(10^4(x/L - 0.5)) + \frac{p_5 + p_1}{2} \quad (3.21)$$

so that at $0 < x < 0.5$ m p_1 is variable up to 512 bar and from $0.5 < x < 1$ m constant at $p_5 = 1$ bar. Besides the pressure ratio, also the EoS of nitrogen gas is varied. For ANSYS CFX and ANSYS FLUENT the build-in ideal gas and real-gas Redlich-Kwong EoS (section 2.2) are used. For software packages FEMLAB both equations of state are implemented. Besides testing of the capability of resolving the gas dynamics in a shock tube, also the effects of different grid resolution, advection scheme, transient scheme and convergence criterion are studied.

For simulations for both equations of states and driver gas pressure $p_1 = 2$ bar all three packages handle the gas dynamics well and give approximately the same results.

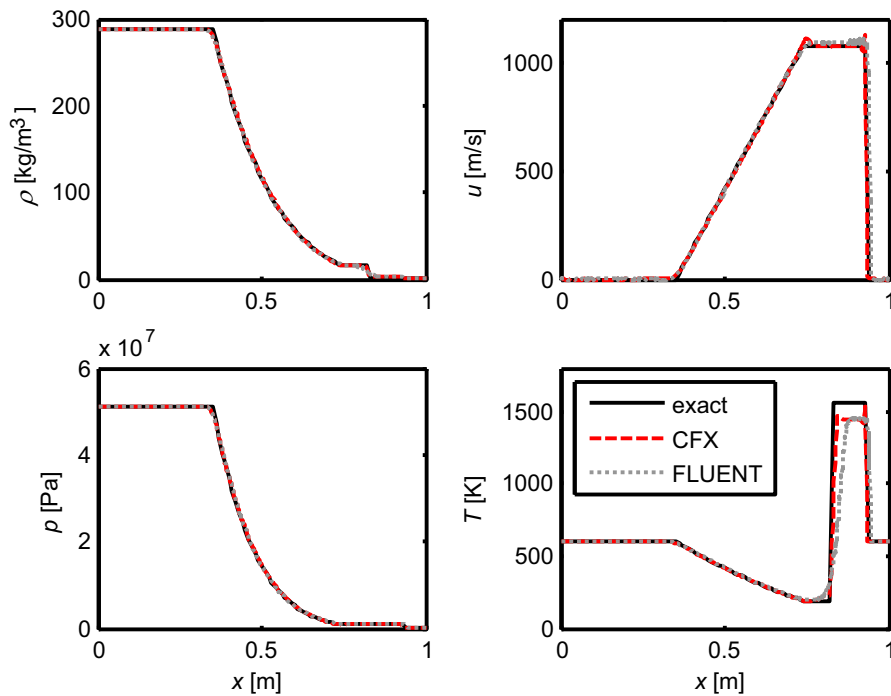


Figure 3.3. Comparison of results of CFX and FLUENT with exact solution for a perfect gas with driver gas pressure $p_1 = 512$ bar, uniform initial temperature 600 K and $t = 3 \times 10^{-4}$ s on coarse grid with 512 cells.

However, at higher driver gas pressures the FEMLAB package fails to converge. The other two packages converge with pressures up to 512 bar with time steps varying between 10^{-5} to 10^{-6} s. The exact solution is only available for a perfect gas and the results of the coarse grid with 512 cells are shown in figure 3.3 after a simulation time of 3×10^{-4} s and time step size of 10^{-6} s.

The performance of both software packages is comparable with only deviations between the analytical and numerical solution in the high-temperature region between the contact surface and the shock wave. These deviations are due to the numerical diffusion of the coarse grid and the inclusion of a turbulence model for the FLUENT case. The simulations have shown that CFX is more stable compared to FLUENT solver this problem with large discontinuities of the solution variables. Simulations with the real-gas EoS are not presented here, but the convergence rates and calculation time are similar to the case of ideal gas simulations resulting in similar behavior of density, velocity, pressure and temperature.

Figure 3.4 presents results from simulations with the fine grid of 10000 cells with a nodal distance of 0.1 mm, which is comparable to the grid size in the bulk flow in a safety valve. The discretization order is varied as well. It can be seen that the results of the simulations on the fine mesh match in the high-temperature region,

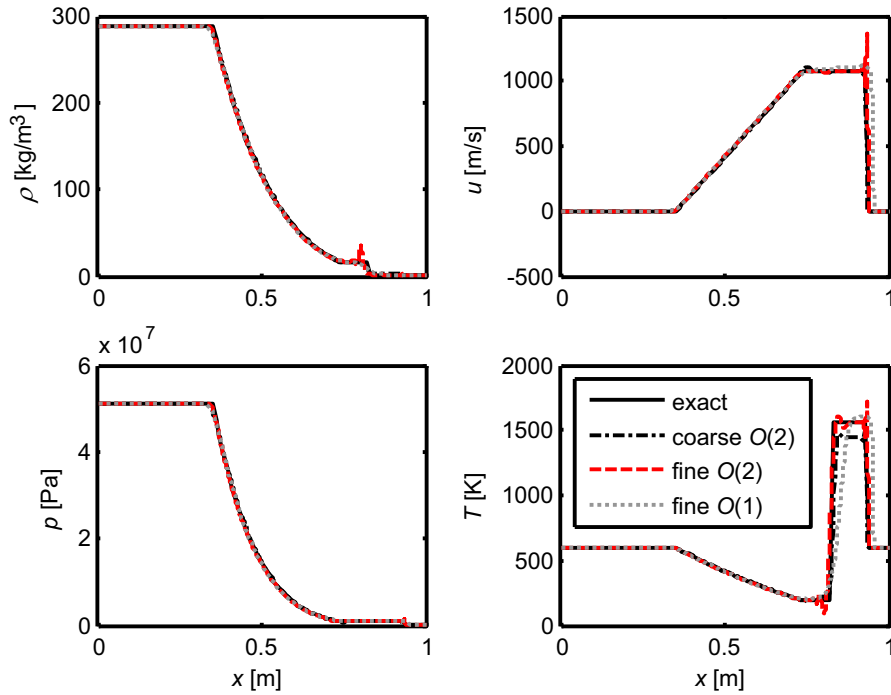


Figure 3.4. Comparison of results of perfect and real-gas simulation in CFX with exact solution for a perfect gas with driver gas pressure $p_1 = 512$ bar, uniform initial temperature 600 K and $t = 3 \times 10^{-4}$ s on coarse (512) and fine (10000) grid.

but the oscillations are unacceptably large for the second-order discretization. In contrast, the first-order solution smears out the temperature discontinuity so that the shock location is poorly predicted. In conclusion, both discretization methods do not provide a satisfactory accurate solution at the shock itself. It is noted that for safety valve flows the flow consists of multiple shocks so that the individual shock strength is at least a factor ten lower as calculated in this test case. Simulations with a driver gas pressure $p_1 = 2$ bar are not shown here, but oscillations were not present so that for weak shocks the solution is sufficiently accurate. Nevertheless, attention should be paid to the existence of oscillations in the flow field of safety valve flows. Also based on general CFD experience it is chosen to develop the numerical method for the safety valve in ANSYS CFX.

3.2.2 Axisymmetric nozzle

With the help of standard DIN EN ISO 9300 [28] it is possible to determine gas mass flow rates by means of fixed nozzle geometries with an accuracy of 0.3%. The standard uses an experimentally determined critical flow function C^* to correct for the deviations between the ideal nozzle theory and experimental data. This correction

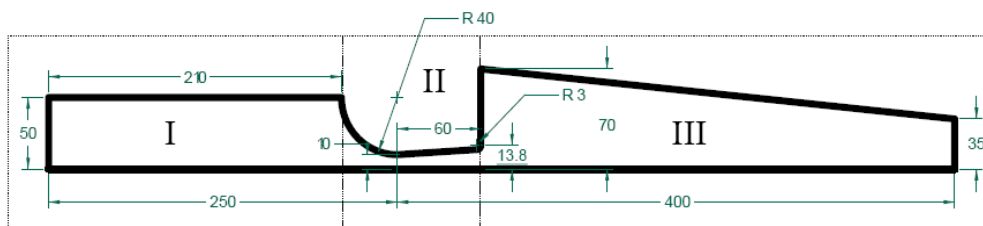


Figure 3.5. Front section of axisymmetric nozzle.

factor is tabulated for common gases for temperatures from 200 to 600 K and pressures from 1 to 200 bar. The mass flow rate is calculated with

$$\dot{m} = \frac{A_0 C_{d'} C^* p_0}{\sqrt{\frac{R}{M} T_0}} \quad (3.22)$$

with the flow coefficient $C_{d'}$ depending on the Reynolds number as

$$C_{d'} = a - b Re_0^n \quad (3.23)$$

with tabulated coefficients a , b and n . In ANSYS CFX11 the mass flow rate of an axisymmetric nozzle geometry (part II in Fig. 3.5) 2° rotated around its axis with a nozzle throat diameter $d_0 = 20$ mm is calculated. Symmetry planes are applied to the azimuthal boundaries of the sector. The solver of ANSYS CFX does not support 2D planar or axisymmetric computational domains, so that these have to be converted to a plane or sector with single cell thickness in the tangential direction. As long as the rotation angle is a few degrees the accuracy of the numerical solution is hardly affected. Part I is an enlarged inlet to apply a total pressure condition of the flow at rest and part III is enlarged as well to stabilize the flow at the static pressure outlet. At the nozzle throat the nodal distance of the quadrilateral unstructured mesh elements was 1 mm with a first layer thickness of 0.2 mm at the smooth walls to get 18 nodes along the nozzle radius.

The walls are assumed adiabatic and also at the axis symmetry boundary conditions are applied. The flow is solved with the total energy equation including the term for viscous work at the walls and with the SST turbulence model. The fluid considered is nitrogen with its properties according to the real-gas EoS (section 2.2). This flow is assumed to be steady. The close to second-order accurate advection scheme is employed. Table 3.2 shows a comparison between the results of the numerical method and the experimentally determined values of the critical nozzle for various inlet pressures. The total density at the inlet is compared with database GERG (2004) [37] with an uncertainty of less than 0.1%.

From 100 bar onwards the density deviates up to 5.65% at 200 bar, for which real-gas effects become apparent. It can be concluded that, although the Redlich-Kwong EoS used has insufficient accuracy for these inlet pressures, the mass flow rate calculated with the CFD program remains accurate with deviations smaller than 0.46%.

p_0 [bar]	C^* [-]	\dot{m}_{CFX} [kg/s]	\dot{m}_{dev} [%]	$\rho_{0,CFX}$ [kg/m ³]	ρ_{dev} [%]
2	0.68492	0.143863	0.33	2.2474	0.02
25	0.69182	1.81545	-0.03	28.254	0.32
100	0.70703	7.42794	0.46	112.935	1.08
150	0.71555	11.278	0.04	168.413	2.23
200	0.72168	15.1973	0.21	224.539	5.65

Table 3.2. Comparison of mass flow rates and densities at the inlet of an ISO 9300 axisymmetric nozzle as a function of inlet pressure at constant inlet temperature of 300 K and constant static pressure of 1 bar at the outlet.

The reason is that this quasi one-dimensional flow is essentially irrotational resulting in a low dependency of the density on the position of the sonic flow plane that limits the mass flow rate at the nozzle throat. With the developed real-gas property tables described in section 2.3, the error in the density reduces to values below 2%.

3.2.3 2D supersonic ramp

In a safety valve, the interaction between the transonic flow below the valve disk and the disk itself determines its opening characteristics. The supersonic flow over a bump, see NASA (Settles, 1991) [60], is used to study the numerical accuracy of the numerical method ANSYS CFX11. The geometry concerns a 2D compression corner of 25° and height $h = 15$ mm, where the horizontal x -coordinate has its origin at the compression corner and follow the ramp whether horizontal or sloped. The y -coordinates has its origin at the model surface.

Static pressures and Mach numbers calculated from mean velocity profiles are used for comparison. The locations are adjacent to the surface of the ramp geometry and at five sections at constant x -coordinate, see figure 3.6. The mean flow profiles obtained from Pitot measurements are at maximum 30% inaccurate in the vicinity of shocks. The experiment with free-stream conditions of the air in the wind tunnel were: Mach number $Ma = 2.88 \pm 0.003$, temperature $T = 294 \pm 12$ K and pressure $p = 0.12 \pm 0.001$ bar.

In ICEM CFD, a 2D geometry around the wedge with $40h$ long and $13.33h$ high is discretized using structured mesh with a minimal nodal wall distance of 0.5 mm from $2h$ before to $1h$ after the ramp for the coarsest grid. The nodal distance increases towards the inlet at the left with a ratio of 1.025 and to the outlet at the right with a ratio of 1.2. The first cell thickness on the adiabatic walls at the bottom is 0.01 mm with an expansion ratio of 1.1 to the free-slip wall at the top. The 2D mesh with one cell in the z -direction consists of 33588 hexahedral cells. Also grids with a nodal distance of 0.25 and 0.125 mm have been tested.

In ANSYS CFX11, symmetry conditions are applied to the front and back plane. The fluid model is air ideal gas with constant properties. The turbulence model is the SST model of Menter [42]. The expected dimensionless wall-normal coordinate y^+ values at the ramp are around 2. The inlet of the steady-flow simulations is supersonic with a prescribed velocity $u = 990$ m/s corresponding to the Mach number of 2.88

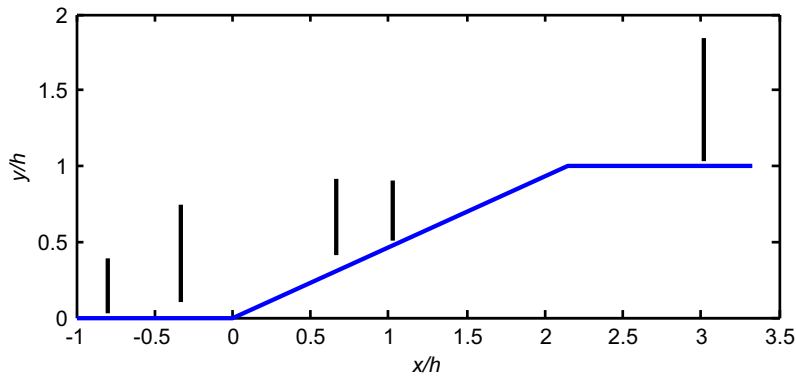


Figure 3.6. Ramp geometry with five measurement sections.

and the static pressure of 0.12 bar. The outlet is supersonic as well. With these basic settings the performance of the two-equation turbulence models $k - \epsilon$ and SST with transitional turbulence as well as the Reynolds stress turbulence model LRR are varied. In the LRR model the six components of the Reynolds stress tensor and the turbulent kinetic energy are solved from seven transport equations instead of the eddy viscosity models $k - \epsilon$ and SST that use two equations. Furthermore, the mesh density and the discretization order are varied to study their influences on the overall solution accuracy. Figure 3.7 shows the pressure distribution on the ramp and Mach number distribution at 0.1 mm and 1 mm above the ramp. The pressure and Mach number distributions perpendicular to the wall of the first two sections show the largest sensitivities to the applied turbulence model. These results are presented in figure 3.8.

The results of the first-order discretization of the SST model are significantly closer to the experimental values than the results of the second-order discretization of the SST turbulence model as well as the second-order LRR model. However, simulations with the finer grid approach the second-order SST solution and this grid, the solution has become insensitive to the discretization order. Also further away from the wall, the SST model at first-order represents the bulk flow better than the other two turbulence models. None of the turbulence models investigated correctly predict both the separation and reattachment point. Alternatively, numerical simulations with the transition turbulence model of SST accurately predict these locations, but the predictions of the bulk flow is worse than the standard SST model itself.

In the comparisons of the measurement sections $x/h = -0.8$ and -0.33 it is shown again that the first-order SST model gives the best results. It is not possible to obtain converged solutions with the $k - \epsilon$ and $k - \omega$ model for this type of flow. Also the time-averaged values of unsteady flow simulations with the SST model give the same results as steady flow simulations. When the valve disk of a safety valve is shaped like a wedge-expansion corner with recirculating flow, it is important to resolve the separation and reattachment points for accurate prediction of the pressure distribution and the resulting flow force. In such a case, use of the SST model with transitional

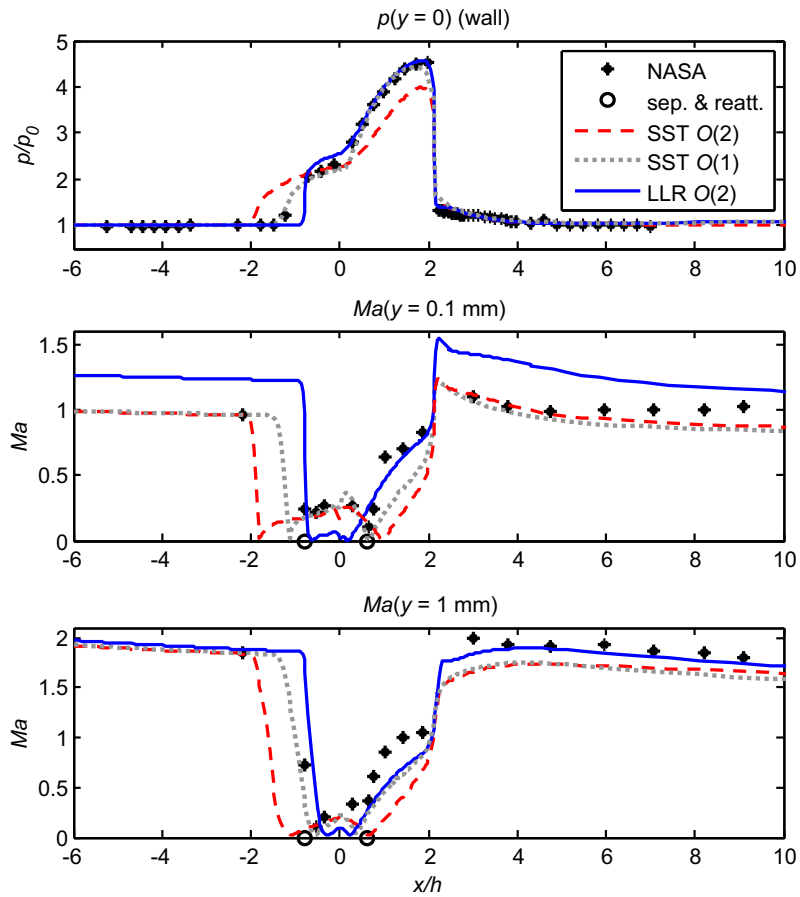


Figure 3.7. Pressure and Mach number distributions as a function of the x -coordinate on and adjacent to the wall with different RANS turbulence models and order of spatial discretization for coarsest grid.

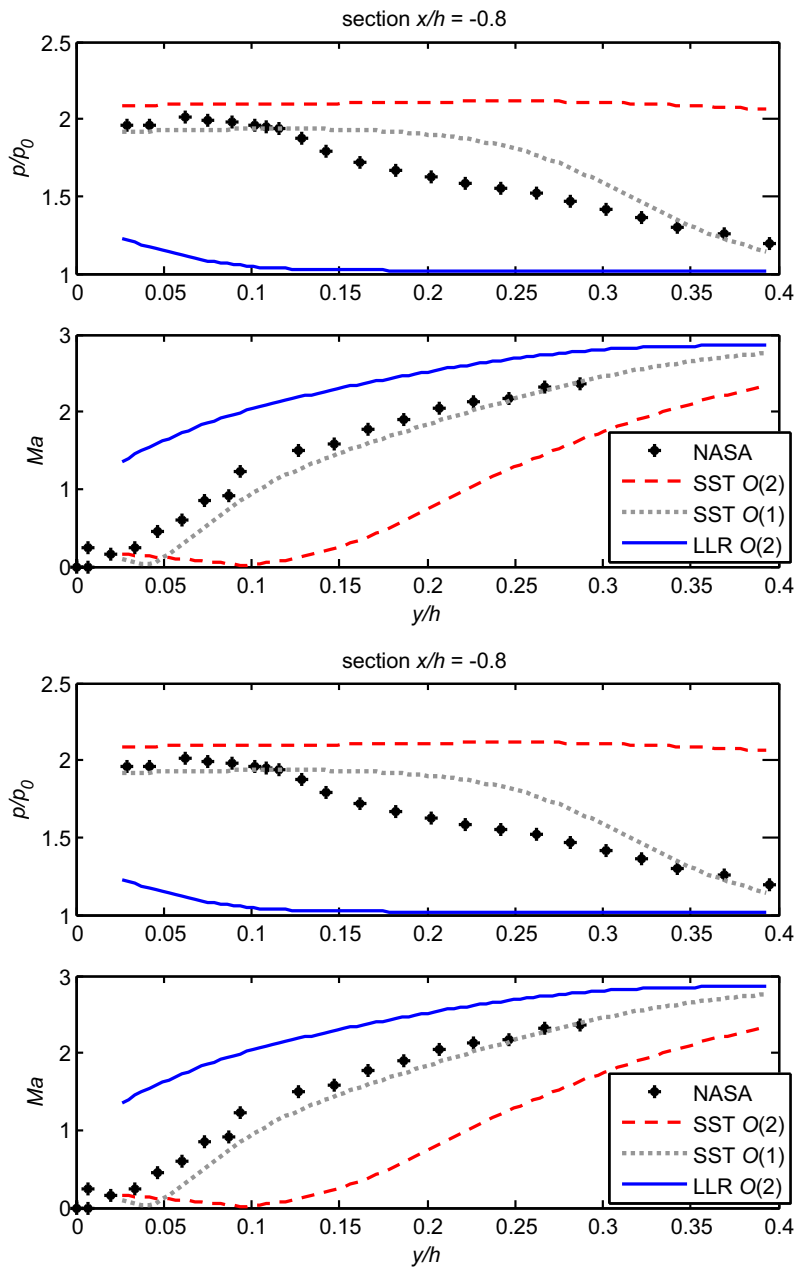


Figure 3.8. Pressure and Mach number distributions of first two sections with different RANS turbulence models and order of spatial discretization for coarsest grid.

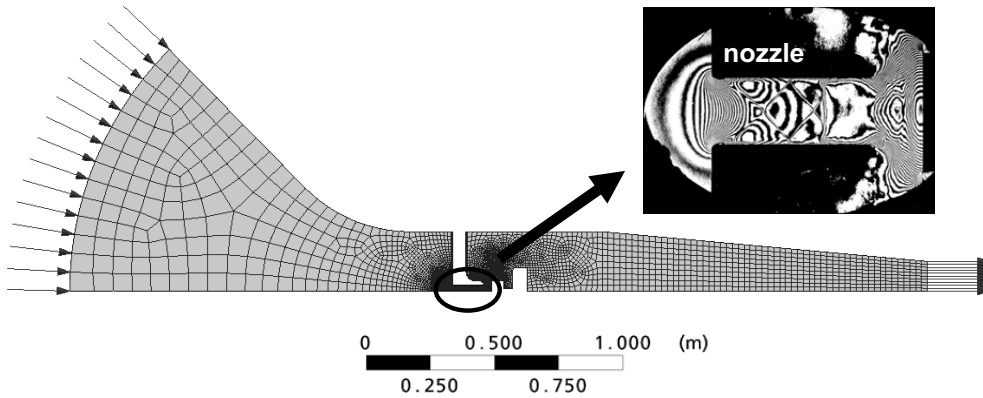


Figure 3.9. Computational domain representing upper part of vacuum channel. Insert shows window of valve model with Mach-Zehnder-Interferometry photograph.

turbulence would be preferable. On the other hand, the bulk flow determines the mass flow rate and should therefore be accurately predicted as well. Only a turbulence model sensitivity study can show the size and location of areas with recirculating flow. From these results, the optimal grid size in combination with the SST model can be chosen.

3.2.4 2D simplified valve model

Föllmer used a simplified 2D safety valve model in a vacuum channel to visualize density changes of choked dried air flow with Mach-Zehnder-Interferometry (Föllmer, 1981) [22]. From this photographed window with density fringes and the known fixed density increments ($d\rho = 0.034 \text{ kg/m}^3$) between two fringes, the density field can be reconstructed. Without flow the optical misalignment of the interferometer is reduced to a half fringe shift over the total optical area, so that the absolute density uncertainty is less than 0.017 kg/m^3 . In the work of Föllmer an experiment is selected, in which separation and reattachment areas of the flow interact with the position of shocks and their reflections.

In the right part of figure 3.9 the selected picture of the valve experiment with throat diameter $d_0 = 40 \text{ mm}$, fixed valve disk lift ratio $h/d_0 = 0.7$, inlet pressure 1 bar, outlet pressure 0.25 bar and inlet temperature of 293 K is shown. The photographed window with the valve model is the ellipse in the domain shown. The valve is placed in a duct with $10d_0$ height. In the computational domain only the upper half is considered, assuming symmetry. The inlet and outlet geometry is according to the experimental setup truncated far enough from the flow restriction to ensure a definition of the boundary conditions insensitive to the flow.

The hexahedral grid domain is one cell thick with symmetry planes on both sides. It is important to resolve the boundary layer with a well-defined grid. A grid refinement study shows that the dimensionless distance of the first grid line to the wall

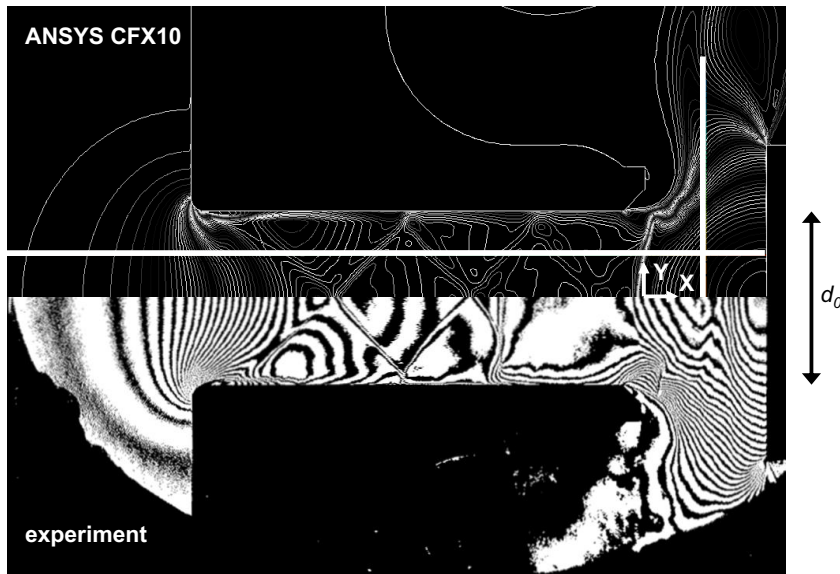


Figure 3.10. Density contour plot with two lines $y = d_0/4$ and $x = 0.35d_0$ along which local densities are compared in figure 3.11. The finest mesh with nodal spacing of 0.5 mm is used resulting in 18 nodes at the chamfered edge of the valve seat with diameter d_0 .

can be large since the separation of the flow is induced by sharp edges with large pressure gradients. Therefore, the first layer thickness is 0.2 mm corresponding to a dimensionless wall distance of $y^+ = 100$ with an inflation factor of 1.2 to the bulk grid density. In the nozzle throat the nodal spacing is varied from 0.5 to 4 mm. The EoS used is a thermally perfect gas with heat capacity depending on temperature. The simulations are carried out with ANSYS CFX10 with the same flow equations as in the critical ISO nozzle test case in section 3.2.2.

The upper part of figure 3.10 shows density contour lines resulting from the numerical simulations on the finest grid and the lower part shows the corresponding Mach-Zehnder photograph. Along the horizontal straight line at $y = d_0/4$ parallel to the nozzle axis and along a line in the middle between the nozzle tip and the disk, parallel to the disk, at $x = 0.35d_0$ the density variations are compared. The results from the reconstructed density contours from the experiment and the simulations with the finest and coarsest mesh and with two two-equation RANS turbulence models SST and $k-\epsilon$ are shown in figure 3.11. The origin is located in the middle of the nozzle throat with $L/d_0 = 0$.

In general, the locations of the shock reflections and the shock front at the nozzle axis show excellent agreement with the experimental data. Both the coarsest grid and the finest grid represent the global result of the experiment well. Especially in the part before the nozzle, the deviation from the experiment is within the experimental accuracy, which is half the fringe width.

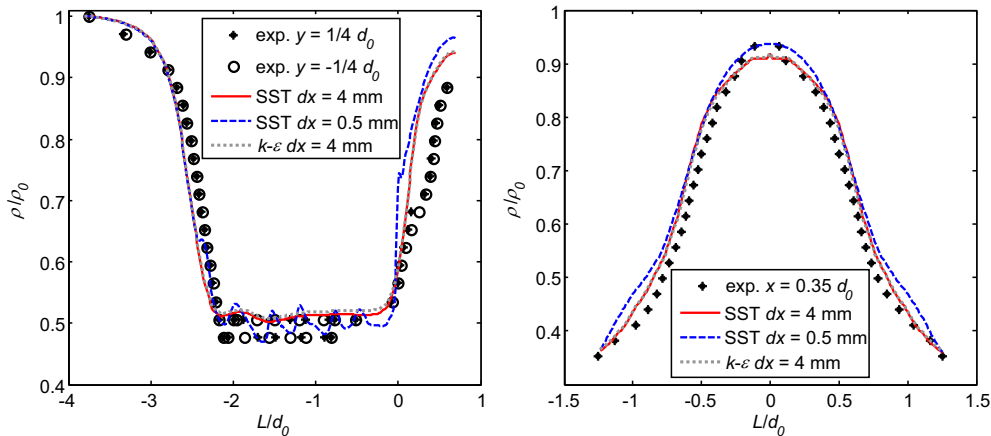


Figure 3.11. Comparison of density lines at $y = d_0/4$ from the nozzle axis and parallel to the disk at $x = 0.35d_0$ with $y^+ = 100$.

Deviations occur in the nozzle itself, because only the finest grid resolves the photographed density oscillations. A sensitivity study shows that the numerical solution is neither sensitive to the wall function formulation nor to the turbulence model chosen. However, only the SST model is stable for finer grids and therefore, the $k - \epsilon$ model cannot properly resolve the shocks. Furthermore, only the finest grid resolves the shock reflections well.

Between the nozzle and the disk, deviations become significant, because the numerical solution shows a stronger bow shock around the origin than the experiment, where the shock is smeared out over a larger area. In this area, again, only the finest grid represents a density discontinuity halfway along the pressure recovery path, but at a different location. It might be that this secondary shock front is a transient flow effect and therefore not seen in the CFX calculations for steady flow or that the SST model dissipates this discontinuity.

3.2.5 3D pneumatic valve model

Since accurate validation data of valve geometries is limited, another validation test case concerning volumetric air flow rates of a pneumatic model valve from Bürk (2006) [14] is defined (figure 3.12). In this work, steady air flow rates in rotationally symmetric blunt body geometries as well as in pneumatic valves with a side outlet with set pressures up to 7 bar were measured with an orifice in accordance to standard DIN 1952 (1982) [19]. This test case focuses on the pneumatic valve, where the disk lift h is varied up to $3/4$ times the seat diameter d_0 of 22 mm. In this work the flow was calculated with a comparable CFD method with deviations from the experimental data within 6.5%. The pressure ratio p_b/p_0 is kept constant at $3/7$, which is smaller than the critical pressure ratio for ideal air flow of 0.53 indicating that in this 3D geometry supersonic flow areas occur. The pneumatic model valve geometry is close to

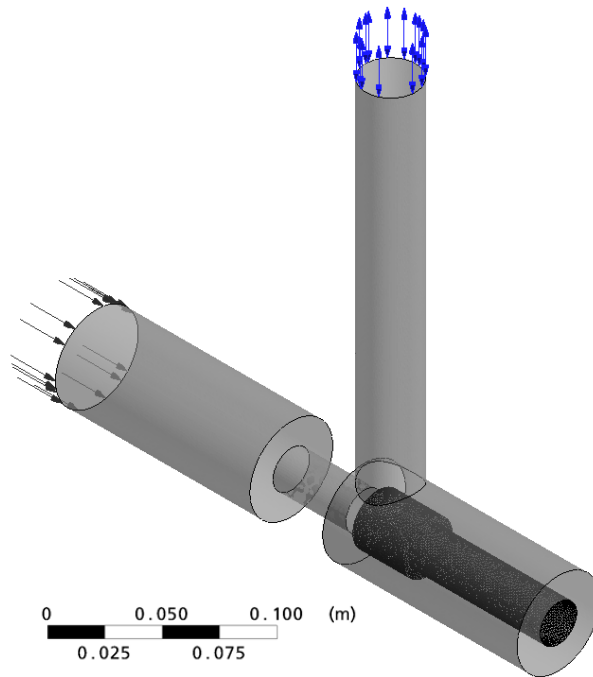


Figure 3.12. Computational domain of 3D pneumatic valve model with highlighted flapper.

a safety valve geometry except the inlet length, which is only $2D$ long with a sudden contraction, instead of over $10D$ with a conical contraction. Therefore, it is likely that flow separation at the edge of the sudden contraction plays a more important role for the pneumatic model valve. As a consequence, after flow separation at the sudden contraction, the flow will not reattach before the seat and a recirculation area remains. Also the outlet of the pneumatic valve is small, so that the choking plane at high disk lifts and low pressure ratios will not exist between the valve seat and the flat disk, but at the outlet.

The computational domain is divided into 1.2 million tetrahedral cells with structured boundary layer cells. Also a second computational domain is created for axisymmetric simulations similar to validation test case nozzle DIN EN ISO 9300 described in section 3.2.2. Simulations for steady flow to compute the normalized volumetric flow rate \dot{V}_N of air are carried out at different valve lifts with constant inlet pressure of 7 bar, outlet pressure 3 bar and 20°C (see figure 3.13). The present numerical simulations show that the numerical 3D model reproduces the measured normalized volume flow rates within 5%. At the smallest and highest disk lifts 3D effects of the flow at the inlet play a less dominant role, because the deviations of the axisymmetric simulations become smaller. The deviation of the normalized volumetric flow rate $\dot{V}_{N,dev}$ is largest when the geometric cross-section of the valve seat $\pi d_0^2/4$ and the area between the seat and the disk $\pi d_0 h$ are equal when $4h/d_0 = 1$. The overprediction

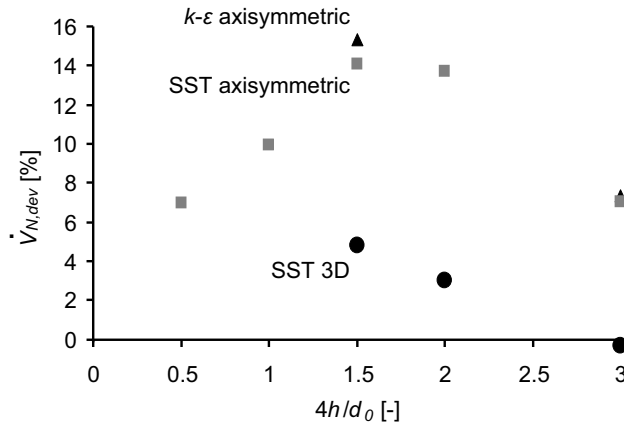


Figure 3.13. Deviations between computed and measured normalized volumetric flow rates with respect to disk lift of 3D pneumatic valve model at pressure ratio 3/7 with different RANS turbulence models and computational domains.

of the flow capacity at this point is due to a too low calculated pressure loss of the shock at the contraction resulting in a 5% too high stagnation pressure at the front of the disk (Bürk, 2006) [14]. Nevertheless, the local pressure errors partly compensate each other in the contribution to the total flow force on the disk.

3.2.6 3D safety valve

High-pressure safety valve capacity tests carried out at by TÜV Rheinland Aachen (1988) [68] are used as reference data for comparison with results of numerical simulations. Two safety valves with nominal sizes 6 and 10 mm are chosen. These valves have an exchangeable seat with diameter $d_0 = 4$ and 8 mm, respectively and valve spindles with the shape of a truncated cone without lifting-aid. The mass flow rate was measured with fixed disk lifts h without installed spring with 2.5% accuracy. The inlet pressure of the air flow was kept constant at 7 bar, outlet pressure 1 bar and inlet temperature 20 °C.

The computational domain consists of a 3D valve comparable to the construction drawing (figure 3.14 left) which is cut in half at the symmetry plane. The inlet is enlarged to get a well-defined total pressure condition with $Ma < 0.01$ for fast convergence. The first cell thickness of the structured boundary layer grid is 0.01 mm and the nodal distance 0.02 mm increasing with an expansion factor of 1.02 up to 1 mm from the smallest flow cross-section. Figure 3.14 right shows the axisymmetric geometry derived from the 3D model. The simulations of the safety valve with nominal size 6 mm are carried out for both the axisymmetric and 3D geometry, but simulations with nominal size 10 mm are carried out for only the axisymmetric geometry. The results of the simulations are compared with the experimental data in figure 3.15. The discharge coefficient K_d is derived from the mass flow rate with the ideal gas

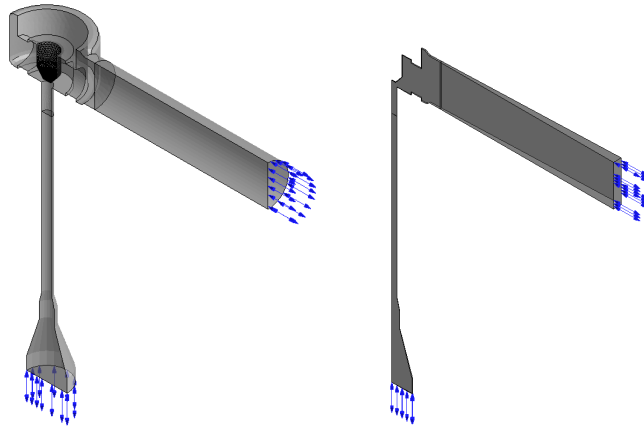


Figure 3.14. 3D and axisymmetric computational domains of safety valve 6 mm with highlighted disk.

properties of air $\kappa = 1.4$ and $Z = 1$ according to equations (2.2-2.10). At higher fixed dimensionless disk lifts h/d_0 the discharge coefficient K_d is up to 18% overpredicted. To investigate the error source of this large deviation, the results of a numerical parameter sensitivity S study are given in table 3.3. This study is subdivided into geometry parameters, discretization parameters, turbulence model parameters and fluid flow parameter parameters.

To start with the geometry parameters, the sonic flow plane limits the mass flow rate in a safety valve, which is located in the axisymmetric part between the valve seat and the valve spindle. The influence of 3D effects is smaller than 1% as expected. In addition, when the edge of the truncated valve cone and the sharp edge of the seat is rounded with a relatively large fillet radius of 0.1 mm the increase in the mass flow rate is 6.5%. This increases the deviation between the numerical result and the reference data point even more.

Second, the discretization influence is studied by comparing the solution of a coarse mesh with that of a fine mesh with a four times smaller nodal distance resulting in a throughput decrease of 2%. Furthermore, using a structured mesh instead of an unstructured mesh results in an increase of 4%. Finally, the mesh is automatically adapted to be three times refined in regions where the pressure gradients are large resulting in a mass flow rate reduction of 3%.

Third, the variation of alternative RANS turbulence models, such as $k - \epsilon$ with a production limiter, the LRR Reynolds stress model, or the SST model with transitional turbulence leads to a mass flow rate deviation up to 4%. Also a larger distance of the first grid point from the wall or the inclusion of rough wall treatment do not significantly affect the throughput with a reduction up to 0.7%.

Fourth, the inclusion of an equilibrium phase change model with the wet Redlich-Kwong EoS shows that homogeneous condensation can first occur at an inlet pressure of 10 bar onwards, because then the local temperature in the supersonic area drops

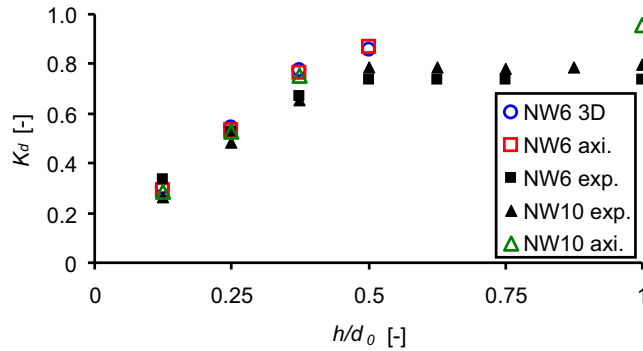


Figure 3.15. Comparison of discharge coefficients of normal high-pressure safety valves with nominal inlet diameter 6 and 10 mm with numerical simulations for different values of the disk lift, pressure ratio 1/7 and a calorically perfect gas.

Sensitivity parameter	S [%]
Axisymmetric vs. 3D valve domains	1
Production tolerances of seat diameter and misaligned seal lenses	6.5
Discretization uncertainty after three times grid refinement	2
Structured grid based on coarsest reference grid	4
Mesh adaptation in three steps based on coarsest grid	-3
Alternative RANS turbulence model $k - \epsilon$ with production limiter	4
Alternative RANS turbulence model LRR Reynolds stress model	0.4
Transitional turbulence of SST turbulence model	-0.8
Near-wall treatment of turbulence model with $y^+ = 35$ up to $y^+ = 3500$	-0.5
Rough walls with arithmetic average of roughness $Ra = 10 \mu\text{m}$	-0.7
Equilibrium phase change with wet Redlich-Kwong EoS	0
Swirl 45° at the inlet	0

Table 3.3. Sensitivity study of numerical parameters in high-pressure safety valve model.

below the thermodynamic critical point of the gas. The inlet pressure of 7 bar is not high enough to let nitrogen condense in the supersonic flow region. Also, a tangential velocity equal to the axial velocity at the inlet generates a swirl of 45° , but since no driving force is present it disappears with accelerating flow so that this fluid flow parameter does not affect the mass flow rate either.

Only an arithmetic average of the roughness profile of $Ra = 100 \mu\text{m}$ would lead to a reduced gas mass flow rate of 16.5% but this value is not realistic since the construction drawing allows only $Ra = 3.2 \mu\text{m}$ at maximum. That means that neither of the investigated numerical modeling parameters compensate for the large deviation at higher disk lifts at most. In section 5.2.1, the valve capacity measurement of TÜV Rheinland Aachen (1988) [68] with safety valve 10 mm with exchangeable seat and valve spindle without lifting-aid at the largest fixed disk lift of $h/d_0 = 1$ will be replicated.

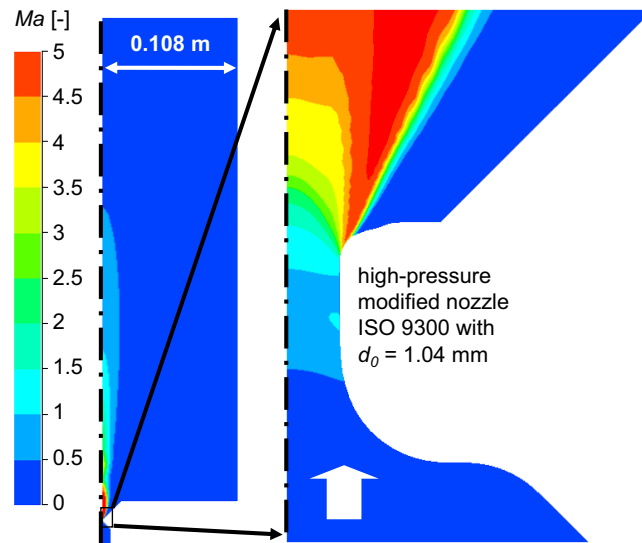


Figure 3.16. Mach number contour plot in axisymmetric computational domain computed with ANSYS CFX with focus on smallest cross-section of high-pressure nozzle experiment 3500 bar inlet pressure.

3.3 Validation test case of a high-pressure nozzle

Experimental data concerning mass flow rate experiments of a high-pressure nozzle with gaseous nitrogen up to 3500 bar is available (Netter, 2005) [48]. In these experiments performed at the ultra-high pressure laboratory of BASF a low-pressure nozzle located downstream of the high-pressure nozzle with throat diameter 1.04 mm was used as a reference device. Both nozzles were constructed according to standard ISO 9300 as much as possible. Depending on the pressure upstream of the low-pressure nozzle, blowing-off into the atmosphere, the throughput of the critical flow was calculated according to ISO 9300 [28] or the flow was considered sub-critical and was determined according to ISO 5167 [29]. In both standards, the dimensionless flow coefficient C is deduced from several experimental data in order to get errors below 1%.

In an experiment, a pressurized vessel with nitrogen attached to the nozzles was relieved through the nozzles into the atmosphere. Four experimental series were carried out with initial pressures in the vessel ranging from 100 to 3500 bar. In the experiments with relieve pressures higher than 1000 bar a satisfactory steady flow between the high-pressure and low-pressure nozzle could not be established anymore, so that the uncertainty of these mass flow rates is in the order of 5%.

With the help of the CFD tool ANSYS CFX, the high-pressure nozzle experiments have been numerically simulated as well. Therefore, the geometry of the high-pressure nozzle with throat diameter 1.04 mm is measured with a coordinate machine with an

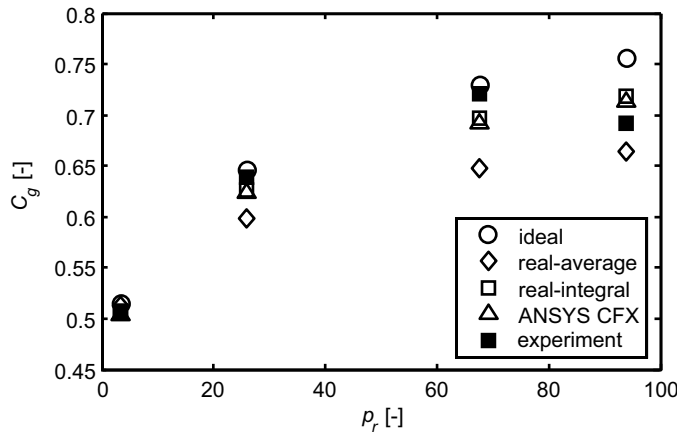


Figure 3.17. Comparison of three valve sizing methods and numerical model with experimental data of a nozzle at inlet pressures up to 3500 bar.

accuracy of $0.9 \mu\text{m}$. Figure 3.16 shows the results of a numerical simulation of the nozzle experiment with initial pressure of 3500 bar in the vessel. The left part shows the Mach number contours projected on the whole axisymmetric computational domain of the nozzle. The right part focuses on the geometrically smallest flow cross-section of this domain with the actual nozzle in accordance with ISO 9300. The smallest nodal distance in the nozzle throat is $40 \mu\text{m}$ with an inflation ratio of 1.05 to achieve 27 cells in radial direction. The first cell thickness of the boundary layer with 20 cells is $1 \mu\text{m}$ to obtain a dimensionless wall distance $y^+ = 900$ at a pressure of 3000 bar. The thermodynamic properties of nitrogen are defined in the real-gas tables which are equal to the properties used for the valve sizing models as described in sections 2.2 and 2.3.

Due to a developed thin boundary layer the flow is already completely choked before the geometrically smallest cross-section at the nozzle throat. Downwards of the nozzle throat the flow expands further to Mach number 5. Since the real-gas tables are fully thermodynamically consistent the maximum residues of the solutions reduced to below 10^{-5} with only local higher residues in the jet shear layer downstream of the nozzle.

In figure 3.17 the results of the CFD method are compared with the four nozzle experiment series. Also the results of the three valve sizing methods that are already compared with each other in section 2.7 can be compared with the experimental data since this is an experiment of a nozzle flow. The CFD results agree well with experiment within its accuracy. Furthermore, the *real-integral* method delivers a slightly lower flow coefficient than the computational model. This deviation is actually the velocity coefficient φ correcting for friction losses which is 0.994 on average. The results of the other two analytical methods deviate from the numerical solutions in the same way as figure 2.6.

Chapter 4

Facility for safety valve tests

This chapter summarizes the high-pressure test facility to conduct function tests of high-pressure safety valves at operating pressures up to 600 bar to provide measurement data for validation of the numerical method. In section 4.1, design considerations and the construction of the test facility are provided. Then in section 4.2, the apparatus for the quantities to be measured are presented. Lastly in section 4.3, in two example tests is demonstrated how the valve capacity and opening characteristic of a safety valve operating with sub-cooled water and gaseous nitrogen are determined.

4.1 Design considerations and construction

For validation of the numerical method, valve tests are conducted at well-defined measurement conditions for various fluids, pressures, valve types, valve sizes and springs. A test facility is constructed to determine the discharge capacity and opening characteristics of high-pressure safety valves for water and nitrogen at operating pressures up to 600 bar. Also special measurement equipment is designed and calibrated to measure local values of pressure and temperature, valve disk lift and the integrated quantities mass flow rate and force on the valve disk. In the test facility the major valve characteristics described in the standard EN ISO 4126 [30] are tested. The valve tests are carried out for the following operating conditions for maximum pressure relief:

- The valve is installed on a vessel with a minimum pipe length so that the risk of valve disk vibrations, caused by moving pressure waves or excessive pressure losses at the inlet during valve opening, is minimized.
- The pressure losses in the piping around the valve are small compared to the pressure loss in the valve.
- The vessel is large to have well-defined conditions for accurate measurement of the total pressure and temperature and so the mass flow rate.

- The valves are experimentally investigated with mounted protection cap on the spring housing so that an elevated pressure in the spring housing can build up to act as counter-pressure assisting to close the valve.

The operating characteristics are determined by measurement of:

- total temperature at the valve inlet,
- total pressure at the valve inlet,
- valve disk lift,
- mass flow rate through the safety valve,
- force on the valve disk.

No local temperatures and pressures in the bulk flow are measured, since it is difficult to implement sensors in a high-pressure test rig without disturbing the flow.

All sensors are located at different positions around the test valve and have different response times. As a consequence, for accurate valve characterization, the flow conditions at the test valve inlet have to be constant as long as the slowest sensor response during blow-off to avoid effects of finite response time of the measurement equipment. The application of a second storage vessel connected by a control valve to the buffer vessel on which the safety valve is mounted allows constant operating conditions in the following way. Prior to a valve test the storage vessel is pressurized with compressed nitrogen at a higher pressure than the operating pressure of the test valve. During the test the control valve adjusts the flow rate from the storage vessel to the buffer vessel in order to keep the pressure in the buffer vessel constant during blow-off of the test valve, while the pressure in the storage vessel decreases. The buffer vessel is sufficiently large to damp fast pressure changes caused by sudden opening of the control valve or the test valve.

The test rig consists of four vessels (see figure 4.1). Vessel B1 is connected to the compressor, which provides a pressure up to 4000 bar. Safety valve SV1 protects vessel B1 and safety valve SV2 ensures a safe pressure reduction to 600 bar in the test facility itself. After the shut-off valve V2 the high-pressure pipe changes from a maximum allowable operating pressure of 3600 bar (PN3600) to piping with a nominal pressure PN700 and nominal diameter 24 mm (NW24) connected to the vessels B2, B3 and B4. Either buffer vessel B3 is in use for valve tests with water or buffer vessel B2 for valve tests with nitrogen. In figure 4.1 the connected parts of the test facility to the buffer vessels that are partly in use for valve tests with either nitrogen or with water are grey colored. During a valve test, high-pressure nitrogen in the storage vessel B4 expands into buffer vessel B3 filled with water or buffer vessel B2 filled with nitrogen and actually pushes the test fluid in the buffer vessel through the valve located at the opposite side of the feed lines of one of the buffer vessels.

Vessel B3 is tilted 1 m at the side with the water feed valve V7 at the lower inlet and air vent or nitrogen release valve V8 at the higher inlet to increase the maximum filling level of water to 90%. The remaining 10% can be compressed with nitrogen from storage vessel B4. Nitrogen release valve V4 is used to relax buffer vessel B2

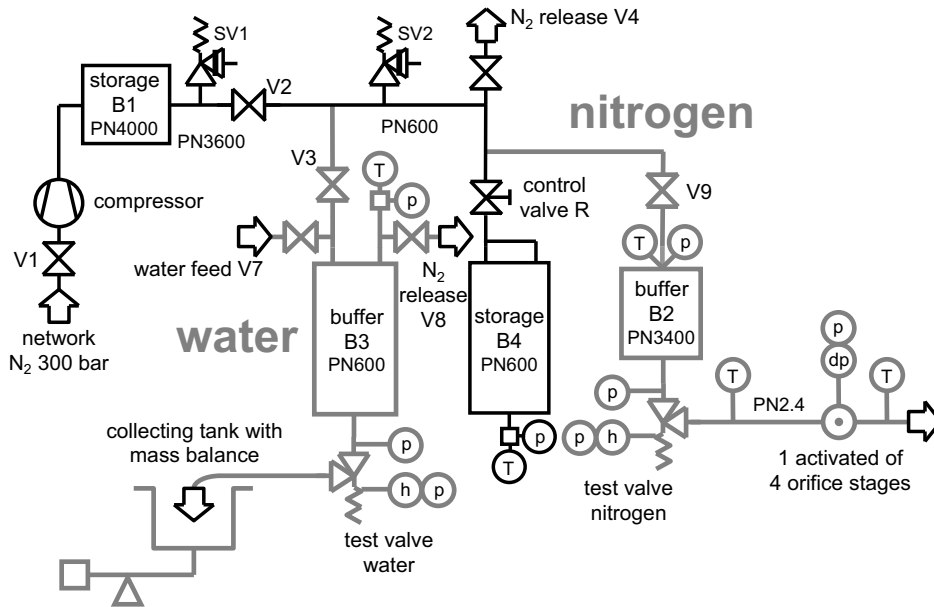


Figure 4.1. High-pressure valve test facility.

after a valve test with nitrogen. Details of the gas mass flow measurement system with 4 orifice stages are given in section 4.2.6 and for the water liquid mass flow measurement system with collecting tank on a scale are given in section 4.2.5. Figure 4.2 shows a picture of the test facility at BASF site Ludwigshafen.

A control valve R PN700 NW24 with pneumatic diaphragm actuator and return springs is located between the storage vessel and the two buffer vessels. With a digital controller ABB Protronic 100 two linear PI-control loops are programmed to define a pressure increase before the test valve opens in the first loop and to keep the pressure at a constant level while the test valve is open in the second loop.

4.2 Measurement variables

Table 4.1 summarizes the measured quantities in the valve test facility. The disk lift and force sensor are mounted in the spring housing of the safety valve to be tested either with water or with nitrogen. The same accounts for a pressure transducer just before the safety valve and one in the spring housing with protection cap of the safety valve. Depending on the actual operating pressure of the test rig the pressure sensors with the corresponding measurement ranges are mounted in the vessels. This also applies for the two pressure sensors around the safety valve. In the gas mass flow measurement only one of the four orifice stages is activated, where the differential and absolute pressure sensor and the temperature sensor is mounted. In the next

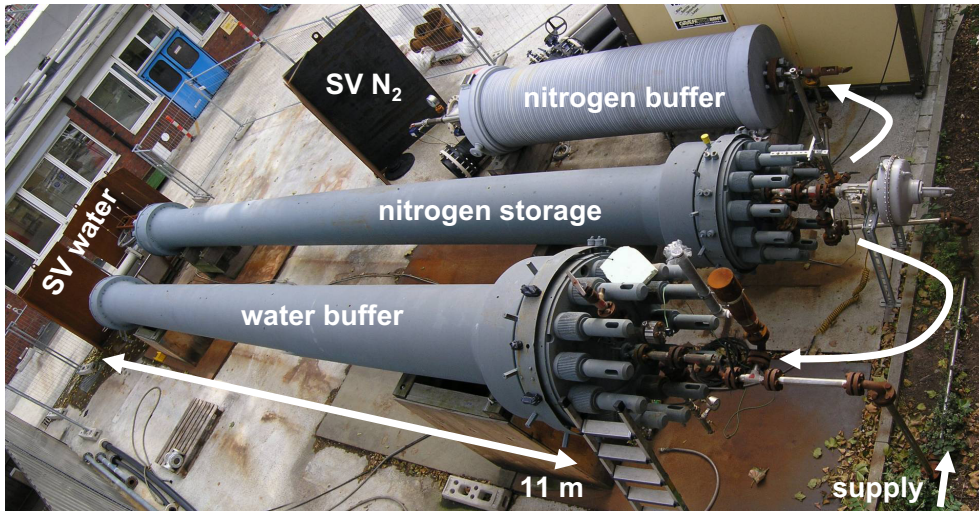


Figure 4.2. Photograph of high-pressure valve test facility at BASF site Ludwigshafen.

subsections, for each quantity a description of the equipment used and the results of a calibration or accuracy analysis are given.

4.2.1 Valve disk lift

In contrast to most existing test facilities the disk lift is measured with a displacement sensor below the pressurized valve spring housing with protection cap. Elevated pressures will build up in the spring housing during measurement leading to an additional pressure force on top of the valve disk. The constraints for the measurement system are:

- measurement range at least equal to the maximum valve disk lift of 4 mm,
- inaccuracy < 1%, i.e. < 0.01 mm for 1 mm disk lift,
- resistant to maximum allowable working pressure of valve housing of 63 bar,
- measurement frequency ≥ 100 Hz,
- severe vibrations on the valve up to 10g at 1 kHz should not disturb the measurement signal,
- minimal friction to valve spindle to allow for undisturbed valve movement compared to measurements without sensor,
- minimal added mass of sensor to valve spindle to allow for similar valve dynamics,
- minimal added volume of valve housing for similar valve dynamics.

Variable	#	Sensor	Range	Inaccuracy
Disk lift	1	Temposonics type R (spring housing)	25 mm	0.0152-0.0323 mm
Disk force	1	HBM U2B (spring housing)	1 kN	12.8-52 N
Temperature	3	thermocouple type K (Vessels B2, B3, B4)	273-313 K	1 K
	2	resistance PT100 (pipes with orifice)	223-323 K	0.3 K
Pressure (gauge)	3	WIKA UT-10 (vessels B2/B3, valve)	20/100/600 bar	0.01/0.05/0.3 bar
	1	SETRA GC206 (vessel B4)	700 bar	0.35 bar
	2	WIKA S-10 (vessels B2/B3, valve)	16 bar	0.01 bar
(absolute) (differential)	1	Rosemount 3051 CA1	2000 mbar	1 mbar
	2	Rosemount 3051 CD1/CD2 (pipes with orifice)	69/690 mbar	0.15/0.83 mbar
Liquid mass flow rate	1	mass balance Bizerba 4000 VE-L	2000 kg	2-3.5%
Gas mass flow rate	4	orifices DN50/100/200/400 acc. to EN ISO 5167	0.04-15 kg/s	1.3%

Table 4.1. Overview of all sensors and their locations of the high-pressure valve test facility.

The valve spindle is guided within a small gap so that friction between the spindle and the guidance rings is minimized. Consequently, only the two translational and the two rotational degrees of freedom perpendicular to the spindle axis that tilt the spindle are weakly suppressed. A non-contact displacement sensor at the side of the spindle is only accurate when the small distance between the spindle and the sensor is constant during opening of the valve. Consequently, this measurement principle is unsuitable to measure the movement of the spindle itself accurately. Alternatively, a MTS Temposonics R-serie analogue magnetostrictive non-contacting linear displacement sensor in combination with a guiding extension is used. This sensor is commonly used in hydraulic applications and therefore resistant to severe vibrations and to high peak pressures up to 750 bar.

In figure 4.3 the setup of the disk lift measurement is shown. The sensor with bar is mounted in an elongated protection cap with pressure sensor tap. Since the minimal available length of the sensor bar is 50 mm the protection cap is elongated with the smallest possible diameter so that the total dead volume still equals the volume of the original protection cap. The top part of the elongated protection cap is the same for other test valve types and sizes, so that the sensor can be used for other

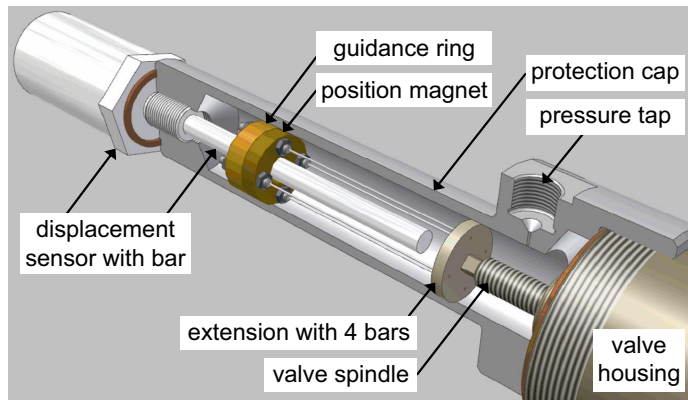


Figure 4.3. Disk lift measurement setup.

valves as well.

On the valve spindle the extension is mounted that consists of four small bars for only high axial stiffness to hold the ring-shaped position magnet and guidance ring. This ring has a sliding tolerance to keep this magnet at the same radial position during valve opening. The bars are thickened in the middle for maximum axial stiffness without decreasing their radial flexibility. A possible skewed alignment of the magnet to the bar does not affect the measurement accuracy and for robustness reasons four bars are used. With this setup small eccentricity of the valve spindle as well as small skewed alignment is allowed resulting in the measurement of the axial disk lift only. A 10-point calibration by rigging the displacement sensor and the position magnet in a CNC lathe with an error smaller than 0.01 mm with a linear fit results in an inaccuracy of 0.0151-0.0323 mm with a 95% confidence interval. The non-parallelism of the extension to the spindle axis of the valve contributes only 10% to the total measurement uncertainty.

4.2.2 Valve disk force

Measurement points of the flow force on the valve disk are only evaluated at almost constant flow conditions in two different situations. In situation 1, the valve disk floats on the flow at constant disk lift h . This disk lift is defined as the distance between the valve seat with surface A_0 and the projected contact circle on the valve spindle in the axis of the valve inlet. The floating disk at constant h can be achieved at constant flow conditions (see figure 4.4). The flow force F_{flow} comprises the net flow force resulting from the flow forces acting upon all sides of the valve spindle, so also back flow forces on the valve spindle are included. Then negligible acceleration forces are present and the flow force is in equilibrium with the spring force.

Friction forces are small as well, because the largest possible eccentricity of the valve spindle that could press the spindle on the guidance rings to create friction is small. Moreover, because of the high pressures the gravitational force will be small

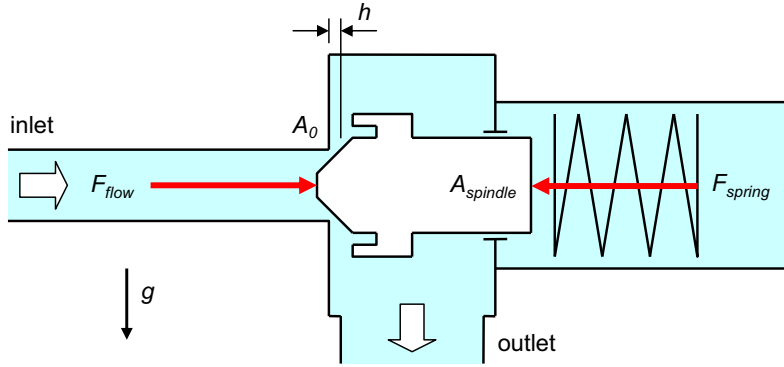


Figure 4.4. Horizontally placed safety valve disk cross-section in force equilibrium.

compared to the flow and spring force, so the orientation of the safety valve is of no importance. In situation 2, the flow presses the valve disk onto a mechanical stop at a certain disk lift. Then at constant flow conditions the flow force is in equilibrium with the spring force and the remaining force applied to the mechanical stop.

Situation 1

The valve disk is at constant opening h during blow-off where the flow force on the disk F_{flow} balances with the spring force F_{spring} . At the set pressure p_{set} of the valve, where the valve should start to open, the disk lift is zero and the spring force equals the set pressure times the seat area A_0 . The set pressure is measured at a small test bench, where the valve is adjusted to the desired set pressure with a series of calibrated analogue pressure gauges. At nonzero disk lifts the spring is deflected further to generate a higher spring force depending on its spring stiffness k_{spring} .

$$F_{flow} = p_{set}A_0 + k_{spring}h \quad (4.1)$$

The spring stiffness is calibrated on a tensile tester with load cells having an accuracy of 0.1% full-scale. Without calibration the spring stiffness is estimated with

$$k_{spring} = \frac{G}{8} \frac{d^4}{D_m^3 n w} \quad (4.2)$$

with shear modulus G , wire diameter d , middle spring diameter D_m and number of effective windings $n w$.

The net flow force F_{flow} can be decomposed into forces acting upon the individual faces of the spindle. Only the rear face of the spindle with area $A_{spindle}$ is in contact with the spring housing. The force $F_{housing}$ on the valve spindle from the elevated pressure in the spring housing $p_{housing}$ is given by

$$F_{housing} = p_{housing}A_{spindle}. \quad (4.3)$$

Situation 2

When the test facility is operated close to its capacity limit it is difficult to control the pressure in the buffer vessel to constant force equilibrium. Therefore, a force sensor measuring the force F_{sensor} acts as the mechanical stop at variable maximum disk lift and allows still accurate force measurement when the spindle moves to this stop. With this mechanism flow forces in a safety valve are measured outside its equilibrium position instead when the valve would move up to the maximum position given by the valve construction itself. When the valve disk reaches the mechanical stop at disk lift h_{stop} the resulting flow force extends to

$$F_{flow} = p_{set}A_0 + k_{spring}h_{stop} + F_{sensor}. \quad (4.4)$$

Figure 4.5 shows the construction of the force measurement with mechanical stop, which is used in combination with the previous described valve disk lift setup. The

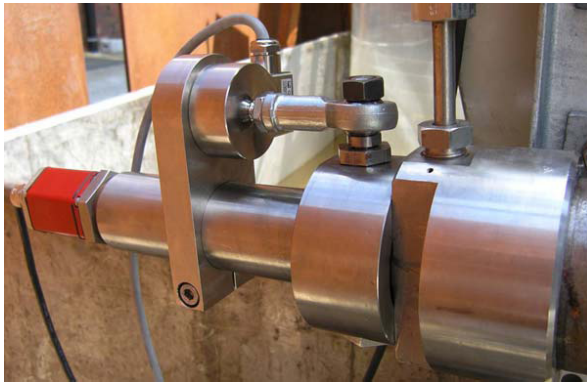


Figure 4.5. Picture of force sensor on protection cap as it is implemented in the test facility.

valve spindle presses on a round bar, which is held at one side with a tight sliding fitting ring working as a joint. The other side is connected with a knuckle eye to the force sensor type HBM U2B with measurement range 1 kN that is fixed on the protection cap. The force sensor consists of 24 strain gauges that linearly change their resistance to elastic deformation and is resistant to excessive side forces compared to its axial force to be measured with an inaccuracy of 0.1%.

The spindle presses at approximately one-third of the bar, so that the force sensor measures approximately the same part of the original force. The protection cap can still be pressurized up to 63 bar because two rubber rings seal the space between the bar and a metal holder which is mounted on the base of the protection cap with sufficient space for elastic deformation of the bar and sensor. To avoid excessive peak forces from damaging the force sensor when the spindle collides with the mechanical stop, a screw with a rubber plate is mounted on top of the spindle to damp the collision forces. This screw is adjusted to the desired maximum allowable disk lift with 0.1 mm inaccuracy.

Due to tolerances of the valve seat diameter, eccentricity of the valve spindle, disk

lift measurement and set pressure determination at the small test rig, the resulting accuracy of the force measurement without mechanical stop is 3.2%. For the measurements with mechanical stop and force sensor, different setup configurations between the use of rubber seal rings and the use of a collision damper between the spindle screw and the bar are calibrated. During a calibration measurement the complete configuration with rubber sealing is subjected to random force changes at different frequencies and amplitudes. These force changes are generated by manually moving the traverse of a tensile tester up and down with variable speeds and positions.

The calibration measurements result in a hysteresis range of 52 N independent of the actual force applied. For the configuration without rubber sealing this uncertainty reduces to 13 N, so the viscoelastic behavior of the rubber sealing causes the largest uncertainty. Nevertheless, the backflow force that would occur in valve experiments with pressurized protection cap is on average five times higher so that measuring with rubber sealing is preferred. For instance, when the total disk force measured is 2 kN, from which 200 N comes from the force sensor, the total uncertainty is still then only 5%.

4.2.3 Temperature

Thermocouples type K measure the total temperature in the storage and the two buffer vessels. The thermocouples consist of two chromel and alumel wires in a circuit where a voltage exists when both connections are subjected to different temperatures due to the thermoelectric or Seebeck effect. The sensor bar with variable length of approximately 1 m is strengthened with ceramic material in a thin stainless steel pipe of 5 mm diameter and reduced at the sensor tip to 2 mm diameter, so that the sensor tip is at least 152.4 mm (ASME, 1998) [6] away from the vessel wall. At the tip the connections of the sensor wires are welded on the pipe wall for fast response. The thermocouples are directly connected to the data acquisition system with the electrically incorporated cold junction as reference temperature and are calibrated (ASTM, 2008) [7] at 0 °C and at 30 °C so that the resulting precision is ± 0.2 K. In practice and due to temperature drift of the sensors, the resulting uncertainty increases to 1 K.

Platinum resistance thermometers PT100 measure gas flows directly downstream of the safety valve and downstream of the orifices. The resistance equals 100 Ω at 0 °C linearly increasing with temperature. The sensor wire with 1.5 mm diameter is placed in a stainless steel pipe with Teflon insulation to minimize heat transfer to the wall with the free sensor tip located in the middle of the pipe. The uncertainty after calibration in combination with the temperature transmitter and data acquisition system is 0.15 K.

Transducers in a flow always detect the so-called recovery temperature, close to the stagnation temperature. When the PT100 sensors are subjected to flow Mach numbers higher than 0.1 the difference between the recovery temperature and temperature of the undisturbed flow becomes significant. Then, the total temperature T_0 at the sensor tip significantly differs from the temperature T_{real} of the fluid far away

from the transducer. The recovery temperature with recovery factor R is defined as

$$\frac{T_0}{T_{real}} = 1 + R \frac{\gamma - 1}{2} Ma^2, \quad (4.5)$$

where the temperatures are in Kelvin. For a wire perpendicular to the flow direction and $0 < Ma < 1$, the recovery factor satisfies $0.84 < R < 0.87$ (Shapiro, 1954) [61]. This leads to a real temperature of approximately 2 K lower than the measured temperature at $Ma = 0.2$. Another measurement error occurs when at low temperatures water vapor condenses on the sensor resulting in too low temperatures. Experiments have shown that this effect occurs at the PT100 sensor directly after the test valve. Fortunately, the second sensor far away from the test valve does not suffer from this effect, because all condensates have already settled down on the pipe wall upstream of the sensor.

4.2.4 Pressure

Gauge pressure sensors WIKA UT-10 with adjustable ranges 20-100-600 bar, SETRA GC206 (700 bar) and WIKA S-10 (16 bar) are used to measure the pressure in the vessels, before the safety valve and in the protection cap. For the gas meter equipment an absolute pressure sensor Rosemount CA1 (2 bar) is used to measure the static pressure in the low-pressure pipe and two differential pressure sensors Rosemount CD1 (62 mbar) and CD2 (620 mbar) are necessary to cover the whole measurement range.

Basically, a (pressure) transmitter should not be operated below 10% of its span, because then the noise level becomes poor and systematic errors become apparent. For the same reason also the turndown, which is the reduction factor of the maximum span, is practically limited to five. The measurement frequency of the pressure transducers with their span equal to or higher than 100 bar is 100 Hz so that high-frequent pressure oscillations do not disturb the measurement signal of interest at lower frequencies.

In all special high-pressure adapter pieces between the buffer vessel and the test valve high-pressure taps at the end of the adapter piece are placed with at least $10D$ constant pipe diameter upstream to achieve a sufficient boundary layer thickness for accurate static pressure measurement within the boundary layer at the pipe wall. The pressure bores are perpendicular to the pipe flow with 1 mm diameter and sharp edges to have a minimal error of smaller than 0.2% when the radii of the edges of the bores are smaller than $0.25D$ (Nitsche, 1994) [50].

All 10-point calibrations are carried out with a hydro-balance module for pressures equal to or higher than 16 bar and high-precision pressure transmitters at lower pressures with a precision of 0.05%. The resulting measurement uncertainty for a time interval of 3 s taking into account the non-linearities of the measurement system and the transmitters, the noise on the signal, the calibration inaccuracy and the temperature and time dependent drift one year after calibration is smaller than 0.25% for all sensors except for the 700 bar pressure transmitter at the storage vessel which is smaller than 0.6%.

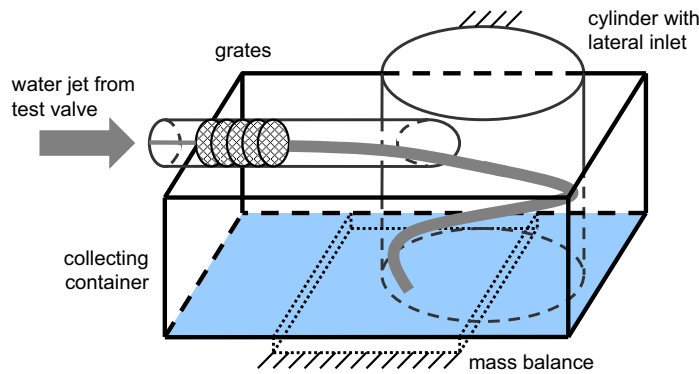


Figure 4.6. Schematic representation of liquid mass flow rate measurement setup.

4.2.5 Liquid mass flow rate

The liquid mass flow rate can be measured in either the high-pressure part just before the safety test valve or in the low-pressure part after the safety test valve at atmospheric conditions. A measurement in the high-pressure part of the setup is preferred for fast response. The conditions for the mass flow measurement system are:

- test fluid water,
- maximum mass flow rate 40 kg/s,
- size of the tank must be large enough for a measurement of at least 40 s,
- insensitivity to valve vibrations,
- not affecting the opening characteristics of the test valve.

At the high-pressure side only an ultrasonic flow meter with its sensors clamped on the outside of the high-pressure entrance pipe could measure the mass flow rate without disturbing the flow at the valve inlet or inducing additional pressure losses. However, excessive accelerations of the test valve up to 10g at a frequency 1 kHz during preliminary high-pressure valve tests resulted in signal failure of the sensor. Therefore, measuring the mass flow rate with a mass balance at the low-pressure side after the safety valve where the water is collected in a tank is the most preferable option. The possibility of transient mass discharge measurement of (multiphase) fluid in a 10 liter reactor in combination with force sensors was previously represented in the work of Koenig (2005) [35].

In figure 4.6 and figure 4.7 the setup of the water mass flow rate measurement is schematically shown. Before the liquid flows into the collecting tank it first passes five vertically placed grids with grate distances from 2 to 10 mm located in a DN200 horizontal cylinder. These grids decelerate the jet flow from the safety valve so that the stream divides across the vertical cylinder. Hereafter, a DN1000 vertical cylinder

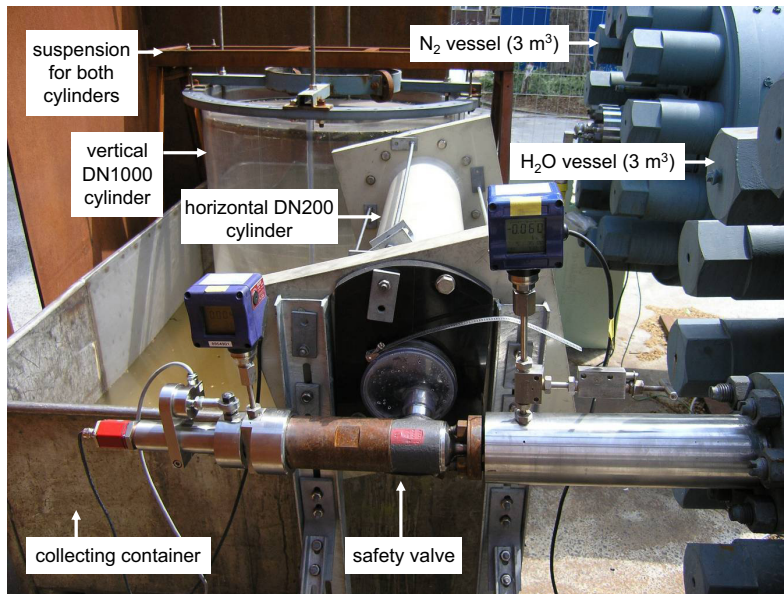


Figure 4.7. Picture of liquid mass flow rate measurement setup.

decelerates the flow further so that the momentum of the flow will minimally disturb the mass reading of the mass balance Bizerba 4000 VE-L with a measurement frequency of 33 Hz and a resolution of 0.0166 kg situated below the collecting tank. The tank volume is 1.6 m³ to allow mass flow rate measurements up to 40 kg/s for a period of 40 s. The cylinders are connected with a bifilar suspension construction to the ground floor of the test rig, separately from the collecting tank and the mass balance, so that the measurement system is mechanically separated from the flow-calming section.

To obtain the mass flow rate, the mass reading is differentiated with respect to time. Two different digital filters, namely a Butterworth filter with a cut-off frequency of 5 Hz and a Savitzky-Golay filter (Savitzky, 1964) [58] with a data window of 3 s reduce the noise of the signal. The Butterworth filter is an anti-causal third-order low-pass filter that is maximally flat in the pass band, so that the signal part lower than its cut-off frequency remains undistorted. The Savitzky-Golay filter performs a local polynomial regression on a number of points to determine the smoothed value of each point. The advantage compared to the moving average method is the tendency to preserve local minima and maxima and that a derivative of the smoothed measurement point can be calculated. The data window is chosen to be 3 s to achieve a $\sqrt{3s \cdot 33\text{Hz}} = 10$ times better signal to noise ratio.

Table 4.2 shows the disturbing factors for an accurate mass flow rate measurement. The momentum correction comprises the momentum force, defined as the vertical velocity multiplied with the mass flow rate, after decelerating the flow by the cylinders

Mass flow rate \dot{m}_l	2 kg/s	20 kg/s
Momentum correction	0.06%	0.6%
Buoyancy forces	0.03%	0.03%
Unbalanced mass	1.6%	0.16%
Wind, calm weather	1.5%	0.15%
Wind, ± 30 km/h	(25)%	(2.5)%
Rain	(1.8)%	(0.18)%
Total expected uncertainty	2.19%	0.64%

Table 4.2. Total uncertainty in the mass flow rate measurement. The numbers between parentheses represent the extra uncertainty due to bad weather conditions.

that impacts on the mass balance. After this correction the uncertainty of the mass flow rate is 0.06% for a low mass flow rate of 2 kg/s and 0.6% a high mass flow rates of 20 kg/s.

The buoyancy is a systematic error in the mass reading, because the vertical cylinder is partially immersed in the water. During a calibration measurement with accurate small masses of water poured into the collecting container the mass reading is corrected for this systematic deviation with a rest uncertainty of 0.03%.

If large amounts of water flow into the container within a short time, waves may be formed leading to a mass imbalance in the container. A slope of the water level in the container is assumed to be 5° at maximum that is simulated with a corresponding weight in the corners of the tank. This imbalance results in an uncertainty of 1.6% for low mass flow rates and 0.16% for high mass flow rates.

Measurements with much wind are not recommended, because this leads to an uncertainty up to 25% for low mass flow rates. For calm weather the analyzed mass flow rate fluctuations around zero without any water flowing into the tank results in an uncertainty of 1.5% for low mass flow rates and 0.15% for high mass flow rates. Measurements in heavy rain with a precipitation rate of higher than 50 mm/hour should be avoided as well.

The total relative uncertainty in the measured mass flow rate decreases with increasing mass flow rate from 2.19% at low mass flow rate to 0.64% at high mass flow rates. When the mass flow rate is not constant but changes 50% in 30 seconds an additional uncertainty of 0.11% has to be added.

The mass flow measurement method is calibrated with a reference Coriolis Endress+Hauser Promass 63 DN80 mass flow meter. Figure 4.8 left shows the results of test series with constant flows up 27 kg/s achieved with an external pump. At the right of figure 4.8 the measurement uncertainty for time windows of 3 and 4 s are given with a 95% confidence interval. The developed mass flow rate measurement system enables measurement of constant mass flow rates with an uncertainty between 2% and 3.5%.

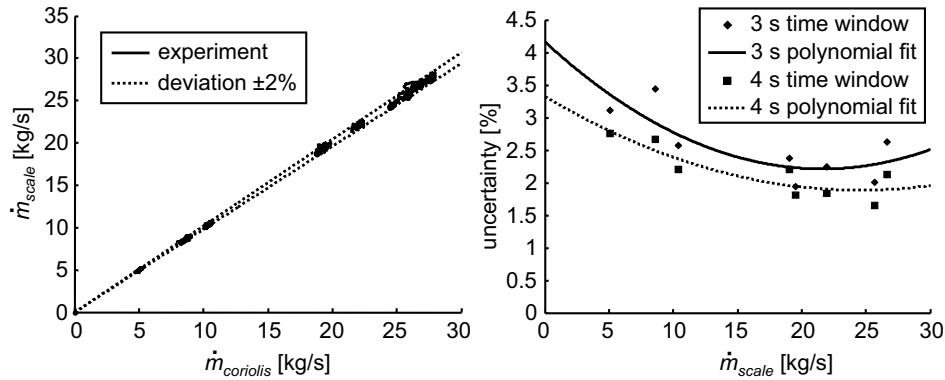


Figure 4.8. Left: Results of the mass flow rate calibration measurements. Right: Uncertainty of the mass flow measurement of a 3 (solid) and 4 s (dashed) Savitsky-Golay filter window.

4.2.6 Gas mass flow rate

Gas mass flow rates are measured at the low-pressure side after the test valve, because at the high-pressure side no device can cover the whole measurement range of 0.02-10 kg/s without inducing excessive pressure losses. With an orifice a subcritical single-phase non-pulsating flow through a straight pipe can be measured. The pressure drop measured over the orifice restriction is a measure for the mass flow rate. To ensure well-defined completely developed flow conditions at the orifice, its geometry with pressure taps, the entry and exit lengths of straight pipe with undisturbed flow and the pipe wall roughness are in accordance to standard EN ISO 5167 [29], so that measurement uncertainties smaller than 1% are achieved without calibration.

To cover the whole measurement range four orifice stages with partial overlap in the measurement range of the mass flow rate for DN50, DN100, DN200 and DN400 pipes are defined. In table 4.3 the sizes of the four orifice stages are given with pipe diameter D_{pipe} equal to the orifice diameter, orifice bore $d_{orifice}$ with the maximum mass flow rate \dot{m}_g corresponding to the maximum pressure difference dp and the pipe velocity u_{pipe} . The dynamic measurement range of the orifice is factor five. The

Stage ND	D_{pipe} [mm]	$d_{orifice}$ [mm]	\dot{m}_g [kg/s]	dp [mbar]	u_{pipe} [m/s]
400	375.4	300	10	152	57
200	209	150	3	226	60
100	93.1	70	0.6	204	46
50	49.2	30	0.12	268	34

Table 4.3. Dimensions of four orifice stages for gas flow rate measurement.

pressure difference ranges from 6 to approximately 300 mbar. At higher pressure differences the pipe velocity becomes too high and the pressure ratio of 0.75 as prescribed in the standard is exceeded.

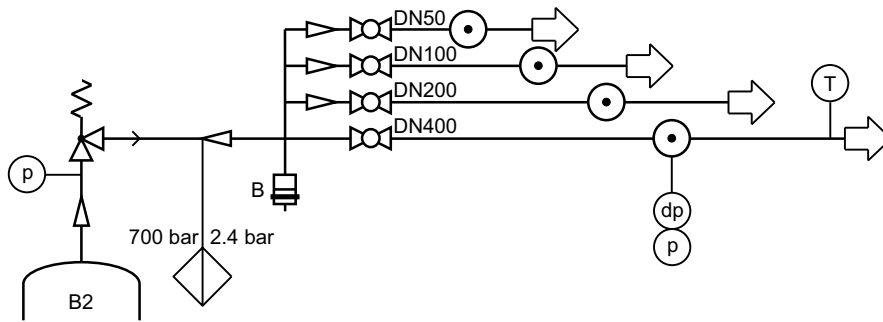


Figure 4.9. Gas measurement configuration with four orifice stages.

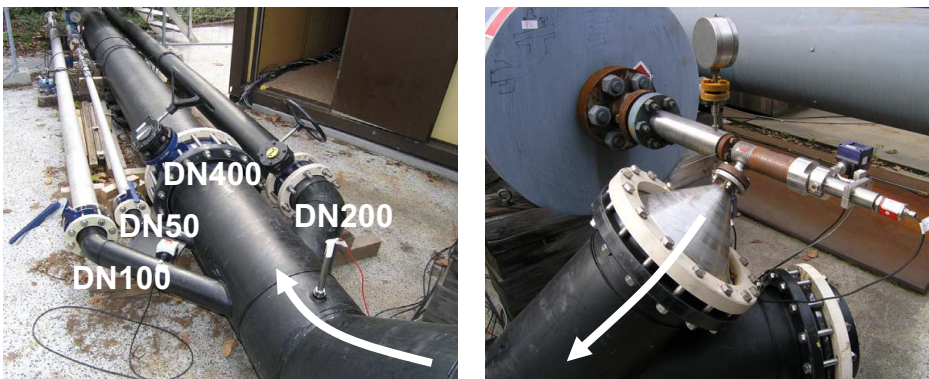


Figure 4.10. Pictures of junction pipe with four orifice stages.

Two types of orifice plates are used. First, an orifice plate with corner pressure taps integrated directly next to the compact orifice geometry is used in the two smaller stages. Second, a single orifice plate with pressure taps at distances D and $0.5D$ from the orifice plate in the pipe is used in the two larger stages. The piping configuration of the gas metering section of the test rig is shown in figure 4.9.

Directly after the safety valve a conical transition piece connects the high-pressure outlet of the test valve with the DN400 orifice stage with diagonal inclined T-junctions to the smaller stages (figure 4.10). Each orifice stage is separated from the test section with a butterfly valve, so that only one orifice is connected. At the rear side of the T-junction, a foil is mounted to act as a rupture disk to protect the gas metering part from overpressure. The straight pipe length between the butterfly valve and the orifice is $44D$ for all four orifice stages and $8D$ after the orifices. To meet the pipe wall roughness limits and for handling reasons the straight pipes of the two smaller stages are made out of seamless stainless steel and the two larger orifices out of PE-HD. The absolute and differential pressure sensors are connected to two pairs of pressure taps, which are 180 degrees staggered from each other to average the pressure mea-

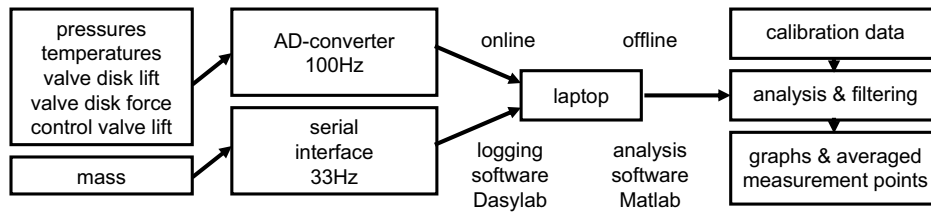


Figure 4.11. Scheme of data acquisition system.

surement. The temperature sensor is mounted between $6D$ and $15D$ downstream of the orifice plate so that the flow is not disturbed upstream of the orifice.

The inaccuracy of the gas mass flow rate measurement is 1.3% when the temperature recovery correction for higher flow velocities is not taken into account. Otherwise it is reduced to 0.8%. The dead volume of the T-junction causes an increase of the response time of the smallest orifice section up to 10 s. For the larger orifices this response time reduces to 1 s and the 16 m long entrance pipe causes an additional delay time of 1 s.

4.2.7 Discharge coefficient

The discharge coefficient is calculated in accordance to standard EN ISO 4126 [30]. For liquids with an uncertainty of the stagnation pressure $p_0 = 0.90$ bar and 2% for the mass flow rate, the uncertainty in the discharge coefficient for liquids equals 3%. For critical gas flow with the uncertainties of the mass flow rate of 1.3%, the same uncertainty of the stagnation pressure $p_0 = 0.90$ bar, specific volume v caused by a stagnation temperature uncertainty of 1 K, the resulting uncertainty in the discharge coefficient for gases is 2.5% for operating pressures $50 < p_0 < 100$ bar and 2% for $p_0 > 100$ bar.

4.2.8 Data acquisition

The analogue signals from the measurement sensors ranging from 4-20 mA or 0-10 V are acquired with a Geitmann 16-channel data analogue-digital converter with a resolution of 12 bit and chosen measurement frequency of 100 Hz with an accuracy of 0.1%. The unfiltered digital signal from the mass balance is serially communicated for maximum resolution and a measurement frequency of 33 Hz. All signals are logged with the data acquisition software program DasyLab version 9.00.02. The data is analyzed offline with the mathematical application Matlab version 5.3, see figure 4.11. To minimize electromagnetic interference, each signal in the AD-converter is galvanically separated. Between the converter and analogue sensors by galvanic separation units the cables are pair-wise twisted and shielded as much as possible. Furthermore, to prevent ground loops all electrical equipment is grounded only on

the test rig if necessary and connected indirectly to the mains power system with a transformer without grounding.

4.3 Examples of valve tests

Before each series of experiments a safety valve is assembled, set to the desired set pressure and mounted into the test facility. Then, a series of valve relief tests are carried out in which the safety valve to be tested remains mounted in the test facility. After a few tests the valve is disassembled and the geometries of the valve housing and spindle, and the stiffness of the spring are measured. In addition, all points of stationary valve operation within each relief test of the same series are collected, from which the opening characteristic is deduced.

In this section for two example tests is demonstrated how the valve capacity and opening characteristic of a safety valve operating with sub-cooled water and gaseous nitrogen are determined.

4.3.1 Valve test with water

Figure 4.12 shows the behavior of all measured quantities of a single safety valve test with water. Prior to the valve test the storage vessel is pressurized at $p_{storage} = 550$ bar and the buffer vessel with the safety valve to be tested is at ambient pressure (4.12 top left), shown by the two measured pressures by the pressure transducer located in the buffer vessel p_{buffer} and just upstream the test valve p_{valve} . When the pressure losses are small the pressure just before the safety valve and the one in the buffer vessel should always be almost equal, which is the case in this example experiment. The pressure in the spring housing $p_{housing}$ is at atmospheric condition.

The control valve is closed and the data logging is started so that the actual valve test begins when the automatic pressure control is activated. Then, at $t = 7$ s the control valve opens (not presented in figures) and the buffer vessel with the test valve is pressurized by high-pressure nitrogen from the storage vessel. At time $t = 12.7$ s the safety valve starts to open, because a disk lift larger than the smallest detectable disk lift of $h = 0.012$ mm is measured. At this time the valve pressure is determined at 362 bar, which is defined as the opening pressure. In figure 4.12 top right the accumulated mass m in the collecting tank and the derived mass flow rate \dot{m} are given. At $t = 15$ s onwards the mass increases from 235 to 502 kg at the end of the valve test with a maximum mass flow rate of $\dot{m} = 6$ kg/s during 23 s.

Figure 4.12 lower left shows the valve disk lift that reaches the mechanical stop $h_{stop} = 1.68$ mm at $t = 16$ s. Although the buffer and valve pressure increases further, because it is difficult to control it at a constant pressure of 465 bar, the spindle moves only little due to the rubber collision damping plate at the spindle top. In figure 4.12 lower right the force sensor measures the remaining flow force $F_{flow} - F_{spring}$ that cannot be compensated by the spring force F_{spring} anymore when the spindle presses on the mechanical stop during the period of 23 s. In the same period with high disk lift the pressure in the spring housing increases to 7 bar.

Around $t = 22$ and 42 s the changes of the pressure, mass flow rate, disk lift and

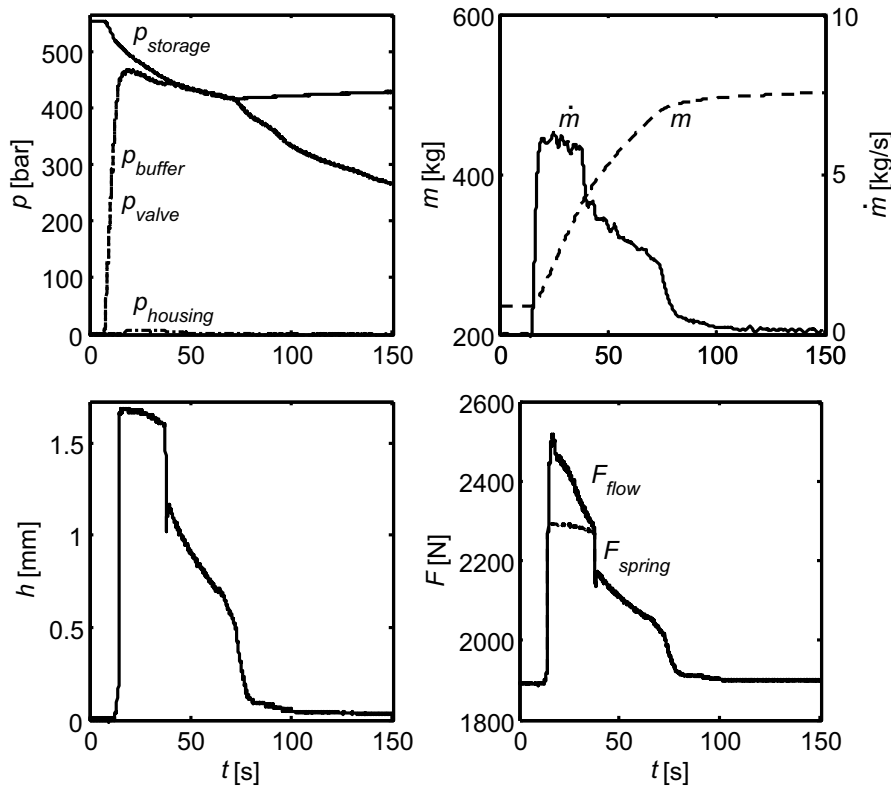


Figure 4.12. Example of valve test with water.

disk force are small enough so that the measurement points around these times are averaged with a measurement interval typically ranging from 1 up to 100 s. Due to the large time scale of the figure the steady conditions cannot be clearly seen. At $t = 72$ s the control valve is closed so that the pressure in the buffer vessel decreases faster and the pressure in the storage vessel starts to increase slowly due to heating of the cold nitrogen gas by the thick vessel walls at ambient temperature. At time $t = 91$ s, the pressure in the buffer vessel decreases faster, because this vessel is also depressurized with a vent valve to avoid chatter of the test valve while closing. Due to damage to the sealing of the valve it does not close entirely to zero disk lift and remains leaking for a longer time that can be seen in still slowly increasing mass in the collecting tank.

4.3.2 Valve test with nitrogen

Figure 4.13 shows the distribution of all measured quantities of a safety valve experiment with gaseous nitrogen. In general the pressure distributions of this valve test are similar to the distributions of the valve test example with water described in

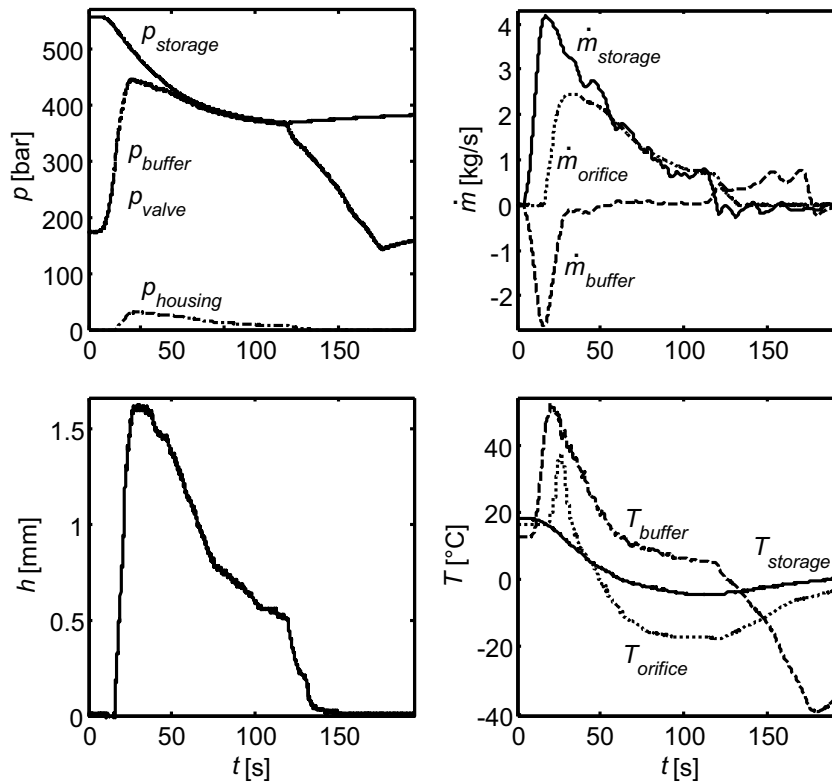


Figure 4.13. Example of valve test with nitrogen.

the preceding section, so only differences are discussed. At $t = 16$ s the safety valve opens at 300 bar measured just before the test valve p_{valve} and the same value in the buffer vessel p_{buffer} . The maximum disk lift is reached around $t = 30$ s and remains constant during 4 s at $h = 1.61$ mm (figure 4.13 lower left). No mechanical stop with force sensor is applied, so that at this point the valve disk still floats on the flow. At this time the pressure in the valve spring housing increases up to $p_{housing} = 30.1$ bar.

It is emphasized that this elevated pressure in the valve housing contributes 20% to the total force on the spindle, which is significant compared to when this valve test would be conducted without protection cap with, as a consequence, a totally other opening characteristic of the test valve. The course of the force is not shown in this figure, because this is similar to the course of the disk lift with the initial value of the force equal to the set pressure of the valve multiplied with its seat area.

In figure 4.13 upper right the temperature in the storage vessel $T_{storage}$ continually decreases until the test valve closes again. Furthermore, due to a fast pressure rise in the buffer vessel, its temperature T_{buffer} increases from 13 to 52 °C and immediately drops after opening of the safety valve. The same temperature variations are observed for the orifice $T_{orifice}$ which are on average 20 degrees lower due to the flow expansion

in the safety valve.

For valve tests with nitrogen it is also possible to measure the mass flow rates by calculating the changing mass in the vessels as function of its total pressure and temperature (figure 4.13 upper right). Unfortunately, due to large temperature variations this experimental method can only be used as indication to check the steadiness of the flow between the storage vessel, buffer vessel and the orifice. Then the flow is steady when the mass flow rate in the buffer vessel \dot{m}_{buffer} is zero and the mass flow rate at the orifice $\dot{m}_{orifice}$ approximately equals the mass flow rate from the storage vessel $\dot{m}_{storage}$.

Furthermore, temperature differences of the gas up to 50 K from the initial value induce additional errors to the gas mass flow rate measurement. Then the flow between the orifice and the temperature sensor cannot be considered adiabatic any more, because the pipe walls are heating or cooling the flow. In addition, the standard EN ISO 5167 [29] assumes that the flow is isothermal, which is justified as long as the pressure losses over the orifice and the resulting temperature differences due to isenthalpic expansion are low.

In principle, the temperature in the buffer vessel always decreases with decreasing pressure. As a result, it is practically impossible to have both pressure and temperature before the safety valve constant during an experiment. Theoretically constant conditions can only be achieved when the volume of the storage vessel reduces as well while relieving. Nevertheless, it is still possible to generate satisfactory stable operating conditions for evaluation as long as the temperature of the gas in the orifices differs less than approximately 20 K from the pipe wall temperature.

Chapter 5

Comparison of numerical and experimental results

The performance of the numerical method is validated with experimental data derived from safety valve tests conducted at the test facility. Section 5.1 focuses on high-pressure valve tests with water at operating pressures ranging from 64 to 450 bar. Section 5.2 presents a re-evaluation of the TÜV measurement with nitrogen as described in section 3.2.6 at an operating pressure of 7 bar. Also experimental and numerical results from high-pressure safety valve tests with nitrogen at operating pressures ranging from 73 to 453 bar are presented. Finally, section 5.3 presents calculations of gas flows through high-pressure safety valves outside the validated pressure region in order to investigate the influence of real-gas effects on the valve characteristics in the largest possible pressure and temperature domain of the numerical method.

5.1 Liquid valve flow

First the experimental results from the valve tests with water are presented. Then, the numerical simulation procedure is given. Hereafter, results of numerical simulations are compared with selected measurement points. In the following analysis, the method is extended to account for cavitation and validated again.

5.1.1 Experimental results

Safety valve test series at set pressures $p_{set} = 50$ and 375 bar are chosen for validation. Typical results are presented in figure 5.1. The measurement points are averaged over five and two valve relief test runs with the same valve at operating pressures between 64-79 bar and 434-450 bar, respectively, attached to the buffer vessel of the test facility. In figure 5.1 upper left the mass flow rate \dot{m} versus the dimensionless disk lift h/d_0 is shown. The dashed vertical line represents the nominal disk lift of 1 mm. The mass flow rate increases almost linearly with disk lift. The small scatter in the

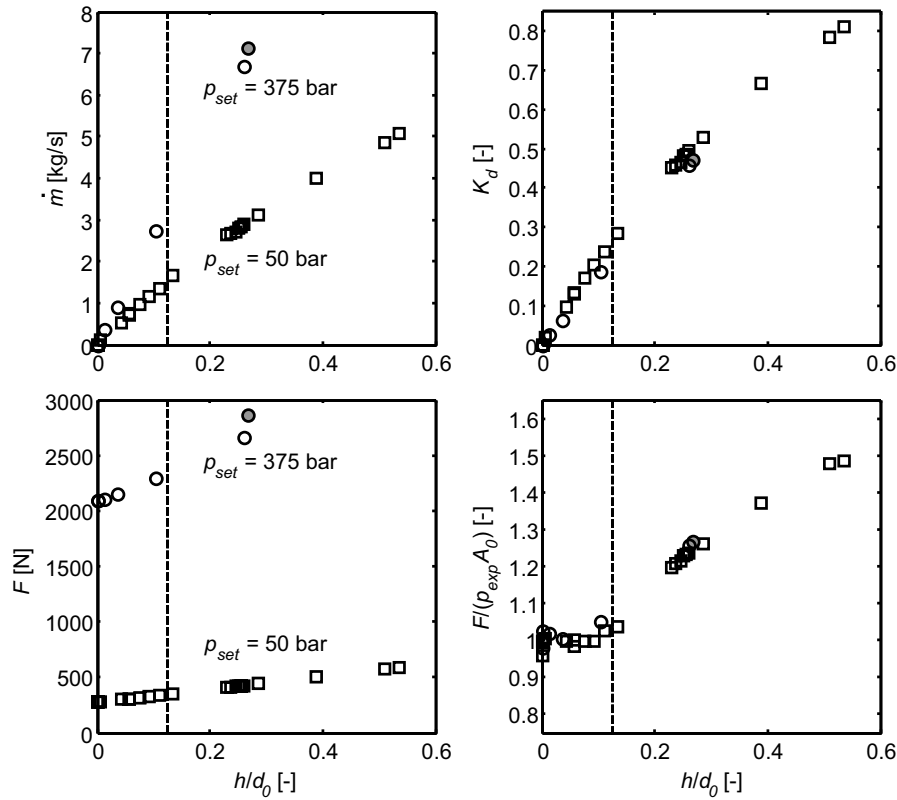


Figure 5.1. Experimental results of averaged data points of safety valve test series water at set pressure 50 and 375 bar. Legend: \square = exp. $p_{set} = 50$ bar; \circ = exp. $p_{set} = 375$ bar; dashed line = nominal disk lift of 1 mm. The grey filled circles represent the measurement with mechanical stop with force sensor attached.

data points indicates that the measurements show a large degree of reproducibility. At the upper right part of figure 5.1 the discharge coefficient K_d collapses on a single curve independent of the set pressure applied. The high-pressure valve test series only shows slightly lower discharge coefficients which is probably due to small differences in the measured seat and spindle geometries.

The bottom left part of figure 5.1 shows the measured valve flow force F , in which for zero disk lift the force equals the pressure at which the valve actually starts to open multiplied with the seat area A_0 . The 50 bar set pressure test series shows linear behavior, but the maximum point (grey filled circles in figure) of the 375 bar test series is substantially higher than the linear behavior of this second series. The reason is that at this point the force was measured with the mechanical stop with force sensor attached. This last measurement point is measured outside its equilibrium position when the valve movement would not have been mechanically limited. This point

can still be compared with the other points when the force is made dimensionless by dividing the actual force by the actual operating pressure p_{exp} at the inlet times the seat area. The results of this dimensionless flow force $F/(p_{exp}A_0)$ are presented in the bottom right part of figure 5.1, where the dimensionless flow force points collapse on the same line as well.

It can be seen that the dimensionless flow force remains around unity until $h/d_0 = 0.1$ and from that disk lift on it starts to increase. For the 50 bar test series a dimensionless flow of 1.5 has been measured at maximum dimensionless disk lift of 0.5. The dimensionless flow force shows larger variations at dimensionless disk lifts smaller than 0.1, because geometry changes due to mechanical wear become apparent. The force at which the valve actually starts to open is calculated from a seat diameter geometry measurement after each valve test series and the average pressure at which the valve actually starts to open in each valve test run. As a result, at zero disk lift all dimensionless flow forces have a value around the average value unity. This method is chosen to average variations in the opening pressure due to geometry changes during a valve test series so that the scatter of the measurement points at larger disk lifts reduces. It has been observed that in the first valve relief test the opening pressure is approximately 3% higher compared to the following test runs within the same series.

5.1.2 Numerical simulations

Four averaged stationary measurement points from the 50 bar test series and two from the 375 bar test series are chosen for validation of the numerical method. The fluid water is used as compressible fluid with the density weakly depending on pressure according to equation (2.14) with temperature 293 K. The steady-state simulations are carried out with uniform water temperature 293 K, constant outlet pressure 1 bar and SST turbulence model. An alternative thermal energy equation suitable for weak compressible flows is used. The computational domain consists of half the safety valve with enlarged inlet as it is mounted on the transition piece on the buffer vessel. Only the first part of this transition piece is modeled where the velocities are small and correspond to the location of a pressure tap. As a result the numerical solution at the inlet boundary is independent of the upstream geometry to the buffer vessel. The outlet is the same as in the experiment where the fluid downstream of the valve is directly exposed to atmospheric conditions without any additional piping that could induce pressure build-up.

The computational domain is discretized with 1.1 million hexahedral grid cells with the mesh generator FLUENT GAMBIT 2.4.6 (figure 5.2). For the axisymmetric section of the safety valve, so without side outlet part, first a planar mesh is created with size functions only for gradual increase of the mesh density with density increase ratios down to 1.025 (front face of axisymmetrical part of right figure 5.2). The densest meshed lines of the planar mesh are the seat and the lifting-aid, where the nodal wall distance is 0.05 mm. The height of the structured boundary layer cells is 0.01 mm with a forced edge-length ratio of unity at the last mesh cell to achieve a gradual increase to the unstructured cells in the bulk flow. The smallest radius of this 2D mesh is 1 mm from the inlet symmetry axis to be able to revolve the mesh around this axis at an angle of 180° to obtain 80 mesh cells in azimuthal direction without

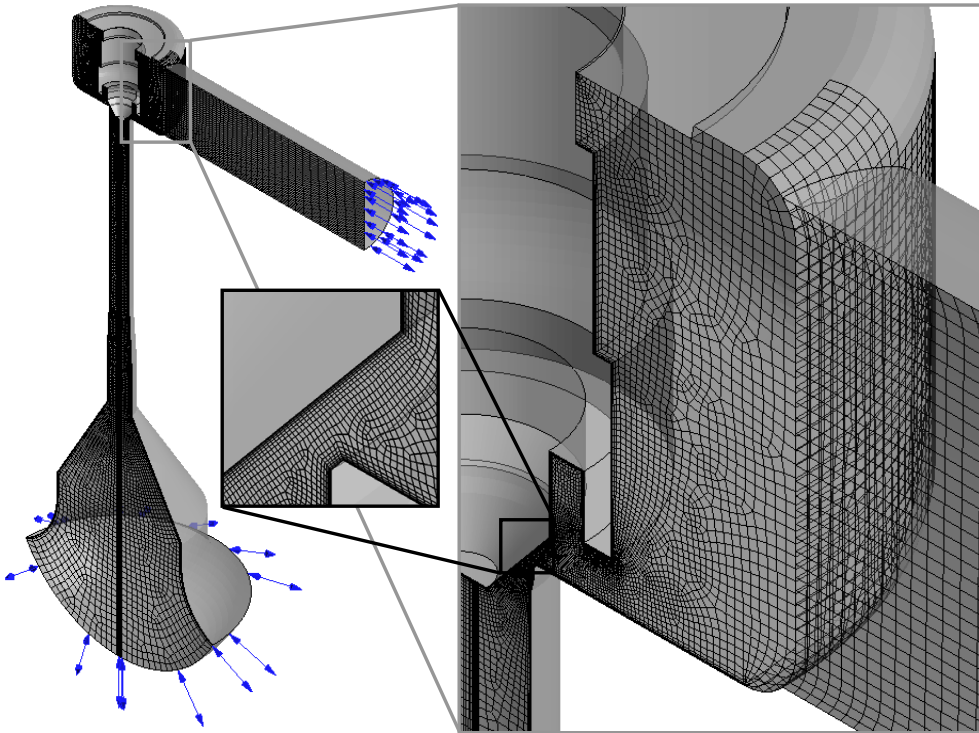


Figure 5.2. Computational domain of a steady flow simulation of safety valve test series with water at set pressure 50 and 375 bar.

generating reduced mesh cells at the symmetry axis (3D mesh partially shown at the top). In this way the mesh is regular in the tangential direction with the advantage of locally increased densities and high mesh quality of the planar axisymmetrical mesh. After revolving the planar mesh the remaining half cylinder volume around the inlet symmetry axis becomes a structured mesh extruded from a planar unstructured mesh at the top surface of the truncated spindle cone.

For the side outlet an unstructured planar mesh is generated with the same mesh density as the revolved 3D mesh that is extruded to the outlet. This means that at the surface between the revolved mesh and the side outlet the face meshes have different topologies, so that only a general grid interface can connect both meshes within the computational domain (both surfaces shown). The drawback is that interpolation inaccuracies occur, but this interface is located in a region where no large gradients occur. In the regions with the largest flow gradients the geometrical mesh quality, such as grid-line orthogonality and small expansion rates of the element volumes, has to be optimal to reduce truncation errors and increase solver robustness.

5.1.3 Comparison and analysis

Figure 5.3 shows the results of the numerical calculations together with the six selected averaged data points of the water experiments. At low disk lifts the mass flow

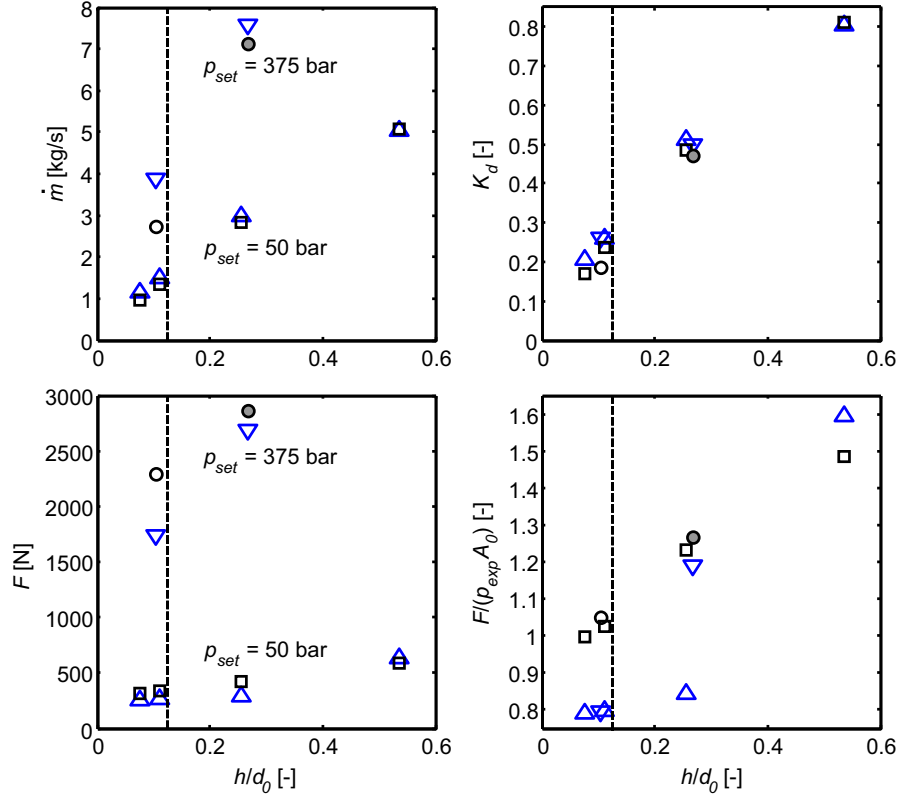


Figure 5.3. Comparison of experimental and computed mass flow rates and disk forces for water of safety valve test series at set pressures 50 and 375 bar. Legend: \square = exp. $p_{set} = 50$ bar; \circ = exp. $p_{set} = 375$ bar; \triangle = CFX $p_{set} = 50$ bar; ∇ = CFX $p_{set} = 375$ bar; dashed line = nominal disk lift of 1 mm. The grey filled circles represent the measurement with mechanical stop with force sensor attached.

rate is overpredicted up to 41% for test series $p_{set} = 375$ bar and 21% for 50 bar set pressure. The forces are underpredicted with deviations up to 30% for test series $p_{set} = 375$ bar and 35% for the test series with 50 bar set pressure. At the highest disk lifts of each test series satisfactory agreement is found.

In order to find an explanation for the large differences between the experimental and numerical results at small disk lift, the simulation results are studied in more detail. It has been observed that negative pressures occur in the smallest cross-section which are in absolute value in the same order as the operating pressure at

the inlet. In incompressible flow computations negative pressures are possible in a converged solution, because an absolute pressure is not defined and all calculated pressures depend on a chosen reference pressure. In reality, cavitation already occurs at absolute pressures in the order of 10 mbar for water, but in the present model this is not taken into account. In order to investigate its effect on mass flow rate and flow force, the standard cavitation model of CFX has been applied. Cavitation is a phase change at almost constant temperature and is due to a local drop in the pressure generated by the flow itself. The degree of development is defined by the cavitation number σ (Agostino et al., 2007) [17]:

$$\sigma = \frac{p_{ref} - p_v}{\frac{1}{2}\rho u^2} \quad (5.1)$$

where p_{ref} is the reference pressure of the liquid, p_v the vapor pressure and u the characteristic velocity as part of the denominator representing the dynamic pressure. When the cavitation number decreases the flow tends to cavitate more. The temperature of the incompressible flow is assumed constant so that the corresponding vapor pressure for water is constant and equal to $p_v = 3.169$ kPa. The Rayleigh-Plesset equation models the mass transfer between the liquid and the vapor phase by describing the growth and collapse of a vapor bubble in a liquid. Then the rate of vaporization and condensation is controlled by liquid-vapor pressure differences derived from a mechanical balance. This model does not take any thermal effects into account. The total interface mass transfer rate per unit volume \dot{m}_{lg} for vaporization is defined as (Singhal, 2002) [63]

$$\dot{m}_{lg} = F \frac{3r_g\rho_g}{R_B} \sqrt{\frac{2}{3} \frac{|p_v - p|}{\rho_l}} \text{sign}(p_v - p), \quad (5.2)$$

where F is an empirical factor with the default value in CFX equal to 50 for vaporization, r_g the volume fraction of the gas phase and $R_B = 1 \mu\text{m}$ the radius of the nucleation sites. When the vapor pressure is higher than the local pressure the fluid vaporizes relatively fast in comparison with the situation that the local pressure is lower than the saturation pressure so that eventual vapor in a control volume condenses. Then in equation (5.2) variable r_g needs to be replaced with $r_{nuc}(1 - r_g)$ to

$$\dot{m}_{lg} = F \frac{3r_{nuc}(1 - r_g)\rho_g}{R_B} \sqrt{\frac{2}{3} \frac{|p_v - p|}{\rho_l}} \text{sign}(p_v - p), \quad (5.3)$$

where F is an empirical factor equal to 0.01 for relative slow condensation compared to vaporization and $r_{nuc} = 5 \times 10^{-4}$ the empirically determined volume fraction of the nucleation sites. This predefined volume fraction is still three orders of magnitude lower than the computed volume fraction where cavitation actually occurs. The cavitation model is implemented as a homogeneous multiphase model with assumed no-slip velocity conditions between the two phases. The cavitation appears as a volume source term in the continuity equation that is solved in a separate transport equation set. The vapor phase is modeled as a gas with constant material properties.

The steady flow simulations are initialized with zero velocity and gradually decreasing pressure field from the inlet to the outlet with a function according to equation (3.21). The simulations with cavitation model are initialized with the solution fields from the simulations without cavitation model and with zero gas phase at the boundaries. The steady flow simulations do not completely stabilize with sufficiently low local residues, but the actual mass flow rates and disk forces are averaged at the moments that the differences of the fluctuating mass flow rates between the inlet and outlet are below 5%.

Figure 5.4 shows the results of the simulations extended with the cavitation model compared to the experimentally determined mass flow rates and disk forces. The

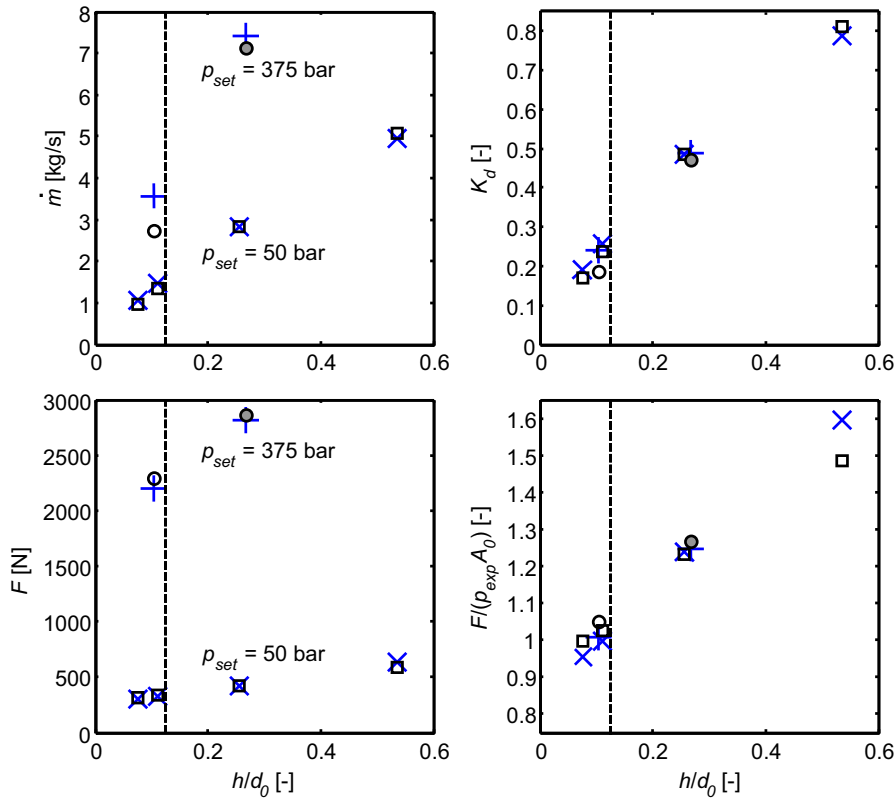


Figure 5.4. Comparison of experimental and computed mass flow rates and disk forces with water of safety valve test series at set pressures 50 and 375 bar with cavitation model. Legend: \square = exp. $p_{set} = 50$ bar; \circ = exp. $p_{set} = 375$ bar; \times = CFX $p_{set} = 50$ bar; $+$ = CFX $p_{set} = 375$ bar; dashed line = nominal disk lift of 1 mm. The grey filled circles represent the measurement with mechanical stop with force sensor attached.

simulations with cavitation lead to a significantly better agreement with experiment: deviations in the mass flow rate are gradually reduced by a factor of two up to 23%,

while deviations in the flow force are strongly reduced from 35% to 7% at lower disk lifts. At the highest disk lifts with cavitation model the mass flow rates deviate down to 4 and 3%, respectively, and the flow forces 5 and 0.5%, respectively.

The different effects of cavitation at lower and higher disk lifts can be visualized by means of contour plots of the solution variables pressure p and liquid volume fraction r_l . In the top right contour plot a large vapor bubble around the valve seat actually reduces the smallest liquid flow cross-section resulting in a lower computed mass flow rate than without cavitation. At the large disk lift no cavitation occurs in the smallest flow cross-section so that the mass flow rate is less affected. In addition to high disk lifts the lowest pressure of the solution field is of the same order as the vapor pressure so that cavitation effects are less apparent.

In figure 5.5 the left two contour plots show the symmetry plane of the valve housing with the pressure contours of the lowest and the highest disk lift of the 50 bar test series. The white line represents the saturation pressure line with $p_v = 0.032$ bar. The two contour plots at the right show the liquid volume fraction of the same cuts of the computed valve flows. Because of the strong asymmetry of the flow both sides of the symmetry plane are shown. At the lowest disk lift $h/d_0 = 0.076$ the flow

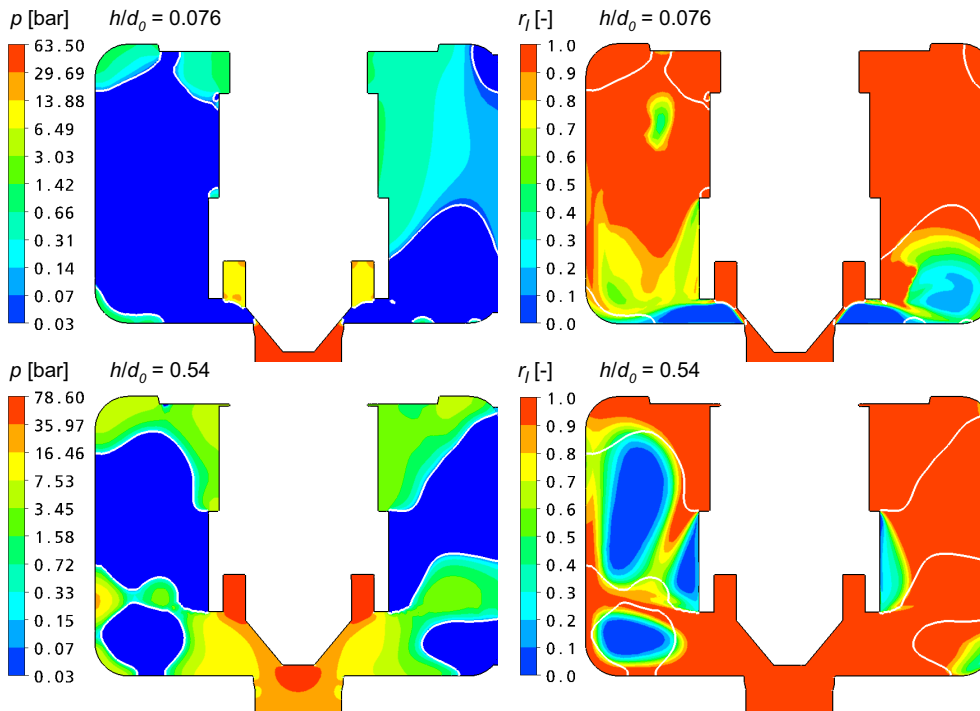


Figure 5.5. Left: Contour plots of logarithmically scaled pressure at symmetry plane of safety valves at $p_{inlet} = 63.5$ bar at $h/d_0 = 0.076$ and $p_{inlet} = 78.6$ bar, $h/d_0 = 0.54$ both at $T_{inlet} = 293$ K. Right: Contour plots of the same valve flow with the liquid volume fraction r_l . The white lines represent the saturation pressure line.

already cavitates in the geometrically smallest cross-section of the flow. In this area the pressure becomes higher compared to the simulations without cavitation and the water vapor volume fraction is close to zero at the lower part of the seat that limits the effective flow area. Further away from the spindle the pressure is still below the vapor pressure but the liquid volume fraction increases again resulting in a limited extent of the two-phase region. At the highest disk lift $h/d_0 = 0.54$ the flow remains single-phase between the valve seat and spindle since it first starts cavitating after passing the spindle. As a result the pressure under the spindle is not directly affected. The insensitivity to cavitation at high disk lifts is also confirmed by comparing the mass flow rate and the flow force.

In conclusion, it is possible to use this numerical method for basically incompressible liquid flows at high pressures, where additional compressibility mainly stems from cavitation effects instead from the weak compressibility of the liquid itself. This preliminary study showed that cavitation is probably an important physical phenomenon that determines the flow in a safety valve, where in this first approach the recommended settings of the Rayleigh-Plesset model in ANSYS CFX are used.

Although the existence of large areas of two-phase flow has not been experimentally proven, the valve experiments have been extremely noisy probably caused by imploding vapor bubbles in the test valve. Furthermore, the deviations of the mass flow rates are still large which indicates that the effect of cavitation is even not modeled strong enough. It is recommended that for high pressures this model has to be extended to account for thermal and compressibility effects of the vapor phase. Also the empirical vaporization and condensation rates that delay or accelerate the growth and collapse of cavitation bubbles may have to be adjusted.

From the comparison between the lower set pressure 50 bar and high set pressure 375 bar test series it can be deduced that in the investigated high-pressure region neither the discharge coefficient nor the normalized disk force depend on the set pressure of the safety valve applied. That means that when such a valve is operated at higher pressures the spring stiffness should be stiffened with the same factor as the set pressure increases. A liquid valve flow is scalable to higher pressures even when cavitation has a large influence on the flow.

5.2 Gas valve flow

This section starts with the re-evaluation of the low-pressure capacity measurement as presented in section 3.2.6, whereafter the results of high-pressure valve tests with nitrogen are compared with the numerical calculations.

5.2.1 Re-evaluation of low-pressure safety valve measurement data

The safety valve capacity measurement of TÜV Rheinland Aachen (1988) [68] is compared with results of the numerical method, which is the only validation test case that shows large deviations between the literature data and the numerical results. This section replicates the same valve capacity measurement with safety valve 10 mm with

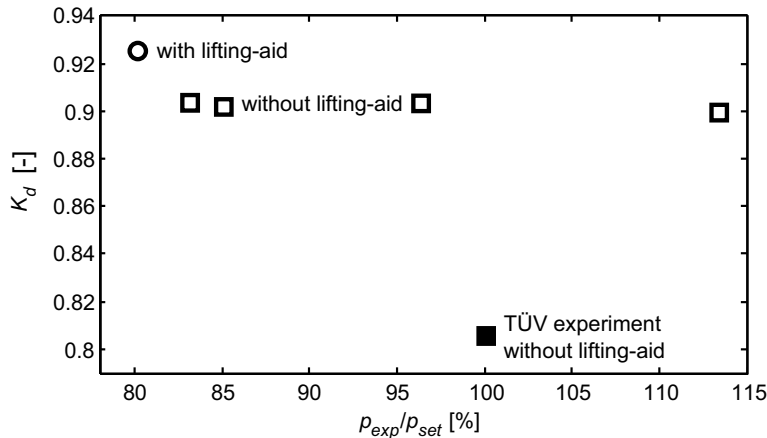


Figure 5.6. Reference discharge coefficient of valve 10 mm with fixed spindle without lifting-aid at $h/d_0 = 1$, $p_{inlet} = 7$ bar and $T_{inlet} = 293$ K with air compared with new experiments of the same valve geometry around 7 bar inlet pressure, $T_{inlet} = 283 - 308$ K and with a valve geometry with spindle with lifting-aid (the spindle is removed) with nitrogen.

exchangeable seat and valve spindle without lifting-aid at the largest mechanically fixed dimensionless disk lift of $h/d_0 = 1$. In figure 5.6 the results of the discharge coefficient from the measurements carried out at the high-pressure test facility are compared with the TÜV measurement point. In total four stable flow conditions are achieved suitable for accurate averaging. The measurement point with lifting-aid refers to the valve geometry given in the construction drawing of figure 1.1. All other valve measurements presented in this thesis refer to the same valve geometry.

It can be seen that the TÜV measurement yields a 10% lower discharge coefficient than measurements at the high-pressure test facility with the same geometry at pressures of 17% and 15% lower than 7 bar and 13% higher than 7 bar, which all result in the same discharge coefficient. The geometry with lifting-aid is measured with infinite disk lift, so no spindle is mounted. This geometry has a slightly higher efficiency, because the flow can expand more due to more space between the valve seat and disk. Only for this geometry a numerical simulation with an axisymmetric computational domain is carried out as described in section 3.2.6. A numerical simulation of this geometry reduced the deviation of the discharge coefficient between the experiments and the numerical method to below 3%.

No clear reason for the difference between both experimentally determined mass flow rates can be given. A first possibility is that the capacity tests conducted in 1988 at the certified test facility in Aachen would yield 10% wrong values. Second, the valve geometry could be different. Since the mass flow rates have been compared with each other differences in the computed discharge coefficients can be excluded. The most probable reason is that the geometries are different although a construction drawing is available.

In conclusion, the experiments and numerical simulation of the safety valve capacity

test with the same valve according to the construction drawing as measured by TÜV Rheinland Aachen agree within 3% and both deviate from the TÜV measurement by almost 15%.

5.2.2 Numerical simulation of high-pressure valve tests

Safety valve tests with nitrogen carried out in the test facility with set pressures $p_{set} = 62$ and 251 bar are chosen for validation of the numerical method. The measurement points with stable operating conditions are deduced from three respectively five valve relief test runs with the same valve at corresponding operating pressures between 73-95 bar and 387-453 bar. The results are given in figure 5.7.

The top left of figure 5.7 shows all averaged measured points of both safety valve

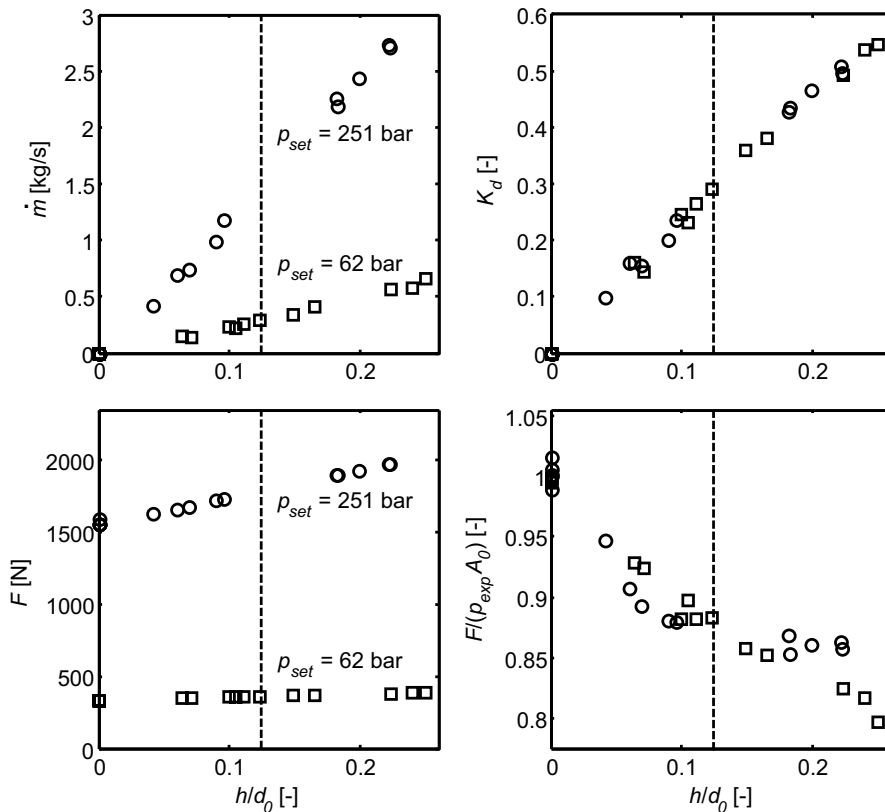


Figure 5.7. Experimental results of averaged data points of safety valve test series with nitrogen at set pressures 62 and 251 bar. Legend: \square = exp. $p_{set} = 62$ bar; \circ = exp. $p_{set} = 251$ bar; dashed line = nominal disk lift of 1 mm.

test series, where both mass flow rates linearly increase as a function of the dimensionless disk lift. At the top right figure, the discharge coefficient is calculated with the

ideal valve sizing method presented in section 2.1. In this pressure region the scatter of the measurement data is larger than the differences between the low-pressure and the high-pressure valve test series. In addition, the deviation of the dimensionless flow coefficient between the *real-average* and the *ideal* sizing method is smaller than 3%. The maximum compressibility factor of the averaged measurement values with constant flow is $Z = 1.31$. The maximum disk lift is due to mechanical limitations only half of that in the water experiments. Consequently, the geometrically smallest flow cross-section is always between the valve seat and valve spindle, so that the smallest flow area always increases with increasing disk lift. When the dimensionless disk lift would be higher than approximately 0.5, the choking plane would move to the seat so that with further opening the smallest flow area and thus the discharge coefficient would not increase any more.

In the bottom right figure it is shown that the dimensionless flow force always decreases linearly with disk lift. In section 4.2.2 the resulting uncertainty of the flow force is determined to 3.2%. The scatter in the figure is mainly caused by large temperature variations during the valve test. In contrast to the water experiments, the dimensionless flow force always decreases with dimensionless disk lift. Although strictly seen all measurement points collapse on the same line within the measurement uncertainty, a weak tendency of the faster decrease and stabilization of the dimensionless flow force around 0.86 of the 251 bar series can be found. Similar to the water tests the dimensionless force at zero disk lift is calculated with the average opening pressure of each test series so that the value varies around unity as well, where the variation between the experiments is reduced to lower than 2%.

From the two safety valve test series three averaged steady-flow measurement points from the series with set pressure 62 bar and two points from the test series with 251 bar set pressure are chosen for validation. The computational domain is basically similar to that in the water simulations with the difference that the first cell thickness of the boundary layer is reduced to 0.002 mm with the same smallest nodal distance of 0.05 mm. Then the dimensionless wall-normal coordinate y^+ according to equation (3.17) is at maximum 400 at the valve seat and spindle.

For all simulations a grid is used with 1.8 million hexahedral grid cells. The conical transition piece at the outlet as shown in figure 5.8 as constructed in the test facility is included in only one simulation as part of a sensitivity analysis. This transition piece is directly attached to the safety valve outlet with diameter 24 mm and starts with a sudden enlargement by means of a short straight pipe with a length of 30 mm and diameter of 29.5 mm with the conical enlargement to the DN400 pipe. In the analysis in section 5.2.3 the influence of this and other variations of the computational domain are discussed.

The fluid nitrogen is modeled as a real-gas described in section 2.3. For all simulations the same real-gas property tables are used. The SST turbulence model is used as presented in subsection 3.1.1, because it is generally considered to perform best for this type of flow although the flow parameters are proven to be insensitive to the turbulence model used (see the sensitivity study in section 3.2.6). The SST model is also the most robust two-equation turbulence model. Furthermore, the steady-state

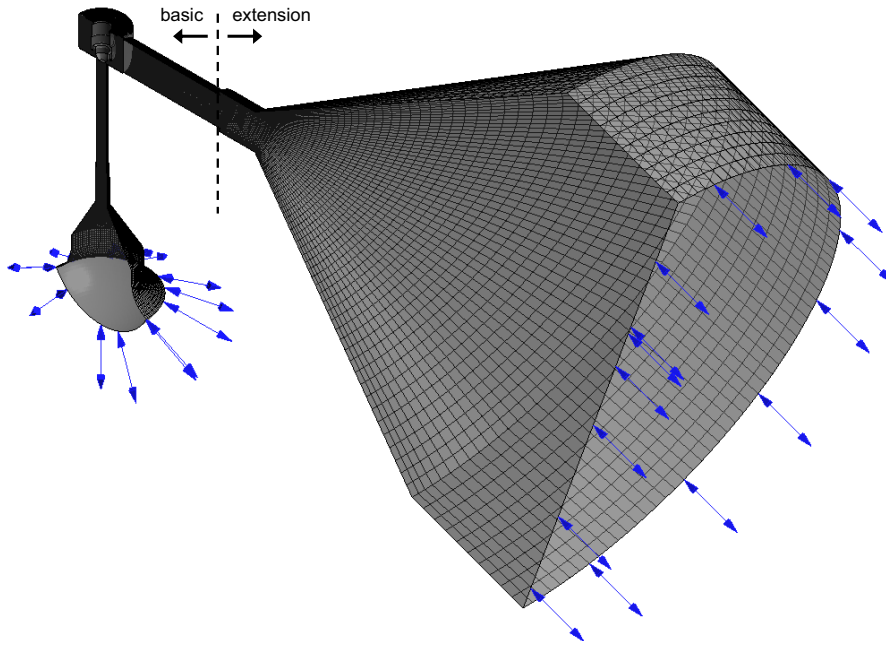


Figure 5.8. Computational domain of a steady flow simulation of basic safety valve geometry with enlarged cone at the outlet.

simulations are carried out with the discretization schemes as given in section 3.1.2.

The steady flow simulations are initialized with zero velocity field, uniform inlet temperature and a pressure field that changes from the measured constant inlet pressure to the initial outlet pressure $p_{outlet,0} = 0.99p_{inlet}$ with the hyperbolic tangent function similar to equation (3.21). This means that the corresponding flow velocities are low in the first iterations, which ensures a stable start of the simulation. While iterating the pressure at the outlet exponentially decreases to approximately 1 bar after 650 iterations. With this approach the high-pressure part upstream of the narrowest flow cross-section is already at the experimentally measured pressure. Then oscillations in the solution variables mainly occur at the low-pressure side, which induced less variations of the mass flow rate and flow force during solving.

With this setup the flow gets slowly choked with excellent stability. However, during iteration the normalized equation residues do not sufficiently reduce so that the disk force remains fluctuating with differences up to 5% from the averaged value. As a result, it is chosen to extract and average only disk force values for which the mass flow rate at the inlet balances with the mass flow rate at the outlet. Also the pressure in the spring housing that counteracts on the spindle should be relatively constant.

It is proven with steady flow simulations that the averaged forces deduced from not completely steady-state solutions do not significantly differ from a stabilized transient

solution. Depending on the stability of the numerical problem a steady flow computation on a 32 bit LINUX cluster partitioned over 4 Intel Xeon 5130 dual-core processors at clock rates of 2 GHz parallel computing the flow on 8 cores takes up to approximately one day. A transient calculation with the same computational capacity up to the point that the solution shows repetitive oscillating behavior takes more than two weeks.

5.2.3 Comparison and analysis of high-pressure valve tests

This section starts with a comparison of the results of the numerical simulations with the selected points of the two test series shown in figure 5.7. Then in contour plots the compressible high-pressure flow is visualized. Hereafter, in a sensitivity study the effect of condensation, transient effects and variation of the computational domain on the valve parameters are studied with the focus on the pressure field around and force distributions on the spindle. Finally, the effect of mechanical wear is discussed.

Figure 5.9 shows the results of the numerical simulations with the three selected low-pressure and two high-pressure averaged measurement points of the gas experiments. In the top left graph of figure 5.9 the mass flow rates of all points show deviations with experimental data within 3.6%. Consequently, the discharge coefficient calculated with the ideal gas nozzle flow model with real-gas property data (*ideal* valve sizing method in section 2.1) turns out to be independent of the operating pressure in the range from 73 to 453 bar consistent with the experimental results. In contrast, the disk forces in figure 5.9 bottom left show an approximately constant deviation between 11.2 and 7.8% for the three low-pressure measurement points and 14.7 and 13.1% for the two high-pressure points. The deviations are already present at low disk lifts. The deviations of each test series are clearly visualized in the bottom right graph of figure 5.9 where the deviations become slightly smaller at larger disk lifts.

Flow visualization

The validation shows that the numerical method accurately resolves the mass flow rate of safety valve flows. The disk force calculation needs attention and that is the focus of this section. The flow inside a safety valve is characterized by three independent variables Mach number, pressure and temperature. The Mach number represents the ratio of the velocity and the local speed of sound according to equation (2.4). The force distribution on the valve disk is directly related to the pressure. The temperature shows local heat effects of the flow. Figure 5.10 shows the Mach number distribution on the symmetry plane of the safety valve with nitrogen at the highest inlet pressure of 452.8 bar and inlet temperature 306 K at dimensionless disk lift of 0.22. The outlet is dimensioned as it is constructed in the test facility. At the inlet the Mach number is smaller than 0.01 so that the solution at the inlet is well-defined and geometry influences upstream of this section can be neglected. The flow accelerates to sonic velocity at the narrowest cross-section between the valve seat and spindle, which is represented by the black line. Here the mass flow rate is blocked and only depends on the inlet pressure and temperature. Within this region the area is supersonic with further acceleration up to $Ma = 3.5$. At the outlet of the axisymmetrical valve part

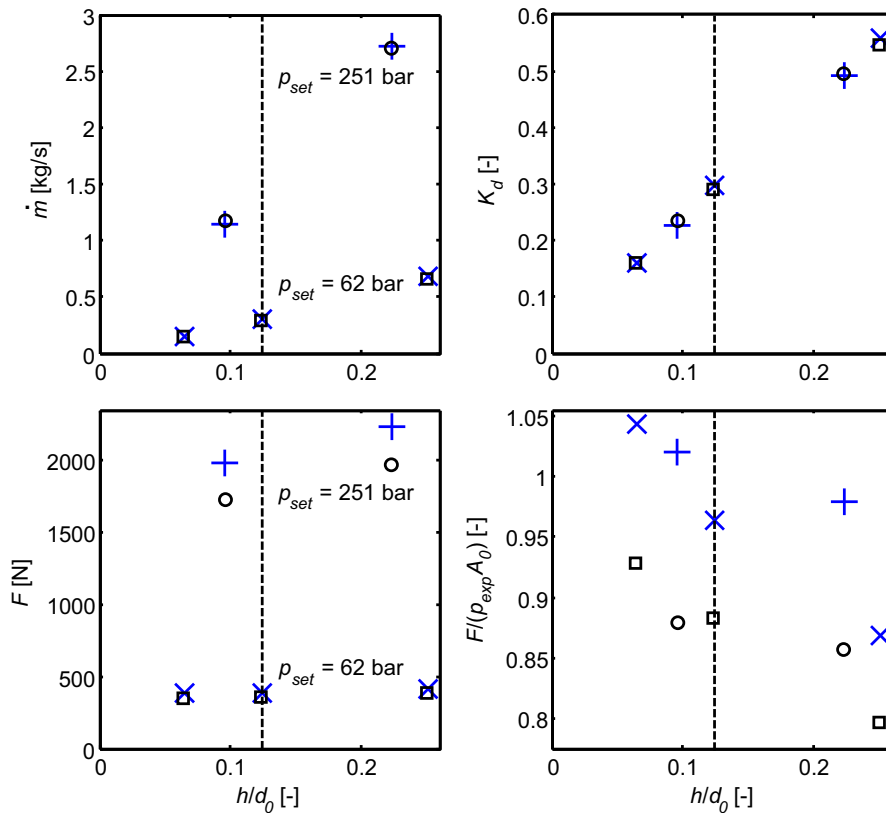


Figure 5.9. Comparison of experimental and computed mass flow rates and disk forces with nitrogen of safety valve test series at set pressures 62 and 251 bar. Legend: \square = exp. $p_{set} = 62$ bar; \circ = exp. $p_{set} = 251$ bar; \times = CFX $p_{set} = 62$ bar; $+$ = CFX $p_{set} = 251$ bar; dashed line = nominal disk lift of 1 mm.

the flow becomes partially supersonic again until it completely chokes at the outlet of the safety valve. At this point the mass flow rate is limited again, so that enhanced pressures in the valve housing emerge. In the conical outlet a further expansion with similar high Mach numbers occur, where the flow at the outlet boundary of the computational domain is still partially supersonic. Since the flow at the outlet of the safety valve is completely supersonic the geometry downstream of the outlet should not influence the flow upstream.

Figure 5.11 shows the Mach number, pressure and temperature distribution of the left part of the symmetry plane of the same safety valve. In the left plot high Mach numbers are present in the supersonic flow area with repetitive plumes, where the last plume is detached from the other ones. This shape is similar to overexpanded nozzle flows, where various reflected waves form a diamond pattern throughout the free jet flow. The limited space in the housing suppresses the flow to expand further,

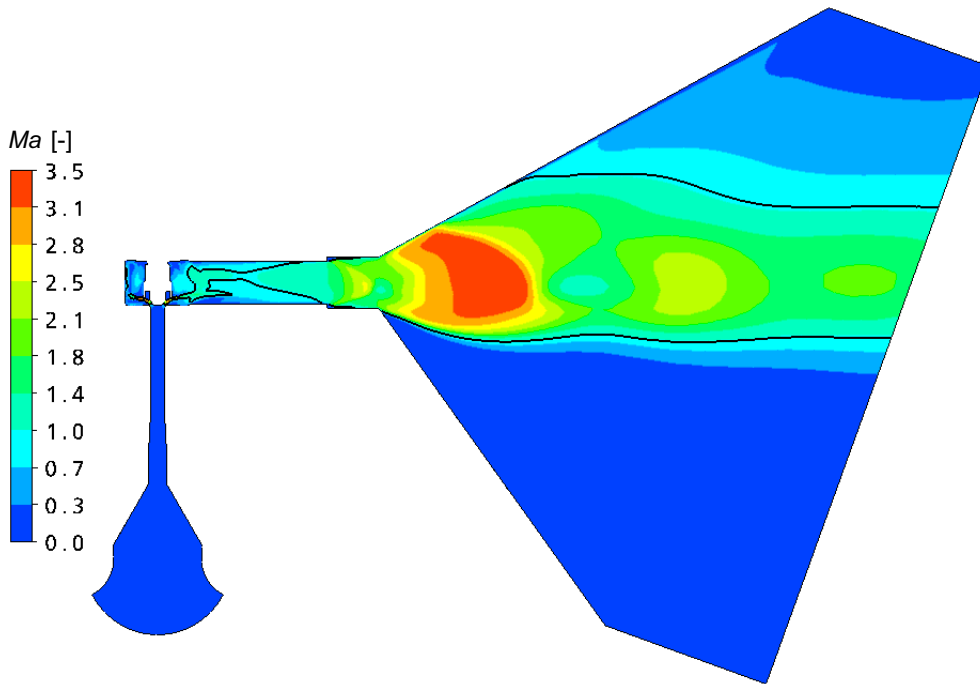


Figure 5.10. Contour plot of Mach number at symmetry plane of safety valve at $p_{inlet} = 452.8$ bar and $T_{inlet} = 306$ K at $h/d_0 = 0.22$. The black line represents the sonic flow line at which $Ma = 1$.

so that a second large expansion area with a strong shock at the outlet is necessary to increase the entropy to balance with the thermodynamic state with lower potential energy at the outlet as shown in figure 5.10.

For visibility reasons the pressure contours in the middle of figure 5.11 are plotted on a logarithmic scale with an increased minimum range from 10 bar instead of the computed minimum absolute pressure of 74 mbar at the secondary large supersonic area in the outlet. Due to the elevated pressure in the valve housing the minimum pressure in the supersonic flow area equals 8 bar. The flow expands from the inlet pressure of 452.8 bar to a pressure of 75 bar in the cavity of the lifting-aid and to 150-210 bar on the tip. In the valve tests also the pressure of the spring housing is measured. At the measurement points this pressure is constant as well, so that dynamic effects and pressure losses that would occur in the small gap connecting the valve housing with the spring housing do not have to be taken into account. As a result only the connecting face between the gap with tolerance 0.1 mm and the valve housing is defined as a separate wall boundary condition. This measured pressure is in this valve test at the highest operating pressure of 452.8 bar equal to 34 bar. The numerically obtained pressure is 27 bar.

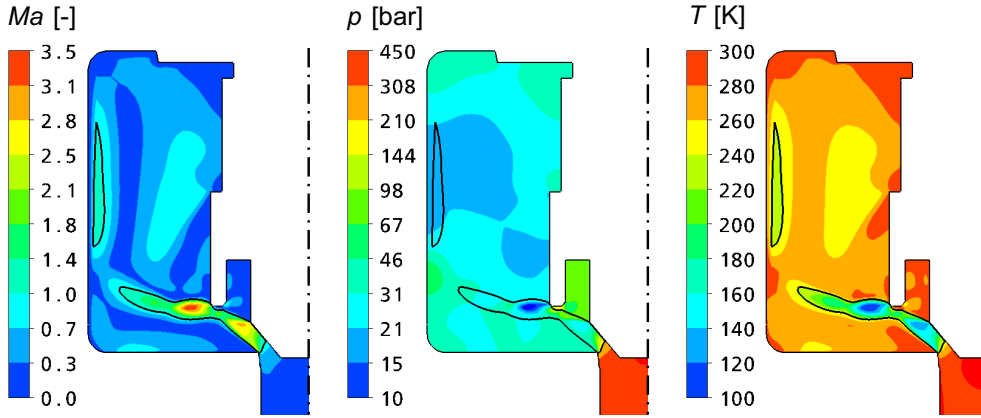


Figure 5.11. Contour plots of Mach number, pressure and temperature of left part of symmetry plane of simulation for nitrogen, $p_{inlet} = 452.8$ bar and $T_{inlet} = 306$ K at $h/d_0 = 0.22$. The black line in all three figures represents the sonic flow line at which $Ma = 1$. The pressure contour plot is logarithmic.

Effect of condensation

In the real-gas property tables the minimum temperature is 100 K. In the flow this artificial temperature limit is only reached in supersonic flow areas with Mach numbers higher than 3.4. An additional simulation is carried out with the build-in Redlich-Kwong EoS for nitrogen of the same valve test with inlet pressure 452.8 bar. Then the real-gas material definition is modeled as a homogeneous binary mixture to allow equilibrium vapor-liquid phase changes. As a result the temperature locally drops further to 62 K with a maximum liquid mass fraction of 0.15 in the supersonic flow area at the valve spindle for this valve test. The effect of condensation reduces the disk force by 3% when the condensation would occur at thermodynamic equilibrium.

From the classical nucleation theory the amount of homogeneous condensation at non-equilibrium conditions can be estimated. The saturation pressure according to the equation of Gomez-Thodos (2.46) for a temperature of 62 K equals $p_{sat} = 0.1$ bar. The saturation ratio S indicates the degree of supersaturation (Hinds, 1999) [26]

$$S = p/p_{sat} \quad (5.4)$$

that equals $S = 50$ with 5 bar on average in the supersonic flow area. The residence time of the fluid in the supersonic flow area with length 3 mm and average velocity 650 m/s is 4.6×10^{-6} s. It is not very likely that homogeneous condensation will be achieved. An example of binary condensation in supersonic nozzle experiments can be found in Wyslouzil (2000) [70].

Transient effects

To verify that the average force from a steady flow simulation is accurate a transient simulation is performed for the case which showed largest fluctuations in a steady

flow simulation ($p_{inlet} = 452.8$ bar and $h/d_0 = 0.22$). In the transient simulation the disk force acting on the part with the lifting-aid fluctuates up to 50% around its average value. The other parts of the spindle wall perpendicular to the valve spindle axis fluctuate around 20% around their average value. Nevertheless, the values averaged from the quasi steady-state simulation do not differ more than 1.4% from the averaged values of the transient one.

The characteristic frequencies of the oscillations are deduced from a discrete FFT transformation, in which the lowest achievable frequency is around 1 kHz. Alternatively, the frequencies can also be graphically determined from a plot in the time domain. Two clear resonance frequencies at 24 and 42 kHz are found. With the local speed of sound characteristic length scales of 8.5 mm and 15 mm are derived which is approximately similar to the average space of 11 mm between the spindle and the housing. Fluctuating pressure waves between the inlet and valve spindle and outlet and valve spindle could not be accurately detected, because the simulation time of 3 ms was not high enough.

It is noted that only measurement points with constant disk lifts have been chosen for validation, so that acceleration forces are insignificant at these points. However, in a valve opening characteristic large acceleration forces are present. In chapter 6 the effect of these forces on the valve characteristic are investigated for incompressible flow in transient simulations with moving meshes. From the experiments no effects of friction forces on the valve spindle during valve relief have been observed, so this effect will not be numerically investigated.

Variation of computational domain

As mentioned before, the size and shape of the computational domain downstream of the safety valve should not influence the operating characteristic, because at the exit the flow is completely choked. Also a mesh refinement or the modeling of the small gap that connects to the spring housing should not change the steady-state solution of the internal flow. Therefore, simulations are carried out with a different mesh size and shapes of the computational domain, where the size of the outlet boundary is related to the outlet diameter D of the safety valve:

- Basic safety valve geometry with outlet diameter D without any additional enlargement with 1.8 million nodes.
- Refined mesh of the same basic safety valve geometry with 3.7 million nodes.
- Rectangular cylinder attached to the outlet with length $10D$ and diameter $5D$.
- Conical transition piece as constructed in the test facility with approximately $16D$ outlet diameter.
- Attachment of a flat cylinder at the small gap with height 1 mm to model the space at the rear side of the spindle in the spring housing.

The listed different computational domains result in a variation of the mass flow rate of 0.4%, valve disk force of 2.2% and pressure in the spring housing of 3.6% compared to the basic safety valve geometry. This means that the numerical solution has a small

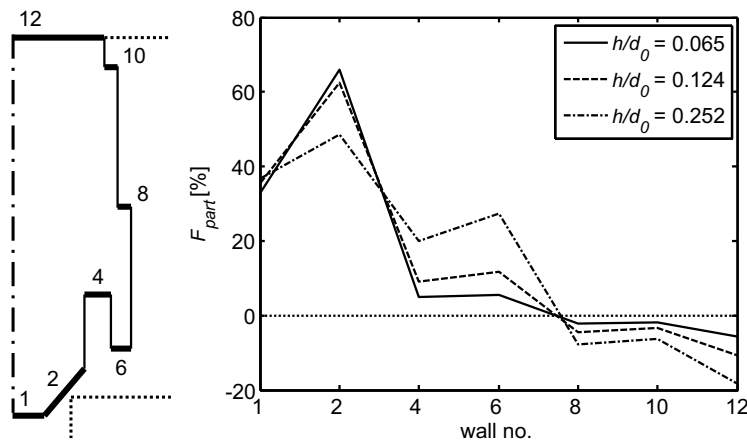


Figure 5.12. Relative wall part contribution to total disk force versus dimensionless disk lift at $p_{inlet} = 73.3, 79.9$ and 95.1 bar and $T_{inlet} = 293, 281,$ and 274 K.

sensitivity to the shape and density of the numerical grid compared to the deviations found in the simulations with the basic safety valve geometry.

Flow distributions around spindle

Next, attention is paid to the flow distributions around the valve spindle that contribute to the valve disk force. The left part of figure 5.12 presents the individual parts of the spindle wall facing the flow. The parts perpendicular to the valve axis induce a net side force to the spindle, but the friction part of the flow force is too small to significantly account for the axial flow force. Therefore, the right part of figure 5.12 shows the relative force contribution of all perpendicular oriented faces and the oblique face of the cone to the axial net disk force of 100%. The three lines refer to the dimensionless disk lift of the valve relief test runs at corresponding operating pressures between 73-95 bar.

For all three disk lifts the force part of the truncated part of the cone (wall number 1) remains at approximately 35%. At the side of the cone this contribution drops 15% during opening. The lifting-aid is of relative small importance at the smallest disk lift whereas at the highest disk lift the contribution increases to 20%. At higher disk lifts the influence of the backpressure becomes also apparent with an increase of 30% over the sum of wall parts 8, 10 and 12. So during valve opening the lifting-aid is initially unimportant and the pressure distribution strongly depends on the disk lift.

Figure 5.13 presents pressure distributions for the two inlet pressures. The measurement at an operating pressure of 80 bar at 0.992 mm disk lift is compared with an upscaled numerical calculation of five times this pressure with the same numerical grid. In order to compare both pressure distributions a dimensionless pressure p/p_{inlet} is defined where for visibility the ranges are adapted from 0.01 to 0.1. So below the cone towards the inlet the dimensionless pressure is unity.

Basically the dimensionless pressure distributions are similar. However, there are

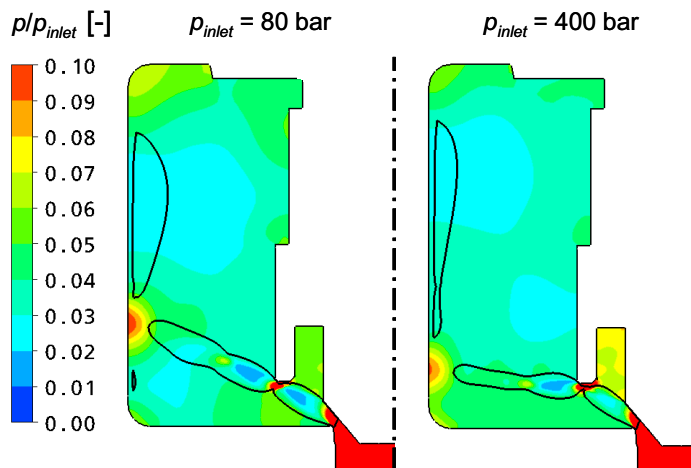


Figure 5.13. Contour plots of dimensionless pressure p/p_{inlet} in symmetry plane with respect to inlet pressure at $h/d_0 = 0.22$. The black line represents the sonic flow line at which $Ma = 1$.

two remarkable differences. First, the black sonic flow line shows that the direction of the flow after passing the lifting-aid is deflected more in the 400 bar solution than in the 80 bar solution. The reason is that the flow differently impinges on the edges of the lifting-aid. Second, the dimensionless pressure at the bottom of the cavity increases from 0.06 to 0.08. Also the size of the bubble with dimensionless pressure above 0.1 at the tip of the lifting-aid is larger for the 400 bar case.

The direction of the flow in and around the cavity can be visualized with the help of vector plots. Figure 5.14 presents these plots of the flow for the same two simulations. In the 400 bar plot right two vortices can be distinguished which have comparable tangential velocities. The lower vortex circulates clockwise at the inner side of the cavity where the upper vortex rotates anti-clockwise with its core closer to the outer side of the cavity wall. In the 80 bar situation left the locations of the center of the vortex and the vortex strength is different, because the lower vortex core is located adjacent to the inner oblique wall of the cavity tip whereas the velocity of the upper vortex are low. In fact, the upper vortex is hardly present with, in addition, higher velocities in the main flow with the same velocity scale for both vector plots.

A force contribution of these simulations analogous to the previous comparison is given in figure 5.15. From this figure the oblique wall of the cone, the bottom and the tip of the lifting-aid show a change of the force contribution. Moreover, the lifting-aid compensates for the lower force contribution of the cone. The local changes of the flow field around the lifting-aid do not affect the backpressure at the three highest wall numbers.

Finally, the pressure distributions on the wall itself in the symmetry plane for the inlet pressures 80 and 400 bar are given in figure 5.16. The difference in dimensionless pressure is also seen at the bottom of the cavity but especially at the tip of the lifting-

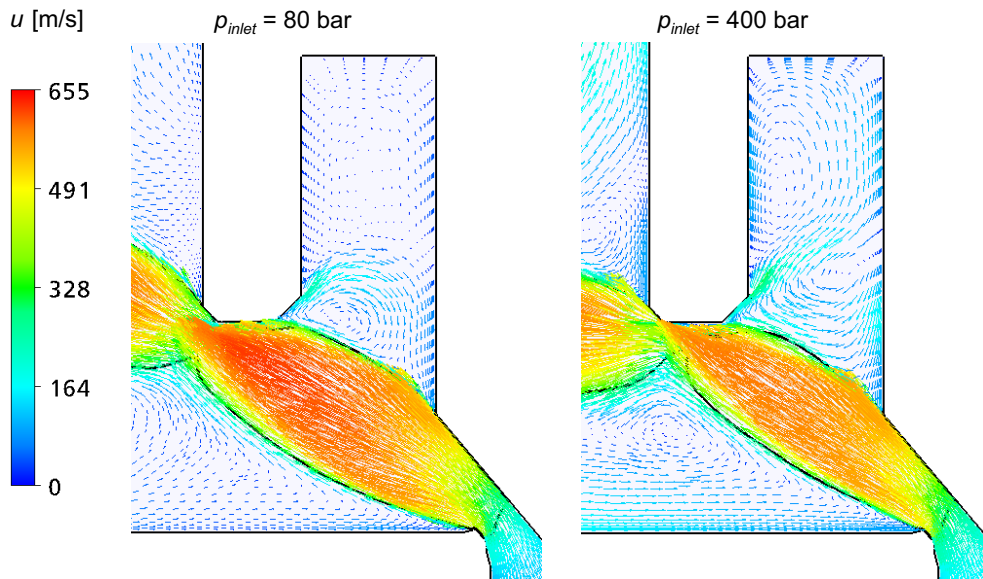


Figure 5.14. Vector plots of lifting-aid of spindle at symmetry plane with respect to inlet pressure at $h/d_0 = 0.22$. The black line represents the sonic flow line at which $Ma = 1$.

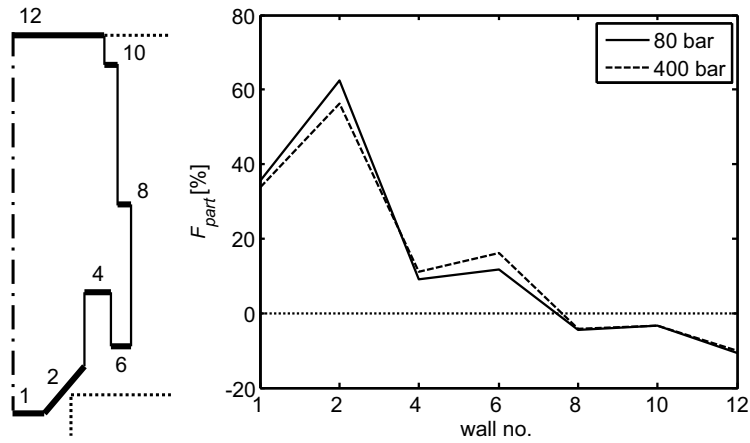


Figure 5.15. Relative wall part contribution to total disk force versus inlet pressure 80 and 400 bar at $h/d_0 = 0.22$.

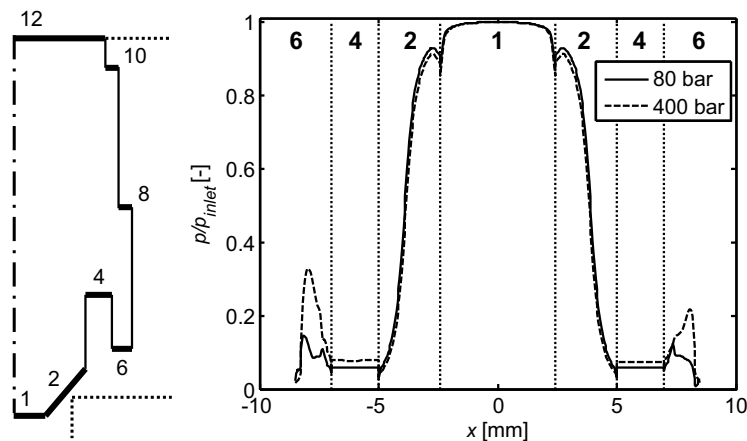


Figure 5.16. Dimensionless pressure distribution of disk wall parts versus inlet pressure at $h/d_0 = 0.22$.

aid. The asymmetry of the flow results in a higher dimensionless pressure on the left side of the symmetry plane than on the right side, where the flow is directed to the outlet. This indicates that at higher inlet pressures the shape of the valve housing, in which the flow expands, has a larger effect on the static pressure at the tip of the lifting-aid.

Effects of mechanical wear

During a valve test the valve seat and spindle are exposed to a high-speed dynamic flow with large adverse pressure gradients. Also during opening partial valve chatter is observed, that mainly occurs during the first relief test of the valve. Prior to and after a valve test series the geometry of the valve seat and valve spindle are measured on a 3D-coordinate machine of Zeiss with an inaccuracy of $0.9 \mu\text{m}$. This data is converted and compared with the geometry in the construction drawing of the safety valve as shown in figure 5.17.

The comparison shows that the sharp edges of the valve seat and the inner edge of the tip of the lifting-aid are rounded due to hammering of the spindle on the seat and excessive wear. Due to reduced chatter after the first relief test it appears that the rounded edges stabilize the flow impinging on the tip of the valve spindle. Balwin (1986) [8] states that the flow interaction over a cavity is a dynamic phenomenon that depends on the edges of the cavity. It is stated that flow induced oscillations by alternating streamlines can be avoided when the streamline reattachment is stabilized when the flow impinges with a sufficient large angle on a chamfered edge of the cavity (figure 5.18). This dynamical phenomenon probably causes the observed valve chatter which can be reduced in an adapted geometry.

Alternatively, the clearance of the valve spindle in the guide box of the safety valve allowing the spindle to marginally move could also induce valve vibration. However,

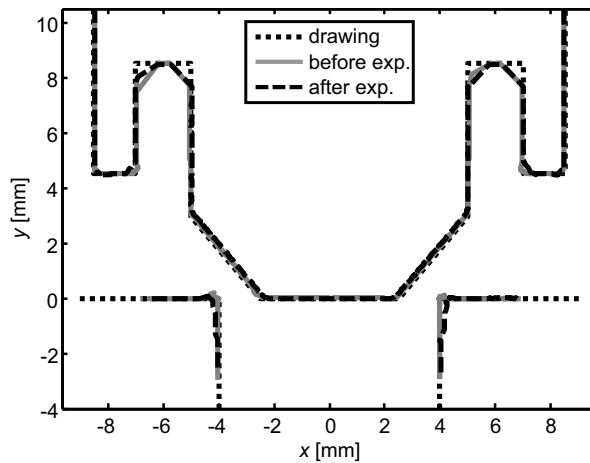


Figure 5.17. Seat and spindle geometry of safety valve as specified in the construction drawing, measured prior to the valve test series with nitrogen at $p_{set} = 62$ bar and after three valve relief tests. Due to mechanical limitations only the sharp inner edges of the bottom of the cavity are not correctly measured.

it is always observed that in the first valve relief experiment the chatter is far more intense than in further valve tests with the same mounted test valve. Then the clearance of the moving spindle is still the same indicating that only a geometry change caused by mechanical wear can account for a different valve characteristic. Besides the nitrogen experiments, in the experiments with water chatter was always observed in the first valve relief test with substantially larger rounding of the corners caused by excessive wear and hammering of the spindle on the valve seat. Chapter 6 focuses on this dynamic flow phenomenon.

In summary, the re-evaluation of the low-pressure safety valve measurement agrees well with the CFD computation. Also all other mass flow rates of high-pressure gas flows agree well within 3.6%. However, in the comparison between the numerical and experimental results in the bottom right graph of figure 5.9 larger deviations occur for the flow forces, with 12% on average. The deviation of the disk force becomes only slightly smaller at larger disk lifts. Since this deviation is relatively constant it is not probable that the error reduces to zero when the valve is completely closed, where the solution is accurately known.

In order to exclude numerical errors that could cause these deviations sensitivity tests have been carried out. As a result the geometry of the computational domain, the mesh density, transient flow effects as well as condensation effects weakly affect the flow pattern. In contrast, the disk lift and the actual operating pressure do affect the pressure distribution. Also large sensitivities of small geometry changes due to mechanical wear that influences the valve characteristic have been experimentally observed.

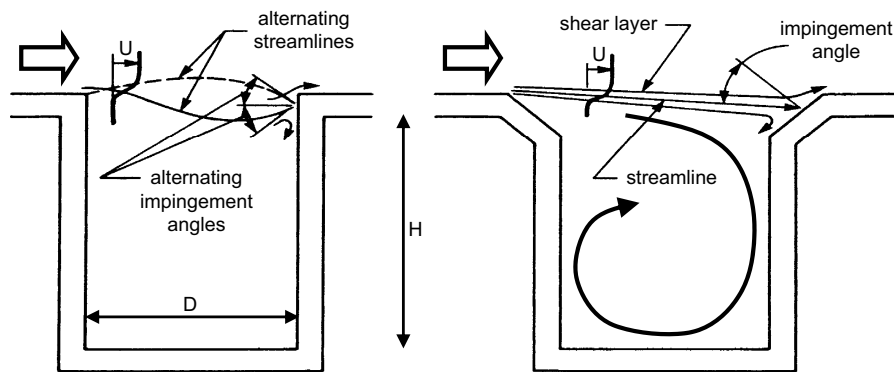


Figure 5.18. Flow interaction over a cavity (Baldwin, 1986) [8].

In conclusion, the numerical analysis has not shown that the deviations in the flow force can be compensated by extensions of the computational domain or discretization errors. Therefore, it is more probable that the indirect measurement of the flow force with the spring deflection and the operating pressure when the valve actually starts to open involves inaccuracies. This topic is further discussed in chapter 7.

5.3 Safety valve flow with real-gas effects

In the preceding section, the numerical method with real-gas effects has been validated for safety valve flows with nitrogen in the pressure region from 73 to 453 bar at ambient temperature conditions. This section presents calculations of this flow outside this region to investigate the influence of real-gas effects on the valve characteristics.

In the experiments and the simulations in subsection 5.2.3 no significant dependency of the discharge coefficient and a weak dependency of the dimensionless flow force on pressure have been found in the investigated pressure region at ambient temperature conditions. The numerical method is developed for a larger pressure and temperature region. Therefore, the influence of real-gas effects on the valve characteristics outside the experimentally possible validation range can be studied. It is chosen to use the stationary point of the safety valve experiment with inlet pressure 79.9 bar, inlet temperature 281 K, and approximately nominal dimensionless disk lift 0.124 as reference measurement. From this reference point numerical calculations are carried out with temperatures closer to the critical temperature and with lower and higher pressures.

In section 2.7 it is discussed that nozzle flows at the minimum inlet temperature of 150 K and inlet pressures from 1000 bar onwards can partially condense in the nozzle throat, because at this location the temperature becomes below the critical temperature of 126.2 K. Consequently, a higher minimal inlet temperature of 175 K is chosen to avoid possible condensation in the nozzle throat, where the flow is critical.

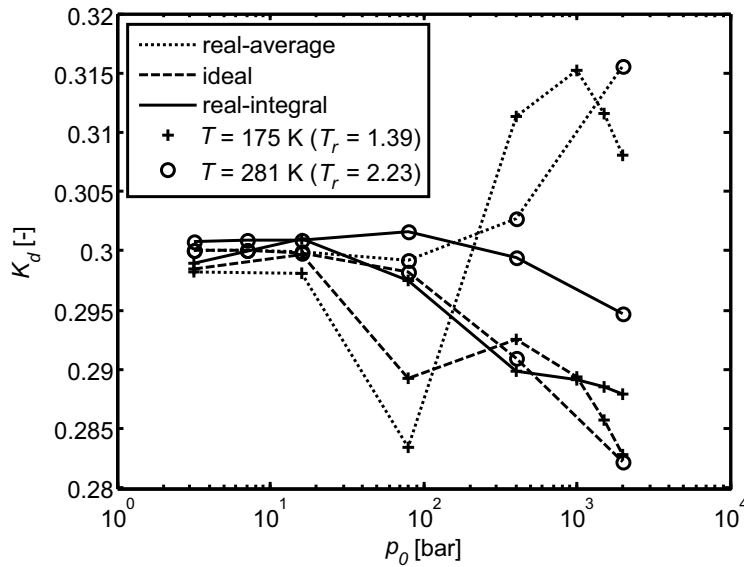


Figure 5.19. Discharge coefficient derived from three valve sizing methods versus pressure and temperature of a safety valve flow at $h/d_0 = 0.124$ with nitrogen.

In the simulations with the safety valve flow the inlet pressure is varied by a factor five to generate the list 3.2, 16, 79.9, 400 and 2000 bar with a few points at other pressures and temperatures.

From the numerical simulations with the same 3D mesh at inlet pressures and temperatures outside the validated domain the mass flow rates and flow forces are computed. The discharge coefficient is calculated by comparing the computed mass flow rate with the one according to each different nozzle method, *ideal*, *real-average*, and *real-integral* (sections 2.1 and 2.6) defining the dimensionless flow coefficient. Figure 5.19 shows the results from this extension to operating conditions outside the validated domain.

For pressures lower or equal to 16 bar, which corresponds to a reduced pressure of 0.47, the discharge coefficient is almost insensitive to the inlet pressure, temperature and the nozzle method used. Above this pressure the *real-integral* method at the reference temperature of 281 K leads to deviations in discharge coefficient of less than 2% for the whole pressure range. The other two methods at the same high temperature show opposite deviations up to +5% and -6% compared to the reference measurement.

The following conclusions can be stated:

- The *real-integral*, *real-average* and *ideal* valve sizing method give the same deviations of the discharge coefficient in the whole application range with acceptable deviations within 6%.
- The *ideal* valve sizing method deviates less than 4% from the most complicated

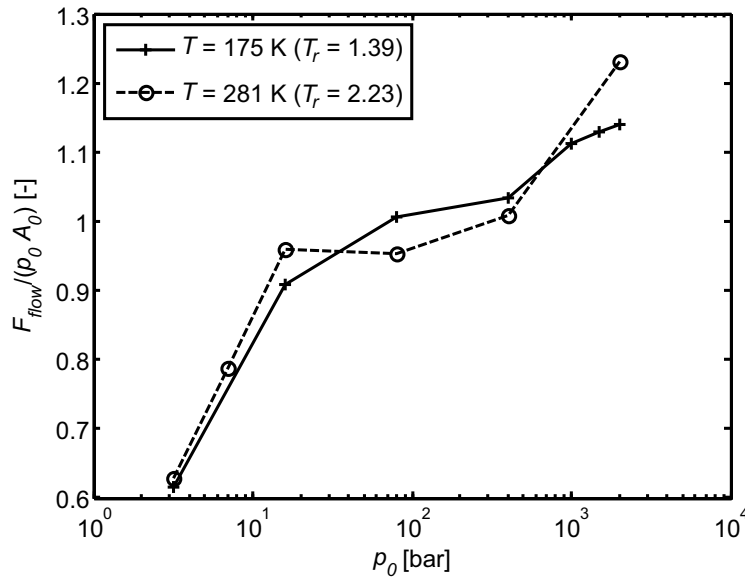


Figure 5.20. Dimensionless flow force versus pressure and temperature of a safety valve flow at $h/d_0 = 0.124$ with nitrogen.

real-integral method.

- Since deviations in the discharge coefficient are sufficiently small it can be assumed constant for this safety valve geometry and this disk lift.
- The simplest currently used *ideal* method is sufficient for safety valve sizing.

From the same numerical simulations the flow force is calculated and made dimensionless by the actual inlet pressure and the seat area that is shown in figure 5.20. The dimensionless force has approximately a constant value for inlet pressures between 16 and 400 bar. At lower pressures the efficiency of the momentum transfer from the flow to the spindle generating the force reduces up to 34%. At higher pressures the fluid is dense resulting in a compressibility factor larger than unity that increases the dimensionless force up to 28%. The dimensionless force is within numerical accuracy independent of pressure.

From figure 5.9 it can be deduced that at the nominal dimensionless disk lift $h/d_0 = 0.125$ of this valve the dimensionless force is approximately 90% of the force when the valve is closed. Also the nominal disk lift should be reached at 10% overpressure. This means that in valve operation the resulting force is approximately equal to the initial force and that the valve is sensitive to small changes of the valve disk force. The force differences found in the extension to pressures and temperatures outside the validated domain are three times larger than the 10% ranges found in the reference point at normal operation, so the operating characteristics are severely affected.

Chapter 6

Dynamic flow simulations

In the preceding chapter, the numerical method for liquid flows has been validated in the pressure region from 64 to 450 bar with an extension accounting for cavitation for steady flows. In this chapter the operating characteristics of a safety valve with water is investigated by extending the numerical method with moving meshes, so that the influence of valve dynamics on steady flow performance can be evaluated.

To gain more insight into valve flow dynamics as discussed in the literature overview in section 1.2 this section focuses on the inclusion of fluid-structure interaction (FSI) in the numerical method of a flow through a safety valve. Then the opening characteristic of a high-pressure safety valve and possible valve instabilities can be distinguished, which may not become apparent in a steady flow approach as presented in chapter 3. With this extension of the numerical model the design of a safety valve can be evaluated and improved to avoid these instabilities during valve operation as much as possible.

In simulations with a single moving grid in each iteration the positions of the mesh nodes are adjusted to the new geometry while preserving the mesh quality parameters orthogonality, expansion and aspect ratio as much as possible. In this process the mesh topology remains the same, because no nodes can be added or connections can be changed. Simulations with a single deforming grid is common practice for small mesh deformations. Multiple grids are necessary in large mesh deformations where some grid cells of the computational domain are stretched too much so that the mesh quality becomes poor resulting in large discretization errors or failure of the numerical solver.

In the case of a high-pressure safety valve the deformation of the grid will not be only large, but also the geometry at the smallest cross-section is complex so that multiple grids are necessary. Furthermore, it is desired to model the valve opening starting from a closed position, which needs special attention to the grid quality as well. The second challenge is to minimize discretization errors that occur in the transfer of the solution variables between two grids with different topology. In order to reduce unnecessary geometrical complexity and to limit calculation time the research is primarily restricted to axisymmetric flow simulations and incompressible fluids.

From the literature overview in section 1.2 CFD computations with multiple mov-

ing meshes for large movements with the inclusion of FSI has not been intensively studied yet with the exception of the research by Bürk (2006) [14], who carried out CFD simulations of a pneumatic valve with critical gas flow with ANSYS CFX.

When a closed safety valve with seat area A_0 is pressurized at a certain set pressure p_{set} that the valve just starts to open, the spring force F_{spring} and gravity force $F_{gravity}$ are in equilibrium with the flow force F_{flow} that is the set pressure multiplied with the seat area. In valve operation friction forces occur at the moment when the valve opens and due to misalignment of the spindle pressing on the guide box. The first friction source is ignored because the valve is simulated with a sufficiently small opening necessary for numerical stability. The second friction source is not possible to simulate because the valve model is axisymmetric and the friction can only occur when the valve spindle is misaligned. Figure 6.1 shows the forces that act upon a moving spindle with a disk of a safety valve.

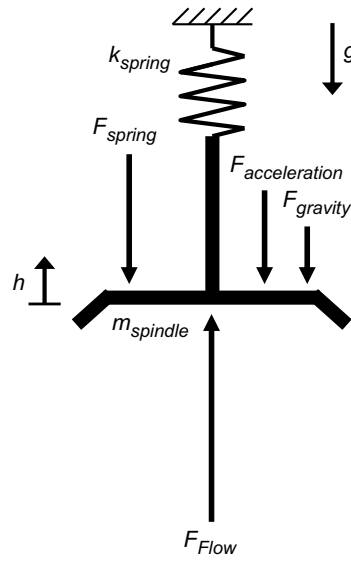


Figure 6.1. Force balance of moving valve spindle with disk.

The initial displacement h_0 of the compression spring with stiffness k_{spring} equals

$$h_0 = \frac{p_{set} A_0}{k_{spring}}. \quad (6.1)$$

The acceleration \ddot{h} of the spindle with disk during valve movement is given by Newton's law as

$$\ddot{h} = \frac{F_{flow} - k_{spring}(h + h_0) - m_{spindle}g}{m_{spindle}}, \quad (6.2)$$

with $m_{spindle}$ the equivalent mass of the moving parts of the valve and g the gravitational constant when the valve is operated in vertical orientation.

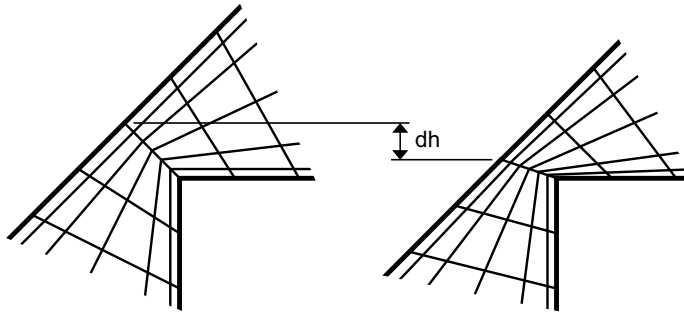


Figure 6.2. Mesh deformation around safety valve seat of a grid with reduced mesh density.

In the numerical method to be extended for a moving valve spindle this spring-mass system is modeled without friction forces and without damping. Besides the moving spindle that deforms the computational domain directly related to the flow, the thick steel walls of the high-pressure safety walls are assumed to deform little and are considered to behave as rigid walls.

6.1 Numerical approach

In this subsection first the discretization of the computational domain is discussed. Then the solution strategy to compute with multiple meshes is presented.

Discretization

The axisymmetric safety valve geometry is modeled as a 2° slice similar to figure 3.14. The valve spindle consists of the truncated cone with an angle of 40° that presses on the sharp edge of the valve seat. Figure 6.2 illustrates a small mesh deformation dh , where the mesh cells at this edge experience nearly only shear so that the mesh orthogonality becomes poor immediately. This effect becomes even larger for more dense meshes with at least 10 cells in the smallest cross-section and at very small disk lifts in the order of the minimum required boundary layer thickness. The numerical method can only compute connected computational domains so that a closed valve has to be approached with a valve with small disk lift, which is chosen to be 0.01 mm. This is smaller than the smallest detectable disk lift in the experiments.

In order to cover the whole disk lift range of 3 mm, 17 grids are generated, which are structured in the smallest cross-section with the largest flow gradients and unstructured after the smallest cross-section. Figure 6.3 shows an example of a grid at $h = 0.89$ mm. From the smallest disk lift of 0.01 mm each grid is predefined with a factor 1.5 larger disk lift compared to the previous one resulting in the 17 predefined meshes in total. The smallest nodal distance of the mesh with disk lift $h = 0.01$ mm is 0.001 mm which increases up to 0.025 mm for the larger meshes with 42000 nodes on average.

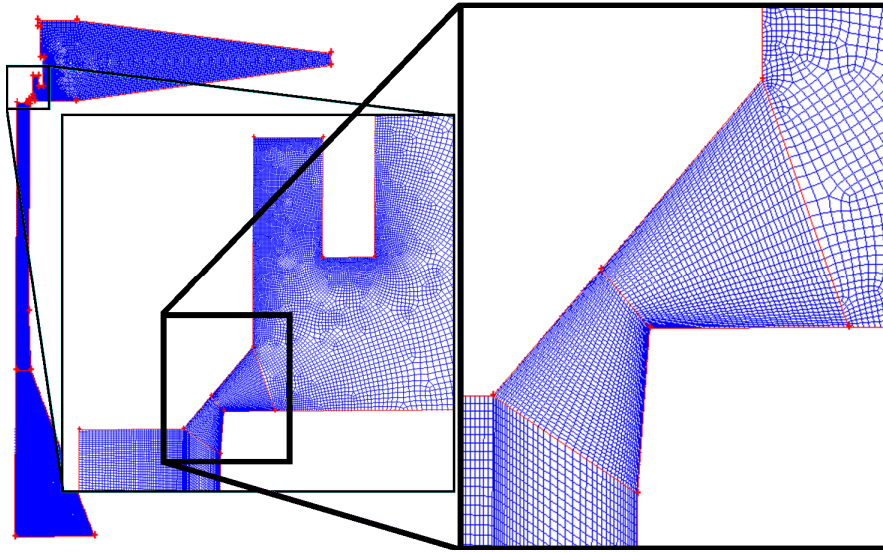


Figure 6.3. Front surface of axisymmetric computational domain of safety valve for $h = 0.89$ mm.

Solution strategy

The schematic procedure of a simulation with multiple meshes is shown in figure 6.4. With the help of code in the programming language Perl the series of simulations with different predefined meshes, the communication of the variables necessary for the calculation of the valve displacement and the export of the solution variables for evaluation in Matlab are controlled. A series of simulations with multiple moving meshes starts with the definition file with basic solver parameters and one predefined undeformed mesh that is closest or equal to the valve disk displacement defined in the definition file. The first simulation is initialized with the solution of a steady flow simulation at the same initial disk lift with velocity zero. When during a simulation a second mesh is loaded the additional parameters such as the spindle velocity and flow force are updated from the previous simulation run to the CFX Command Language (CCL).

Then as part of each iteration time step n in a first user-defined function written in the programming language Fortran first the mesh movement for the next time step is evaluated, where the acceleration of the disk \ddot{h}^{n+1} is a function of the valve displacement h^n and flow force F_{flow}^n

$$\ddot{h}^{n+1} = \frac{F_{flow}^n - k_{spring}(h^n + h_0) - m_{spindle}g}{m_{spindle}}. \quad (6.3)$$

Then with the acceleration of the disk, time step size dt and the velocity of the current

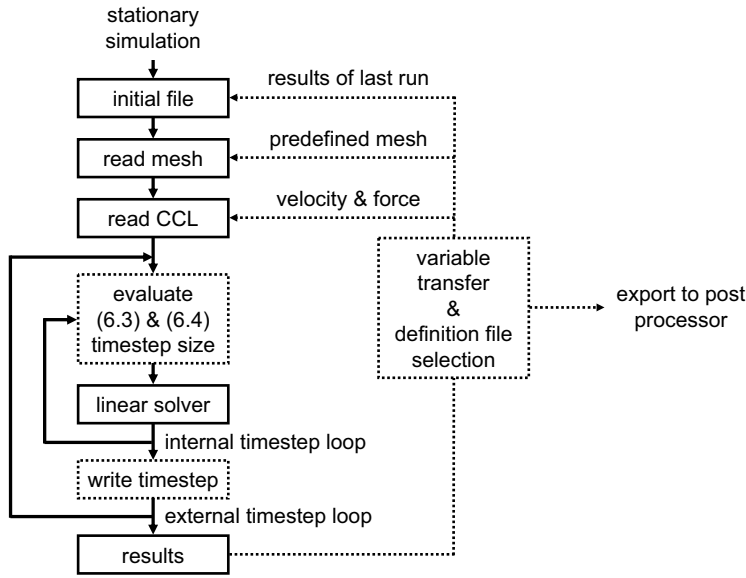


Figure 6.4. Solution scheme of simulation with multiple meshes.

time step \dot{h}^n the displacement of the disk h^{n+1} for the next time step becomes

$$h^{n+1} = h^n + \dot{h}^n dt + \frac{1}{2} \ddot{h}^{n+1} dt^2. \quad (6.4)$$

After the mesh movement is updated in each external time step loop in the same Fortran routine the simulation time step size is evaluated. In order to minimize errors in the interpolation of the numerical solution when the mesh displacement of the current mesh exceeds the displacement of a predefined mesh it is desired to equal the valve disk lift of the current deformed mesh at the end of a single simulation run with the predefined mesh of the next run as much as possible. In the routine the time step size is changed with 1% at maximum between a minimum and maximum value to ensure that after a certain expected elapsed simulation time the difference of the valve disk lift between the two meshes is within a tolerance of 1 nm. Only then interpolation of the solution variables stored at the nodes and the disk force and velocity occurs with low errors. In the second Fortran routine only the updated step size is adjusted for the next external time step loop.

In the internal time step loop the conservation equations of mass, momentum and turbulence are solved in linear equation sets of transport equations as described in section 3.1.2. The temporal discretization is according to a second-order accurate linear multistep method for the mass and momentum equations while a first-order backward Euler scheme is applied for the turbulence equations.

Previous simulations have shown that differences of the flow force between compressible and incompressible water computations are small compared to the flow force fluctuations during a transient simulation, so the influence of moving pressure waves

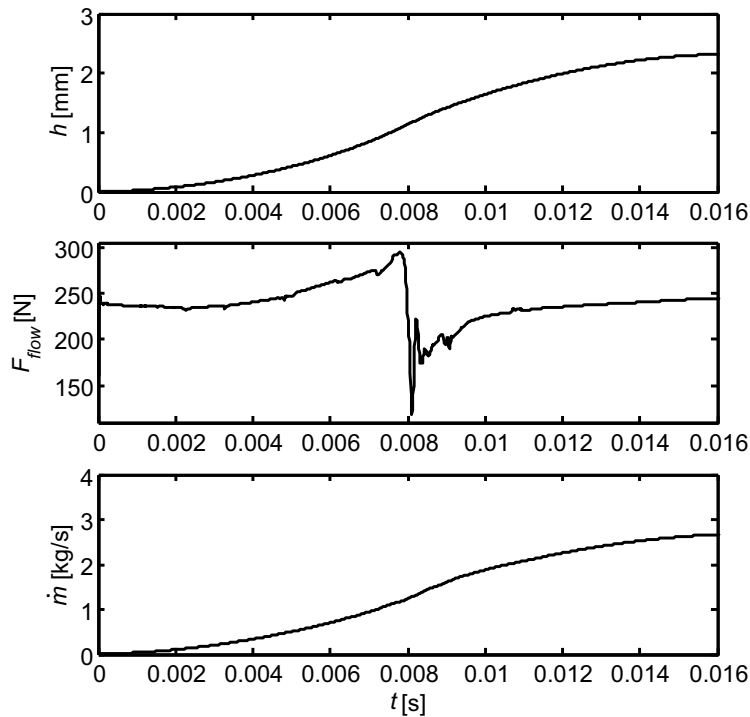


Figure 6.5. Disk lift, flow force and mass flow rate versus time of a FSI simulation with liquid water.

on the flow force of the water computations is small. As a result the incompressible approximation of water to study valve dynamics is sufficient.

6.2 Results

Figure 6.5 shows the results of transient simulations with multiple meshes of the axisymmetric safety valve with water starting with the predefined mesh with disk lift $h = 0.01$ mm, initial spring force based on set pressure $p_{set} = 40$ bar and spring stiffness $k_{spring} = 25328$ N/m, a constant 10% overpressure at the inlet $p_{exp} = 44$ bar, outlet pressure 1 bar, equivalent mass of the moving components $m_{disk} = 0.7662$ kg and simulation time step size $dt = 2 \times 10^{-5}$ s. The valve opens to close to its maximum disk lift of 3 mm.

At time $t = 0$ s the mass flow rate equals $\dot{m} = 0.013$ kg/s, which is comparable to a leaking safety valve after a few valve test series. The oscillations of the flow force during the first few iterations of a new simulation with a predefined mesh are mostly small. Especially for incompressible flows this variable is sensitive to small interpolation errors and inaccuracies that occur during initialization of the simulation.

These oscillations, if present, reduce within 10 time steps to a value that only gradually changes during the rest of the simulation run. Therefore, they do not affect the total behavior of the flow force.

In the first 3 ms the flow force first remains constant although the disk lift increases to 0.2 mm. In the first part of the valve opening the acceleration forces dominate the valve movement. At $t = 8$ ms and disk lift $h = 1.13$ mm the flow force drops relatively fast to half of its maximum value in only 0.3 ms. This results in decelerating of the valve spindle and in a short fast increase of the disk lift and the corresponding mass flow rate.

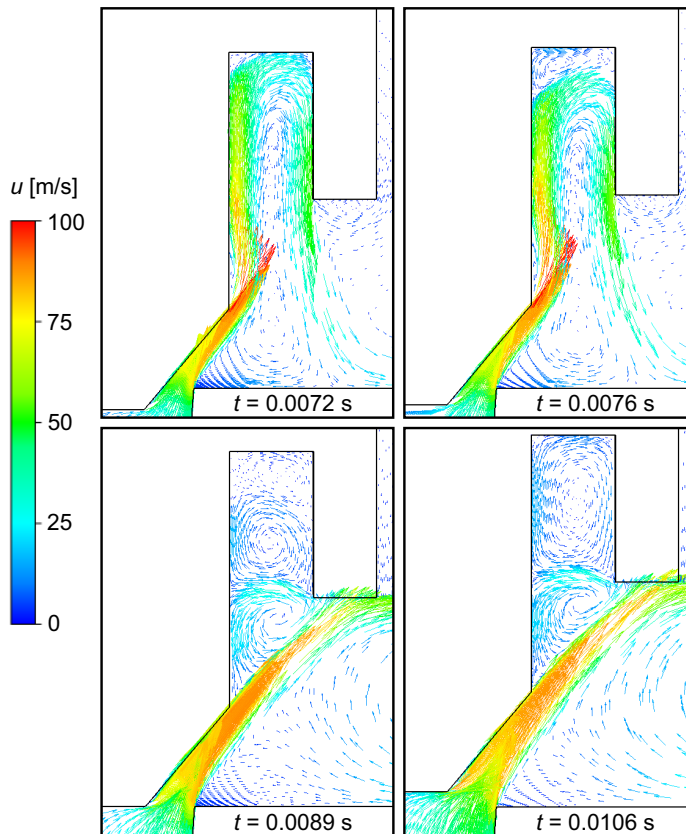


Figure 6.6. Vector plots of velocity field of water flow at four different simulation times at $p_{exp} = 44$ bar.

The change in direction of the flow in this time period is visualized in four vector plots of the velocity field around the lifting-aid in figure 6.6. It can be seen that at $t = 7.2$ ms and $h = 0.89$ mm the flow remains attached to the valve cone and directly impinges on the bottom of the cavity. Then at $t = 7.6$ ms and $h = 1$ mm the flow

starts to detach from the calve cone and the circulating bulk flow moves away from the bottom of the cavity. Hereafter at $t = 8.9$ ms and $h = 1.39$ mm the flow has completely detached and impinges on the tip of the lifting-aid with tree vortices in the cavity. Finally at $t = 10.6$ ms and $h = 1.75$ mm, two vortices remain in the cavity and the flow has stabilized again.

After the force jump the disk lift almost reaches the mechanical stop at 3 mm, but the flow force recovers only slowly to the initial value. At a larger elapsed time up to 0.1 s no further force discontinuities have been observed. Figure 6.7 shows the contributions of the wall parts of the spindle that significantly contribute to the valve force. Only the wall parts with values larger than 1 N are plotted.

This figure clearly shows the fast switch of the contribution of the individual

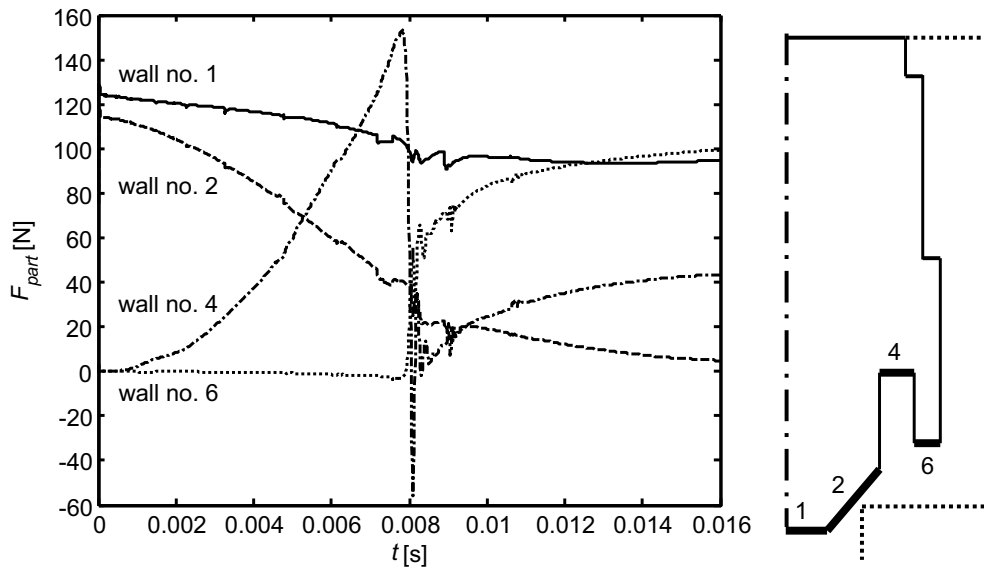


Figure 6.7. Contribution of the significant wall disk parts to total flow force versus time of a FSI simulation with liquid water.

wall parts as a function of time. At $t = 0$ s only the truncated cone (wall no. 1 and 2) contributes to the flow force. Directly after opening the cavity of the lifting-aid (wall no. 4) starts compensating for the reducing forces on the truncated cone. At simulation time $t = 8$ ms the tip of the cavity (wall no. 6) only partly recovers the collapse of the force at the lifting-aid.

In order to determine the influence of the flow dynamics on the valve characteristic, the previously described transient simulation run with constant operating pressure $p_{exp} = 44$ bar is compared with steady-state solutions of simulations at times when the dynamic simulation changes to a new predefined mesh. Then, the disk lifts of the steady-state simulations are converted to the time domain by solving the valve dynamics equations (6.3) and (6.4) with values of the disk force interpolated between

the steady-state solutions starting at $t = 0$ s, initial velocity $\dot{h} = 0$ m/s and initial spring displacement h_0 that is exactly the same as used in the transient simulation with multiple meshes. For the whole time domain the disk lifts have been calculated the corresponding mass flow rates and flow forces are interpolated.

In figure 6.8 the solutions of both approaches are compared with each other. Up

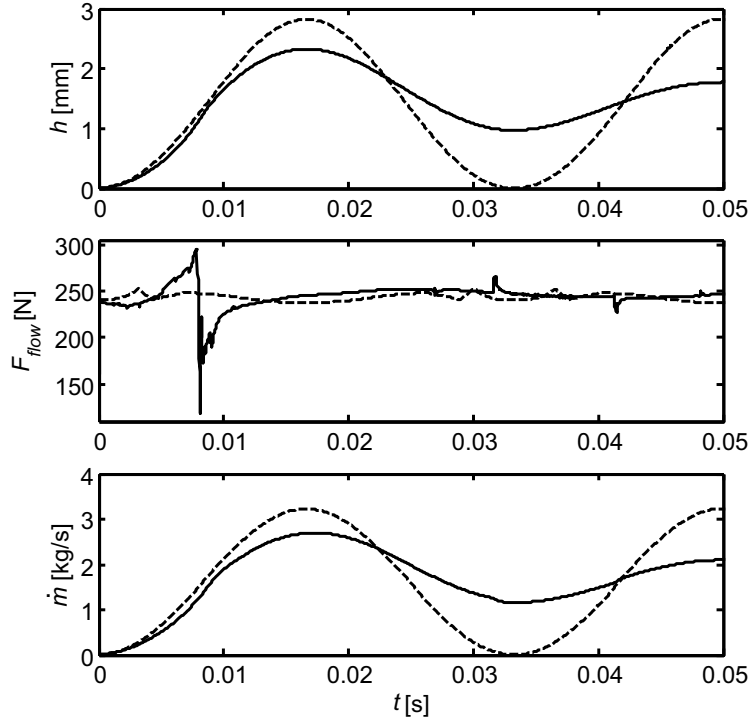


Figure 6.8. Comparison transient simulation results with steady flow approach at $p_{set} = 40$ bar and $p_{exp} = 44$ bar. Legend: solid line: transient, dashed line: steady flow.

to the highest disk lift, the disk lift and the mass flow rate can be well approximated by the steady-state solutions. However, the large rise and collapse of the flow force cannot be distinguished with only steady-state simulations. Fortunately, this hardly influences the mass flow rate and flow force. Furthermore, when the valve closes again the valve movement damps out to a constant value due to viscous and turbulent dissipation, which cannot be reproduced by the steady-state approach. This damping would be even larger when friction effects of the spindle pressing on the guide box are taken into account. In a comparison between the two approaches where the set pressure and overpressure are increased by a factor five the observed differences are similar.

At a valve disk lift of around 1 mm the differences between the steady solution and the transient solution are large. As previously observed in the analysis of compressible flow distributions around the spindle in section 5.2.3 a change in the orientation of

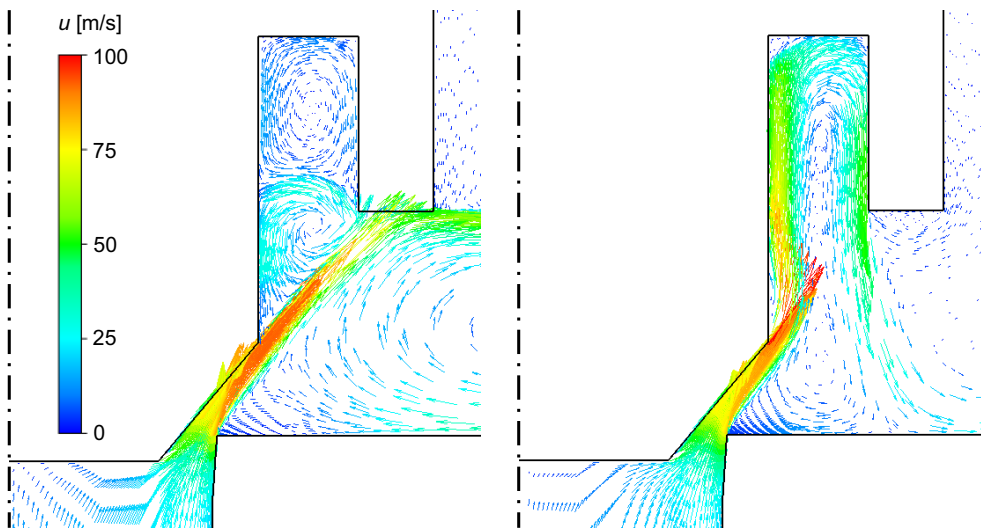


Figure 6.9. Vector plots of stationary (left) and transient (right) velocity field of water flow at $p_{exp} = 44$ bar and $h = 0.89$ mm.

the flow results in a suddenly different distribution of the flow forces acting upon the individual wall parts of the spindle.

The differences in the velocity field of the flow become more apparent when comparing a solution of the steady-state approach with the transient one at the same disk lift $h = 0.89$ mm, which is shown in figure 6.9. In the static simulation in the left figure two clear strong vortices are present and the bulk flow directly impinges on the edge of the lifting-aid. In the right figure, which shows the dynamic simulation results at the same disk lift, the flow remains adjacent to the truncated cone and completely flows into the cavity of the lifting-aid inducing a larger total flow force. It is apparent that in the dynamic approach the flow does not have time to relax so that the redirection of the flow pattern is delayed with a large impact on the flow force. This flow-history effect cannot be distinguished by the static approach.

The inclusion of FSI in incompressible valve flows has led to new insights in valve dynamics that cannot be observed by a steady-state approach. It is emphasized that in the case of incompressible fluids the absence of damping or the ability to absorb pressure waves by the flow poses higher demands on accurate transfer of the solution variables to a new mesh. In addition, the mass flow rate and the disk lift are less affected by large variations of the disk force. However, a redirection of the flow could be induced by traveling pressure waves and can lead to unstable valve operation when occurring close to the eigenfrequency of the valve. This valve chatter has also been observed during valve tests at the high-pressure test facility. Therefore, in valve design sudden changes of the flow force during valve opening should be avoided at all times.

Chapter 7

Discussion

The objective of this study is to analyze the mass flow capacity and opening characteristics of spring-loaded safety valves at operating pressures up to 3600 bar by both numerical simulations and high-pressure valve tests.

Valve sizing methods

Currently, the gas mass flow capacity of a safety valve at any pressure and temperature condition is determined with a standardized valve sizing method. This method is derived from the ideal gas theory and assumes a constant discharge coefficient that is experimentally determined at low pressures. In this study the applicability of this standardized and two alternative valve sizing methods to real-gas flows has been analyzed by means of: CFD computations of nitrogen nozzle and safety valve flow at inlet pressures from 0.1 to 2500 bar and temperatures from 150 to 300 K; experimental data of nitrogen nozzle flow at inlet pressures from 100 to 3500 bar and ambient temperatures; experimental data from safety valve tests with nitrogen at operating pressures up to 600 bar and ambient temperatures.

The two introduced alternative valve sizing methods (*real-average* and *real-integral*) approximate the thermodynamic state changes between the inlet and the choking plane of a critical nozzle flow according to the real-gas theory. From the CFD computations of nozzle flow with nitrogen it is concluded that although the standardized *ideal* valve sizing method is the simplest method since no iterative calculations have to be made and it is based on critical nozzle flow model derived from the ideal gas theory, it deviates only 3% from the most complex *real-integral* valve sizing method.

Safety valve computations have been carried out at higher inlet pressures up to 2000 bar and a lower inlet temperature of 175 K as close as possible to the critical point to remain single phase in the smallest flow cross-section. The discharge coefficient reduces by only 2% in combination with the *real-integral* sizing method and deviates 6% when the dimensionless flow coefficient is calculated with the *ideal* or *real-average* method. Consequently, for this valve geometry the discharge coefficient can be assumed constant and the simplest *ideal* valve sizing method is sufficient. The accuracy of the method is also proven by a comparison with experimental data from nozzle flows at inlet pressures up to 3500 bar.

In conclusion, the nozzle model of the *ideal* valve sizing method sufficiently covers the thermodynamics of the flow, because errors cancel each other, so that the discharge coefficient corrected for frictional losses and redirection of the flow only weakly depends on the thermodynamic state at the inlet of the valve. This means that the current practice of determining the valve discharge capacity by means of valve tests at low inlet pressures between 5 and 7 bar discharging into the atmosphere provides sufficient information for valve sizing at other pressure and temperature conditions. It is noted that this study focused on one valve geometry, but in publication (Schmidt, Peschel and Beune, 2009) [59] computations with another typical high-pressure valve geometry the discharge coefficient with improved accuracy of the equation of state used in the CFD tool is expected to vary within 10%.

According to the principle of corresponding states, this analysis can also be quantitatively applied to other non-polar and weakly polar pure gases or gas mixtures that can be decomposed with the mixing rules and the used equation of state Soave Redlich-Kwong. For polar gases or complicated gas mixtures it is recommended to use a suitable equation of state in combination with the CFD tool to determine the discharge capacity of safety valves when no experimental data is available. For valve sizing by plant designers it is recommended to use the sufficiently accurate standardized *ideal* valve sizing method with properties for the compressibility factor and adiabatic exponent derived from a sufficiently accurate real-gas equation of state when deviations from the ideal gas equation of state become significant.

Analysis of experimental and numerical results for steady valve flow

Valve sizing methods cannot be used to predict the opening characteristics of safety valves. Alternatively, a CFD model or valve tests are necessary to account for 3D flow effects that result in a complex pressure distribution at the valve disk which determines the flow force. The flow force actually determines stable operation of the valve and is, therefore, for a valve manufacturer more important than the mass flow rate as a design parameter for a satisfactory and stable opening characteristic.

In computations of the CFD tool of the investigated safety valve with nitrogen at nominal disk lift and inlet pressures outside the experimental validation range up to 2000 bar the dimensionless flow force continually increases with pressure independent of the inlet temperature within the numerical accuracy. The deviations compared to the reference experiment at 80 bar are -34% at a lower pressure of 3.2 bar and +28% at a higher pressure of 2000 bar. As a result, when stable valve operation is found in accordance with the standards at a certain operating pressure, the opening characteristic differs from valve operation at another set pressure when the spring stiffness is adapted with the same factor as the set pressure ratio.

From the high-pressure safety valve tests conducted at the constructed high-pressure facility with operating pressures up to 600 bar, accurate and reproducible stationary valve flow conditions have been achieved, wherefrom the averaged measurement points show remarkable differences between the valve characteristic conducted with sub-cooled water and gaseous nitrogen both in the pressure range of 64 and 453 bar at ambient temperature. In the valve tests with water the dimensionless flow force based on the actual operating pressure slightly increases to 1.05 at the nominal

disk lift of 1 mm while the experiments with nitrogen show a dimensionless flow force continuously decreasing to 0.88 at nominal disk lift.

The mass flow rates have been accurately determined so that it is possible to relate the small scatter in the measured valve characteristic to specific experimental conditions. In the water tests the dominant experimental uncertainty is a gradual geometry change due to rounding off the edges of the valve seat and spindle caused by excessive mechanical wear. This results in increased discharge capacities up to 10% at the same disk lift for the studied valve type. Also valve chatter in tests after the first blow-off test, if present, reduces or is absent in further blow-off tests of the same valve. In the nitrogen valve tests at high operating pressures large temperature fluctuations in the buffer vessel and the mass flow measurement system cause inaccuracies in the discharge coefficient up to 10%. For both fluids the discharge coefficient and the dimensionless flow force are independent of pressure at the valve inlet in the range between 64 and 453 bar and at ambient temperatures.

In the numerical calculation with the CFD tool for water flows it seems necessary to extend the numerical model with a cavitation model. Simulations with cavitation lead to a significantly better agreement. At low disk lifts and at high pressures the cavitation model needs to be extended to account for thermal and compressibility effects of the vapor phase.

For compressible high-pressure valve flows, the mass flow rates always agree within 3.6%. The flow forces show an approximately constant deviation between 7.8% and 14.7% between experiment and numerical simulation, which are already present at low disk lifts. Analysis of the results shows that this deviation cannot be completely explained by numerical errors, so it is expected that the indirect flow force measurement method with the spring deflection and opening pressure of the test valve is mostly responsible for the deviation. A larger experimental error than previously estimated in the accuracy analysis is possible, because the difference between the set pressure and the actual opening pressure of the investigated safety valve is larger than a priori estimated. This results in a larger pressure range where the valve leaks at non-detectable small disk lift with increasing inlet pressure before the valve actually opens and starts relieving large amounts of fluid. Also frictional effects could play a larger role at high pressures than previously estimated.

For more accurate force measurements it is recommended to decrease the stiffness of the spring as much as possible so that the spring can still be pre-stressed to the force at the desired set pressure, without pressing the windings on each other so that further compression is mechanically blocked by the spring. Then the valve immediately opens and with the force sensor installed stable valve opening at the mechanical stop is ensured. Then the difference between the set pressure and the uncertain opening pressure is minimized. It is noted that it is important to damp the collision of the spindle on the mechanical stop with rubber to avoid excessive peak forces possibly damaging the attached force sensor. Alternatively, it would be better not to install a spring at all and measure at fixed disk lifts directly with the force sensor only. The drawback is that it is more difficult to achieve stable operating conditions during a valve test, because the valve already relieves fluid when the buffer vessel is pressurized.

Dynamic CFD modeling

It is possible to study the opening characteristic of a high-pressure safety valve with incompressible flow in the entire disk lift range with the multimesh FSI algorithm. In the development of this algorithm it is focused on mesh quality and accurate transfer of the solution variables to a new predefined mesh. Especially for incompressible flow it is important to postpone transfer to a new mesh until the disk lift of the deformed mesh differs only 1 nm from the next predefined mesh so that force oscillations, due to discretization errors are minimized.

In the dynamic simulation of an axisymmetric safety valve with water at a set pressure of 40 bar and at 10% overpressure a large rise and huge collapse of the flow force with factor two at approximately nominal disk lift have been observed. A corresponding redirection of the flow hardly affects the mass flow rate and disk lift, but can lead to unstable valve operation when these changes of the flow pattern occur close to the eigenfrequency of the moving parts of the valve.

In a comparison between static and dynamic simulations with incompressible flow a collapse of the flow force can only be seen in the steady-state approach when the amount of steady-state simulations is significantly increased so that the discretization of the coupled valve dynamics is more accurate. That means that flow-history effects should be small so that the flow immediately adapts to changed boundary conditions, which is the case for incompressible flows.

For gases flow-history effects are present resulting in a less strict tolerance of the disk lift difference between two numerical grids, since small interpolation errors are locally damped. However, at high pressures the flow gradients adjacent to the walls are large so that this algorithm is still necessary for accurate calculation. For simulations with (real-) gases it is recommended to reduce the smallest nodal distance of the meshes at lower disk lifts so that converged solutions will be achieved as well. Another future research topic is to model an opening valve with water with a cavitation model, so that the effect of cavitation on the valve dynamics can be investigated.

Possibilities with the CFD tool

This CFD tool can be used for accurate prediction of the discharge coefficient when no measurement data is available or when it is hardly possible to conduct a valve test. It is still unclear whether this tool can quantitatively predict flow forces with similar accuracy. As a result, evaluating valve design should always occur in combination with experimental research.

For safety valve design it is important that the flow force is accurately known as a function of disk lift and varies without large discontinuities caused by redirections of the flow pattern. In static simulations flow pattern changes can be observed, but flow-history effects can only be distinguished by a dynamic approach. That's why in the static approach these redirections of the flow still occur but with smaller amplitudes of the flow force and at slightly different disk lifts than in the dynamic approach. In incompressible flows flow-history effects are smaller than in compressible flows. It is still unclear when dynamic simulations are necessary for different compressible fluids at other circumstances. In future research it is recommended to investigate multimesh FSI simulations for compressible high-pressure valve flows that

comes along with high computational costs and long preparation times compared to the steady-state approach.

Nevertheless, in a static approach of the CFD tool it is possible to study different geometries and see the development of the flow without suddenly emerging separation points causing changed locations of recirculation areas. Actually, from a design point of view it is desired to control these moments to occur outside the mechanically possible disk lift range or at the nominal disk lift in the case of pop-up safety relief valves. Then no unwanted force fluctuations occur during opening and closing of the safety valve when it is most sensitive to elevated backpressures and dynamic flow effects. In other words, the flow gradually changes while opening with separation points and recirculation areas at positions that are insensitive to small changes of the gas or, ideally, to compressibility effects at all. Furthermore, the safety valve can be applied to both gases and liquids with the largest possible pressure range of a single spring.

A safety valve should open to its nominal disk lift at 10% overpressure maximum. The tolerance of the valve spring stiffness and the safety factor of the reduced discharge coefficient used in the standardized valve sizing methods are both 10%. That means that the flow force should be calculated with an accuracy of the order of 1%. This high accuracy demand cannot be achieved with the CFD tool so that the spring stiffness cannot be numerically determined for a safety valve. Therefore, the spring can be dimensioned only in valve experiments and up-scaling to higher pressures than experimentally possible should always be taken with care.

Nevertheless, the strength of the CFD tool is to optimize valve geometries in combination with sensitivity studies to account for small geometry changes (effect of mechanical wear and production tolerances) and real-gas effects to find the cause for valve chatter and to avoid it in improved geometries.

So the CFD tool is suitable to quantitatively predict the mass flow rate, but can only qualitatively predict and show tendencies of the flow force. This means that when a safety valve will be applied at higher pressures than measurable in a test facility, it should always be verified that it certainly reaches its nominal disk lift at 10% overpressure when mounted at the pressurized system of the plant itself. Nevertheless, the simulations of the dimensionless forces at pressures up to 2000 bar of this valve type have shown that the momentum transfer of the flow to the valve disk becomes more efficient resulting in a larger force at nominal disk lift indicating that the net force to open the valve increases with pressure. However, frictional effects can prevent the valve from opening at higher pressures when the overshoot of the net force is small or cause the dimensionless force to decrease too much directly after valve opening.

Bibliography

- [1] AD: 2001, *AD 2000 Merkblatt A2 Sicherheitseinrichtungen gegen Drucküberschreitung – Sicherheitsventile*. Berlin: Beuth Verlag GmbH.
- [2] Alvi, F., J. Ladd, and W. Bower: 2002, ‘Experimental and computational investigation of supersonic impinging jets’. *AIAA journal* **40**(4), 599–609.
- [3] Anderson, J.: 2003, *Modern compressible flow with historical perspective, 3rd edition*. New York: McGraw-Hill.
- [4] ANSYS: 2006, ‘Manual ANSYS CFX, Release 11.0’. Canonsburg.
- [5] API: 2000, *API RP-520:2000 Sizing, selection, and installation of pressure-relieving devices in refineries, Part I sizing and selection*. Washington, DC: 7th ed., American Petroleum Institute.
- [6] ASME: 1998, *Performance Test Code PTC19.3:1974 (R1998) Temperature Measurement*. New York: ASME.
- [7] ASTM: 2008, *ASTM E220 - 07a Standard Test Method for Calibration of Thermocouples By Comparison Techniques*. West Conshohocken: ASTM International.
- [8] Baldwin, R. and H. Simmons: 1986, ‘Flow-Induced Vibration in Safety Relief Valves’. *Journal of Pressure Vessel Technology* **108**, 267–272.
- [9] Bauerfeind, K. and L. Friedel: 2003, ‘Berechnung der dissipationsbehafteten kritischen Düsenströmung realer Gase’. *Forschung im Ingenieurwesen* **67**(6), 227–235.
- [10] Betts, P. and J. Francis: 1997, ‘Pressures beneath the disc of a compensated pressure relief valve for gas/vapour service’. *Proceedings of the Institution of Mechanical Engineers, Part E: Journal of Process Mechanical Engineering* **211**, 285–289.
- [11] Bober, W. and W. Chow: 1990, ‘Nonideal isentropic gas flow through converging-diverging nozzles’. *ASME, Transactions, Journal of Fluids Engineering* **112**, 455–461.

- [12] Botros, K., G. Dunn, and J. Hrycyk: 1998, 'Riser-Relief Valve Dynamic Interactions (Extension to a Previous Model)'. *Journal of Pressure Vessel Technology* **120**, 207–212.
- [13] Bredau, J.: 2000, 'Numerische Strömungsberechnung und experimentelle Strömungsvisualisierung in der Pneumatik'. Ph.D. thesis, TU Dresden, Germany.
- [14] Bürk, E.: 2006, 'Numerische Strömungsberechnung ergänzt durch experimentelle Methoden zur Untersuchung pneumatischer Strömungen'. Ph.D. thesis, TU Dresden, Germany.
- [15] Cremers, J.: 2000, 'Auslegungsmethode zur Vermeidung von Schwingungen bei federbelasteten Sicherheitsventilen mit Zu- und Ableitung'. Ph.D. thesis, TU Hamburg-Harburg, Germany.
- [16] Cremers, J. and L. Friedel: 2003, 'Design of spring loaded safety valves with inlet and discharge pipe against chatter in the case of gas flow'. *Chemical Engineering & Technology* **26**(5), 573–576.
- [17] d'Agostino, L. and M. Salvetti: 2007, *Fluid Dynamics of Cavitation and Cavitating Turbopumps*. SpringerWienNewYork.
- [18] Darby, R. and K. Molavi: 1997, 'Viscosity Correction Factor for Emergency Relief Valves'. *Process Safety Progress* **16**(2), 80–82.
- [19] DIN: 1982, *DIN 1952:1982, Durchflußmessung mit Blenden, Düsen und Venturiröhren in voll durchströmten Rohren mit Kreisquerschnitt (VDI-Durchflußmeßregeln*. Berlin:.
- [20] Domagała, M.: 2008, 'CFD Analysis of pilot operating relief valve'. *Czasopismo Techniczne, wydawnictwo politechniki Krakowskiej* **z. 3-M**.
- [21] Druguet, M. and D. Zeitoun: 2003, 'Influence of numerical and viscous dissipation on shock wave reflections in supersonic steady flows'. *Computers and Fluids* **32**(4), 515–533.
- [22] Föllmer, B.: 1981, 'Strömung im Einlauf von Sicherheitsventilen'. Ph.D. thesis, RWTH Aachen, Germany.
- [23] Föllmer, B. and A. Schnettler: 2003, 'Challenges in designing API safety relief valves'. *Valve World* **10**, 39–43.
- [24] Francis, J. and P. Betts: 1998, 'Backpressure in a high-lift compensated pressure relief valve subject to single phase compressible flow'. *Journal of Loss Prevention in the Process Industries* **11**(1), 55–66.
- [25] Frommann, O.: 2000, 'Effect of Pressure Waves in the Feed Lines upon the Performance of Full Lift Safety Valves'. *Chemical Engineering & Technology* **23**(9), 765–769.

- [26] Hinds, W.: 1999, *Aerosol Technology*. John Wiley & Sons, New York.
- [27] Hoeijmakers, H.: 2005, 'Gasdynamics'. lecture notes 115434, Universiteit Twente, the Netherlands.
- [28] ISO: 2003a, *DIN EN ISO 9300:2003, Durchflussmessung von Gasen mit Venturidüsen bei kritischer Strömung*. Berlin: Beuth Verlag GmbH.
- [29] ISO: 2003b, *EN ISO 5167:2003 Measurement of fluid flow by means of pressure differential devices inserted in circular cross-section conduits running full*. Berlin: Beuth Verlag GmbH.
- [30] ISO: 2004, *EN ISO 4126-1:2004 Safety devices for protection against excessive pressure, Part 1: Safety valves*. Berlin: Beuth Verlag GmbH.
- [31] IUPAC: 2008, 'International Union of Pure and Applied Chemistry: IUPAC Chemical Data Series'. <http://www.iupac.org>.
- [32] Johnson, A., P. Espina, G. Mattingly, J. Wright, and C. Merkle: 1998, 'Numerical Characterization of the Discharge Coefficient in Critical Nozzles'. In: *Proceedings of the 1998 NCSL Workshop Symposium, Albuquerque*.
- [33] Kim, J., H. Kim, T. Setoguchi, and S. Matsuo: 2008, 'Computational study of the gas flow through a critical nozzle'. *Journal of Propulsion and Power* **24**(4), 715–721.
- [34] Knight, D., H. Yan, A. Panaras, and A. Zheltovodov: 2003, 'Advances in CFD prediction of shock wave turbulent boundary layer interactions'. *Progress in Aerospace Sciences* **39**(2-3), 121–184.
- [35] Koenig, H. and L. Friedel: 2005, 'Messung des transienten Massenausstrages und der kurzzeitigen thermofluidodynamischen Vorgänge während der Reaktorentlastung'. *Forschung im Ingenieurwesen* **70**(4), 215–219.
- [36] Kral, L.: 1998, 'Recent experience with different turbulence models applied to the calculation of flow over aircraft components'. *Progress in Aerospace Sciences* **34**(7-8), 481–541.
- [37] Kunz, O., R. Klimeck, W. Wagner, and M. Jaeschke: 2004, 'The GERG-2004 Wide-Range Reference Equation of State for Natural Gases. Fortschr.'. database, Universität Bochum, Germany.
- [38] Li, L., H. Zang, G. Davis, F. Kalb, and S. Hamid: 2005, 'Improving the Closing Characteristics of Subsurface Safety Valve With Combined FEA and CFD Modeling/Numerical Analysis'. In: *SPE Western Regional Meeting*.
- [39] Luft, G., J. Broedermann, and T. Scheele: 2007, 'Pressure Relief of High Pressure Devices'. *Chemical Engineering & Technology* **30**(6), 695–701.
- [40] MacLeod, G.: 1985, 'Safety valve dynamic instability: An analysis of chatter'. *Journal of Pressure Vessel Technology* **107**, 172–177.

- [41] Mahkamov, K.: 2006, 'An Axisymmetric Computational Fluid Dynamics Approach to the Analysis of the Working Process of a Solar Stirling Engine'. *Journal of Solar Energy Engineering* **128**, 45–53.
- [42] Menter, F.: 1994, 'Two-equation eddy-viscosity turbulence models for engineering applications'. *AIAA journal* **32**(8), 1598–1605.
- [43] Müller, J., R. Mümmler, and W. Staudacher: 2001, 'Comparison of some measurement techniques for shock-induced boundary layer separation'. *Aerospace Science and Technology* **5**(6), 383–395.
- [44] Moisidis, N. and M. Ratiu: 1995, 'Enhancement of Pressurizer Safety Valve Operability by Seating Design Improvement'. *Journal of Pressure Vessel Technology* **117**, 279–282.
- [45] Moncalvo, D., L. Friedel, B. Jörgensen, and T. Höhne: 2009, 'Sizing of Safety Valves Using ANSYS CFX-Flo®'. *Chemical Engineering & Technology* **32**(2), 247–251.
- [46] Moran, M. and H. Shapiro: 2006, *Fundamentals of Engineering Thermodynamics, 5th edition*. West Sussex: John Wiley & Sons Ltd.
- [47] Muschelknautz, S. and A. Wellenhofer: 2003, 'Flow reaction forces upon blow-down of safety valves'. *Chemical Engineering & Technology* **26**(7), 797–803.
- [48] Netter, U.: 2005, 'Messung und Berechnung des Massenstroms realer Gase durch eine Düse bei Vordrücken bis 3500 bar'.
- [49] NIST: 2009, 'NIST Chemistry WebBook, NIST Standard Reference Database Number 69'. <http://webbook.nist.gov/chemistry/>.
- [50] Nitsche, W.: 1994, *Strömungsmesstechnik*. Berlin-Heidelberg-New York: Springer-Verlag.
- [51] Reich, A., V. Parthasarathy, and A. DiMeo: 2001, 'Coupled Fluid-Structure Interaction Simulation of the Opening of the Target Rock Vacuum Relief Valve'. *ASME Publications PVP* **424**, 23–28.
- [52] Reid, R. and T. Sherwood: 1966, *The properties of gases and liquids, 2nd edition*. New York: McGraw-Hill.
- [53] Rhie, C. and W. Chow: 1983, 'Numerical study of the turbulent flow past an airfoil with trailing edge separation'. *AIAA* **21**, 1525–1532.
- [54] Rigas, F. and S. Sklavounos: 2005, 'Experimentally validated 3-D simulation of shock waves generated by dense explosives in confined complex geometries'. *Journal of hazardous materials* **121**(1-3), 23–30.
- [55] Rist, D.: 1996, *Springer-Verlag*. Berlin Heidelberg:.

- [56] Roberts, R. and J. Cui: 2006, 'Numerical analysis of a pulsation damper fuel injection rails'. *Int. J. Vehicle Systems Modelling and Testing* **1**(4), 312–328.
- [57] Sallet, D., W. Nastoll, R. Knight, M. Palmer, and A. Singh: 1981, 'Experimental investigation of the internal pressure and flow fields in a safety valve'. *Am. Soc. Mech. Eng.* **81-WA/NE-19**, 1–8.
- [58] Savitzky, A. and M. Golay: 1964, 'Smoothing and differentiation of data by simplified least squares procedures'. *Analytical chemistry* **36**, 1627–1639.
- [59] Schmidt, J., W. Peschel, and A. Beune: 2009, 'Experimental and theoretical studies on high pressure safety valves: sizing and design supported by numerical calculations (CFD)'. *Chemical Engineering & Technology* **32**(2), 1–12.
- [60] Settles, G. and L. Dodson: 1991, 'Hypersonic Shock/Boundary-Layer Interaction Database'. NASA Contractor Report 177577, NASA.
- [61] Shapiro, A.: 1954, *The Dynamics and Thermodynamics of Compressible Fluid Flow, Vol. II*. New York: The Ronald Press Co.
- [62] Singh, A.: 1982, 'An analytical study of the dynamics and stability of a spring loaded safety valve'. *Nuclear Engineering and Design* **72**, 179–204.
- [63] Singhal, A., M. Athavale, H. Li, and Y. Jiang: 2002, 'Mathematical basis and validation of the full cavitation model'. *Journal of Fluids Engineering* **124**, 617–624.
- [64] Soave, G.: 1972, 'Equilibrium constants from a modified Redlich-Kwong equation of state'. *Chemical Engineering Science* **27**(6), 1197–1203.
- [65] Sod, G.: 1978, 'A survey of several finite difference methods for systems of nonlinear hyperbolic conservation laws'. *J. Comput. Phys* **27**(1), 1–31.
- [66] Srikanth, C. and C. Bashker: 2009, 'Flow analysis in valve using moving grids through CFD techniques'. *Advances in Engineering Software* **40**, 193–201.
- [67] Tsuboi, H., M. Tanaka, K. Ikeda, and K. Nishimura: 2001, 'Computation results of the TEAM workshop Problem 7 by finite element methods using tetrahedral and hexahedral elements'. *Journal of Materials Processing Tech.* **108**(2), 237–240.
- [68] TÜV: 1988, 'Bericht über die Prüfung von Sicherheitsventilen'. report, TÜV Rheinland Aachen.
- [69] Wilcox, D.: 1993, 'A two-equation turbulence model for wall-bounded and free-shear flows'. In: *1993 AIAA 24th Fluid Dynamics Conference*.
- [70] Wyslouzil, B. E., C. H. Heath, J. L. Cheung, and G. Wilemski: 2000, 'Binary condensation in a supersonic nozzle'. *J. Chem. Phys.* **113**(17), 7317–7329.

- [71] Zahariev, T.: 2001, 'Berechnung der Durchströmung und der Kennwerte von Sicherheitsventilen'. Ph.D. thesis, Otto-von Guericke-Universität Magdeburg, Germany.

Dankwoord

Onverwachts ben ik de uitdaging aangegaan om onderzoek te doen in samenwerking met 's werelds grootste chemieonderneming BASF SE en 3 jaar te werken op Europees grootste chemische fabrieksterrein Ludwigshafen. Daarbij mijn dank aan prof. Bert Brouwers voor zijn vertrouwen en rol als 'doktervader' door de jaren heen. Gerne möchte ich mich bei Herrn Prof. Jürgen Schmidt für die Gelegenheit bedanken, dieses Projekt bei der BASF durchführen zu dürfen. Dabei hat er mir viel Selbständigkeit und Freiheit überlassen, wodurch ich mich selbst entwickeln und viel lernen konnte.

Mijn directe begeleider dr. Hans Kuerten ben ik bijzonder veel dank verschuldigd ook voor zijn geduld, inlevingsvermogen en het altijd voor me klaar staan. De samenwerking TU/e - BASF is voor mij een ideale mix geweest om met de modernste rekenmethoden een kwaliteitsproduct met een historie een 300 jaar te optimaliseren.

Viel Unterstützung habe ich von Seiten der BASF aus der Gruppe Sicherheits- und Strömungstechnik erhalten. Besonderen Dank gilt hier dem Gruppenleiter Herrn Dr. Klaus Herrmann, aber auch den vielen Kollegen für die anregenden Diskussionen. Ebenfalls besonderen Dank möchte ich Herrn Dr. Jens Denecke für die Durchführung der Simulationen aussprechen.

Des Weiteren danke ich Herrn Dr. Wolfgang Peschel und seinen Kollegen der Abteilung Hochdrucktechnik für das entgegengebrachte Interesse, die Zeit und die Unterstützung für Aufbau und Betrieb des Versuchsstandes. Dabei haben die Herren Hahn, Rodach und Kauffeld ausgezeichnete Arbeit geleistet, das 'Holländische Wasserspiel' aufzubauen und zu betreiben. Erwähnen möchte ich auch die Mitarbeiter der beteiligten Konstruktionsbüros, die am Entwurf vieler Sonderteile mitwirkten.

Discussions met prof. Harry Hoeijmakers and prof. Rini van Dongen heb ik zeer gewaardeerd. Zonder de hulp van twee stagiaires/afstudeerders was ik niet zover gekomen. Eerst Edwin Gerritsen voor zijn oriënterende metingen en berekeningen. Bijzonder veel dank aan Martijn van Heumen als fijne discussiepartner en programmeerwerk om de automatisering van de meetdataverwerking en de dynamische modellering mogelijk te maken. Verder dank aan dr. Bert Vreman voor zijn simulaties.

Ook al was ik in de tussentijd nauwelijks in Eindhoven, in het eerste en laatste half jaar hebben mijn gewaardeerde collega's op vloer 2 altijd een luisterend oor voor me voorzien van koffie. Ook de studiereizen naar Zwitserland op initiatief van Bert waren voor mij een fantastische gelegenheid elkaar beter te leren kennen.

Tenslotte bedank ik mijn ouders voor de onvoorwaardelijke steun en liefde, zodat ik op een hele mooie tijd terug kan kijken!

Curriculum vitae

Arend Beune was born in Helmond, the Netherlands, on the 23rd of October 1978. From 1991 to 1997 he attended pre-university education (VWO) at Carolus Borromeus College in Helmond, the Netherlands. In 1997 he started to study Mechanical Engineering at Eindhoven University of Technology (the Netherlands). In 1999-2000 he was one year a board member of the student association of the faculty of Mechanical Engineering 'Simon Stevin'.

During his four-month internship at the University of Strathclyde in Glasgow (United Kingdom) in 2004 he was involved in experimental research on the characteristics of bubble formation when emerging from an orifice depending on wettability and Reynolds number. Hereafter in 2004-2005 he performed the practical part of his Master's thesis at the research institute for Recourse Efficient and Sustainable Systems at Graz University of Technology, Austria. During his stay of eight months he analyzed the devices of a pot furnace biomass combustion setup and implemented improvements, which increased its reliability and accuracy. In February 2005 he received his MSc degree 'with great appreciation' in Mechanical Engineering at Eindhoven University of Technology (TU/e).

Thereafter, he started to work on his PhD project in the Process Technology group of TU/e in cooperation with and funded by the Safety Engineering & Fluid Dynamics and High-pressure Technology departments of BASF SE in Ludwigshafen (Germany). The topic of his research is to develop a numerical method to predict the discharge capacity and opening characteristic of high-pressure safety valves up to 3600 bar. This is a basis for a new approach to reduce time-consuming and cost-intensive experiments and improve their operating reliability. For the experimental validation he has worked at BASF for three years. There he has built a unique industrial mini-plant to carry out the high-pressure valve tests at double set pressures compared to existing test facilities.